

NORTHWESTERN UNIVERSITY

Electrochemical and Phase Stability Studies of
Cathode Materials for Solid Oxide Fuel Cells

A DISSERTATION

SUBMITTED TO THE GRADUATE SCHOOL
IN PARTIAL FULFILLMENT OF THE REQUIREMENTS

for the degree

DOCTOR OF PHILOSOPHY

Field of Materials Science and Engineering

By

Patrick K. Duffy

EVANSTON, ILLINOIS

December 2016

© Copyright by Patrick K. Duffy 2016

All Rights Reserved

Abstract

Electrochemical and Phase Stability Studies of
Cathode Materials for Solid Oxide Fuel Cells

Patrick K. Duffy

Growing energy and climate concerns in the United States and across the world demand improvements in energy efficiency, conservation, and renewability. Solid oxide fuel cells (SOFCs) are highly efficient devices that electrochemically convert the chemical energy of a fuel to electricity. These devices can operate on natural gas as a fuel, enabling the use of existing infrastructure with significantly higher efficiency compared to conventional natural gas power plants. However, expensive system components and durability issues prevent SOFCs from being cost-competitive with current power plants.

This work focused on the search for new SOFC materials that provide increased performance at reduced operating temperatures. Both electrochemical performance and thermodynamic stability between various layers are important factors for creating SOFCs with good long-term performance, and both were investigated in this work, making extensive use of AC impedance spectroscopy and X-ray diffraction. A novel method used to rapidly character-

ize the electrochemical performance of electrode materials was developed. A hemispherical electrolyte probe pressed into the flat surface of a dense electrode pellet created a circular interface. Impedance spectroscopy measured the polarization resistance associated with the electrode reaction at the interface, along with the resistance of the electrolyte probe, from which the size of the contact was determined. The polarization resistance was normalized by the triple phase boundary (TPB) length to calculate the TPB linear-specific resistance of electronic conductor electrodes. For mixed ionic-electronic conductor (MIEC) electrodes, the polarization resistance was normalized by the contact area to estimate the area-specific surface resistance. Both normalized resistances were found to underestimate literature values by a consistent factor of about 3. The method is shown to have good potential for the rapid screening and ranking of potential SOFC electrode materials.

Details of thermodynamic equilibrium were also refined in the $\text{LaO}_{1.5}\text{-GaO}_{1.5}\text{-NiO}$ quaternary phase diagram. Solubility limits of the $\text{La}_{n+1}\text{Ni}_n\text{O}_{3n+1}$ Ruddlesden-Popper series of phases and LaGaO_3 were determined using conventional phase analysis and the disappearing phase method. For the first time, $\text{La}_3\text{Ni}_2\text{O}_7$ was found to be stabilized over a small compositional range by the substitution of gallium for nickel. The compositional details of phase relationships involving LaGaO_3 were also determined using the disappearing phase method by locating the vertex location of triphasic regions. Equilibrium between LaGaO_3 and $\text{La}_4\text{Ni}_3\text{O}_{10}$ was confirmed, albeit at substantial levels of nickel in LaGaO_3 and gallium in $\text{La}_4\text{Ni}_3\text{O}_{10}$, both of which are detrimental to device performance. No equilibrium was observed between LaGaO_3 and the other $\text{La}_{n+1}\text{Ni}_n\text{O}_{3n+1}$ phases. Equilibrium between LaGaO_3 and NiO was also confirmed. Additionally, saturating NiO with gallium was found to minimize the amount of nickel in LaGaO_3 , with an equilibrium concentration of only 7% of the gallium replaced by nickel in the latter.

Acknowledgements

I would like to extend my deepest gratitude to my advisors Professor Thomas Mason and Professor Scott Barnett. Both of you have molded me into the scientist, engineer, and person I am today. Professor Mason: Thank you for continuously challenging me for the past five years. Your mentorship has taught me to question my assumptions, and has transformed me into a better scientist, a more effective communicator, and a more compassionate mentor myself. Professor Barnett: Thank you for fully welcoming me into your research group for the second half of my graduate studies. Your trust in me has given me the confidence to take ownership of my work and to become a more independent researcher.

I would also like to thank the other members of my committee, Professor Peter Voorhees, Professor Sossina Haile, and Dr. Brian Ingram for their suggestions and advice throughout this process. Over the past five years, I have had the pleasure of working with several outstanding undergraduate researchers; Rachel Beal and Carys Layton who made and characterized many samples for the phase diagram work, and Juveria Masood and Letty Dornfeld who helped pioneer the development of LNO-LSGM cathodes from citric acid-EDTA powders. Also, much of my work would not have been possible without the aid of several lab staff members including Dr. Carla Shute and Jerry Carsello.

I am grateful for the support and comradery of the members of the Mason and Barnett research groups, both past and present. Thank you Mitch, Diana, Danielle, and Qimin for showing me the research ropes and getting me started on my journey. Thank you Ted and Nicola for teaching me everything I needed to know about impedance spectroscopy and ion conductors, and thank you Gareth, Ann, and Kyle for teaching me everything I needed to know about fuel cells. Justin, thank you for teaching me all about the Barnett lab, and for saving me when things went awry. Adler, Arpun, Stephanie, Sam, and Karen, your friendship has kept me sane over the years, from lunches to walks along the lakefront to late nights at Nevin's or Bat 17. I'll love you guys forever. Alex and Kyle, how lucky I was to find such amazing friends as roommates when moving to a new and unfamiliar city. You've always been there to share a beer and a laugh when I needed it.

To all of my other friends and family, I've relied heavily on your love and support throughout the past five years. Thank you for giving me something to talk about other than science (or at least science that isn't my research). Ryan and Michael, brothers and lifelong friends, you are always a source of comfort and support. To my dad, thank you for imparting your love of science and learning, and for giving me confidence when it's hard to find myself. To my mom, always my biggest cheerleader, I wish you could be here to celebrate this moment. I'm sure you'd be proud and bragging to everyone you know. Finally, thank you to Allie for joining me on this crazy, exciting, stressful, intimidating, and rewarding ride. Your constant faith in me has given me the strength I need, and I could never have done this without your support and companionship.

List of Abbreviations

BSCF (Ba,Sr)(CoFe)O_{3-δ}

CALPHAD Caluclation of Phase Diagrams

CGO Cerium Gadolinium Oxide (see GDC)

CHP Combined Heat and Power

CPE Constant Phase Element

EDTA Ethylenediaminetetraacetic Acid

FCC Face Centered Cubic

FRA Frequency Response Analyzer

GDC Gadolinia-Doped Ceria

HEP Hemispherical Electrolyte Probe

IEDP Ion Exchange Depth Profiling

LCM (La,Ca)MnO₃

LGO Orthorhombic LaGaO₃

LGO Rhombohedral LaGaO₃

LNO Lanthanum Nickel Oxide (La₂NiO₄ unless otherwise noted)

LSC La_{0.6}Sr_{0.4}CoO_{3-δ}

LSCF $\text{La}_{0.6}\text{Sr}_{0.4}\text{Co}_{0.8}\text{Fe}_{0.2}\text{O}_{3-\delta}$

LSF $\text{La}_{0.6}\text{Sr}_{0.4}\text{FeO}_{3-\delta}$

LSFC $\text{La}_{0.6}\text{Sr}_{0.4}\text{Fe}_{0.8}\text{Co}_{0.2}\text{O}_{3-\delta}$

LSGM $\text{La}_{0.9}\text{Sr}_{0.1}\text{Ga}_{0.8}\text{Mg}_{0.2}\text{O}_{3-\delta}$

LSM $\text{La}_{0.8}\text{Sr}_{0.2}\text{MnO}_3$

MIEC Mixed Ionic-Electronic Conductor

PVB Polyvinyl Butyral

ReSOC Reversible Solid Oxide Cell

SDC Samarium-Doped Ceria

SIMS Secondary Ion Mass Spectrometry

SOEC Solid Oxide Electrolysis Cell

SOFC Solid Oxide Fuel Cell

SSC $\text{Sm}_{0.5}\text{Sr}_{0.5}\text{CoO}_{3-\delta}$

TEM Transmission Electron Microscopy

TPB Triple Phase Boundary

US-EIA United States Energy Information Administration

WPF Whole Pattern Fitting

XRD X-ray Diffraction

YSZ Yttria-Stabilized Zirconia

Contents

| | |
|--|-----------|
| Abstract | 3 |
| Acknowledgements | 5 |
| List of Abbreviations | 7 |
| List of Tables | 13 |
| List of Figures | 16 |
| 1 Introduction | 17 |
| 1.1 Outline of Objectives and Organization | 18 |
| 2 Background | 20 |
| 2.1 Energy Outlook | 20 |
| 2.1.1 Energy and Carbon in the United States | 21 |
| 2.2 Solid Oxide Fuel Cells | 25 |
| 2.2.1 Operation | 25 |

| | |
|--|-----------|
| | 10 |
| 2.2.2 Advantages and Challenges | 27 |
| 2.3 SOFC Materials and Microstructures | 28 |
| 2.3.1 Electrolytes | 28 |
| 2.3.2 Electrodes | 31 |
| 2.4 Patterned Electrode and Combinatorial Studies | 37 |
| 2.4.1 Triple Phase Boundary Linear-Specific Resistance | 38 |
| 2.4.2 Area-Specific Surface Resistance | 38 |
| 2.4.3 Combinatorial Measurements | 38 |
| 2.5 LaO _{1.5} -GaO _{1.5} -NiO Quasi-Ternary System | 39 |
| 2.5.1 Bounding Quasi-Binary Systems | 39 |
| 2.5.2 Quasi-Ternary System | 43 |
| 3 Sample Preparation and Characterization | 45 |
| 3.1 Solid State Synthesis | 45 |
| 3.2 X-ray Diffraction and Whole Pattern Fitting | 47 |
| 3.3 Phase Stability Investigations | 48 |
| 3.3.1 Conventional Phase Analysis | 48 |
| 3.3.2 Vegard's Law | 49 |
| 3.3.3 Disappearing Phase Method | 49 |
| 3.4 Electrical Characterization | 51 |
| 3.4.1 Four-Point Probe Electrical Conductivity | 51 |
| 3.4.2 Electrochemical Impedance Spectroscopy | 54 |
| 4 Hemispherical Electrolyte Probe for Screening Cathode Materials | 58 |
| 4.1 Overview of Process | 58 |
| 4.2 Surface Roughness Using Optical Profilometry | 64 |

| | |
|---|------------|
| | 11 |
| 4.3 Assumptions and Validation | 64 |
| 4.3.1 Dependence of Polarization Resistance of Contact Size | 67 |
| 4.3.2 Effect of DC Bias | 67 |
| 4.3.3 Spreading Resistance of a Large Hemisphere | 71 |
| 4.3.4 Effect of Polishing | 73 |
| 4.3.5 Mechanical Confirmation of Contact Size by Probe Resistance | 74 |
| 4.4 Finalized Measurements | 76 |
| 4.4.1 Triple Phase Boundary Linear-Specific Resistance | 77 |
| 4.4.2 Mixed Conductor Area-Specific Resistance | 77 |
| 4.5 Conclusions | 82 |
| 5 Phase Compatibility in the LaO_{1.5}-GaO_{1.5}-NiO System | 84 |
| 5.1 Solubility Limit Determination | 85 |
| 5.2 Compatibility Involving LaGaO ₃ | 88 |
| 5.2.1 Electrical Conductivity of La ₄ (Ni,Ga) ₃ O ₁₀ | 93 |
| 5.3 Approximate Representation of the Full Phase Diagram | 94 |
| 5.4 Conclusions and Implications for SOFCs | 96 |
| 6 Summary and Recommendations for Future Work | 99 |
| 6.1 Hemispherical Electrolyte Probe Method | 99 |
| 6.2 LaO _{1.5} -GaO _{1.5} -NiO Quasi-Ternary System | 100 |
| 6.3 Future Directions | 102 |
| 6.3.1 HEP Screening of Cathode and Anode Materials | 102 |
| 6.3.2 LSGM-Ni Phase Stability | 103 |
| 6.3.3 Optimization and Stability of LNO-LSGM Cathodes | 104 |
| References | 114 |

| | |
|---|------------|
| Appendix A Fabrication and Performance of Mixed La_2NiO_4-LSGM Cathodes | 115 |
| A.1 Synthesis and Purity of Cathode Powders | 115 |
| A.2 Synthesis of LSGM Electrolytes | 117 |
| A.3 Device Fabrication | 117 |
| A.4 Initial Electrochemical Performance | 120 |
| Appendix B $\text{LaO}_{1.5}$-$\text{GaO}_{1.5}$-NiO Phase Diagram Samples | 123 |

List of Tables

| | | |
|-----|---|-----|
| 2.1 | Ionic Radii | 40 |
| 3.1 | Resistivity Correction Factors | 53 |
| 4.1 | HEP Electrode Density and Activation Energy | 60 |
| 4.2 | Elastic Constants of YSZ and LSFC | 76 |
| 5.1 | Solubility Limits | 86 |
| 5.2 | Triphasic Region Vertex Compositions | 94 |
| A.1 | Symmetric Cell Activation Energies | 121 |

List of Figures

| | | |
|------|---|----|
| 2.1 | World Net Electricity Projection | 22 |
| 2.2 | World Renewable Energy Projection | 22 |
| 2.3 | U.S. Energy Consumption | 23 |
| 2.4 | U.S. Carbon Emissions | 24 |
| 2.5 | SOFC Operation | 26 |
| 2.6 | Perovskite Crystal Structure | 30 |
| 2.7 | Fluorite Crystal Structure | 30 |
| 2.8 | Conductivity of SOFC Electrolyte Materials | 31 |
| 2.9 | Area-Specific Resistance of SOFC Cathode Materials | 34 |
| 2.10 | Ruddlesden-Popper Series Crystal Structures | 35 |
| 2.11 | Electrode Microstructures | 36 |
| 2.12 | GaO _{1.5} -LaO _{1.5} Quasi-Binary Phase Diagram | 41 |
| 2.13 | Ga ₂ O ₃ -NiO Quasi-Binary Phase Diagram | 41 |
| 2.14 | LaO _{1.5} -NiO Quasi-Binary Phase Diagram | 42 |
| 2.15 | CALPHAD LaO _{1.5} -GaO _{1.5} -NiO Quasi-Ternary Phase Diagram | 44 |

| | |
|---|----|
| | 15 |
| 3.1 Thermogravimetric Analysis of La_2O_3 Powder | 46 |
| 3.2 La_2O_3 Decomposition Steps | 46 |
| 3.3 Identifying Vertices of Triphasic Regions | 51 |
| 3.4 Four-Point Probe Geometry | 53 |
| 3.5 Schematic Bode Plot | 56 |
| 3.6 Schematic Nyquist Plot | 56 |
| 4.1 Hemispherical Electrolyte Probe Geometry | 60 |
| 4.2 Sample Holder | 61 |
| 4.3 Idealized and Realistic Contact Profiles | 61 |
| 4.4 HEP Impedance Spectra | 65 |
| 4.5 YSZ Probe Resistivity | 65 |
| 4.6 YSZ Probe Surface Topography | 66 |
| 4.7 LSM Polarization Resistance vs. Contact Radius | 68 |
| 4.8 LCM Polarization Resistance vs. Contact Radius | 68 |
| 4.9 LSM Polarization Resistance vs. DC Bias | 70 |
| 4.10 LSM Polarization Resistance and DC Bias Over Time | 70 |
| 4.11 Geometry for Measuring Spreading Resistance of Hemisphere and Cylinder . . | 72 |
| 4.12 Spreading Resistance of Hemisphere and Cylinder | 72 |
| 4.13 Effect of Polishing Pellet Surface on ρ_{TPB} | 74 |
| 4.14 Mechanical Confirmation of HEP Contact Size | 76 |
| 4.15 HEP Polarization Resistances | 78 |
| 4.16 HEP Probe Resistances | 78 |
| 4.17 Linear-Specific TPB Resistance of LSM and LCM | 79 |
| 4.18 Area-Specific Resistance of LSFC and SSC | 79 |
| 4.19 Reproducibility of HEP Measurements on LSFC | 81 |

| | | |
|------|--|-----|
| 5.1 | Ternary Diagram Sample Compositions | 87 |
| 5.2 | Disappearing Phase Method: La_2NiO_4 | 89 |
| 5.3 | Disappearing Phase Method: $\text{La}_3\text{Ni}_2\text{O}_7$ | 89 |
| 5.4 | Disappearing Phase Method: $\text{La}_4\text{Ni}_3\text{O}_{10}$ | 90 |
| 5.5 | Disappearing Phase Method: LaGaO_3 | 90 |
| 5.6 | $\text{LaO}_{1.5}$ - $\text{GaO}_{1.5}$ - NiO Solubility Limits | 91 |
| 5.7 | Compatibility with LaGaO_3 | 92 |
| 5.8 | Disappearing Phase Method: 40 mol% $\text{LaO}_{1.5}$ | 93 |
| 5.9 | Four-Point Conductivity of $\text{La}_4(\text{Ni,Ga})_3\text{O}_{10}$ | 95 |
| 5.10 | Updated $\text{LaO}_{1.5}$ - $\text{GaO}_{1.5}$ - NiO Phase Diagram | 96 |
| A.1 | Purity of LSGM Citric Acid – EDTA Powders | 118 |
| A.2 | XRD Spectra of LSGM Citric Acid – EDTA Powders | 118 |
| A.3 | Purity of LSGM Citric Acid – EDTA Powders | 119 |
| A.4 | Nyquist Plot of LNO-LSGM Symmetric Device | 121 |
| A.5 | Ohmic and Polarization Resistances of Symmetric Device | 122 |
| A.6 | High, Mid, and Low Frequency Resistances of Symmetric Device | 122 |

CHAPTER 1

Introduction

Solid Oxide Fuel Cells (SOFCs) are solid state devices that directly convert chemical energy stored in a fuel into electrical energy through an electrochemical process. SOFCs exhibit high efficiency, low emissions, fuel flexibility, and decent impurity tolerance, making them of interest for medium to large scale energy production applications. Their high efficiency provides the potential to greatly reduce carbon emissions from electricity generation, and their inherently modular design makes them excellent candidates for highly dispersed power generation. However, SOFCs are not yet cost-competitive with traditional electricity generation technologies, largely owing to durability and lifetime issues.

SOFCs operate at high temperatures, traditionally in the range of 800-1000 °C. The high temperature is necessary to obtain sufficient ion transport and reaction rates in the device. However, the high operating temperature accelerates degradation mechanisms such as interfacial reactions and coarsening of electrode particles. Lowering the operating temperature could significantly extend device lifetimes and lower costs, but new materials are required to achieve acceptable performance at lower temperatures. New oxide-ion conductors including strontium- and magnesium-doped lanthanum gallate (LSGM) and gadolinium-doped ceria (GDC) have been proposed as replacements for standard yttria-stabilized zirconia elec-

trolytes. New electrode materials with good intermittent temperature performance showing good stability with these improved electrolyte materials could significantly improve device lifetime and decrease cost.

The goal in this thesis work is to investigate the performance of various SOFC cathode materials as well as their stability with LSGM. Understanding both electrochemical performance and phase stability are necessary to design a device with high efficiency that remains stable over time.

1.1. Outline of Objectives and Organization

The objectives of this work are as follows:

1. Develop a method allowing for the rapid screening of potential cathode materials
2. Investigate the details of the thermodynamic equilibrium between LSGM and potential electrode materials
3. Determine proper synthesis conditions for mixed cathodes using LSGM electrolytes and examine initial cathode performance in the intermediate temperature range.

This thesis is organized into several chapters, each focusing on one aspect of the work:

Chapter 2 provides background context for the work presented in the rest of this thesis. This chapter begins with an outlook on the future energy landscape and environmental impacts in the United States and the world, before discussing the operation of SOFCs along with their advantages and challenges. The properties of various electrode and electrolyte materials and common electrode structures are discussed. The chapter then focuses on previous work from the literature more closely related to the work presented in this thesis, including combinatorial studies of electrode materials and phase stability in the $\text{LaO}_{1.5}$ - $\text{GaO}_{1.5}$ - NiO quasi-ternary system.

Chapter 3 describes all of the methods and techniques used to prepare and characterize samples used in this work. For the sample preparation methods, the overall process is explained, though specific parameters such as firing temperatures that varied from sample to sample are specified in later chapters. The characterization methods include X-ray diffraction, various methods for determining phase stability, and electrochemical impedance spectroscopy, listing the instruments and settings used in each case.

Chapter 4 presents the development of the hemispherical electrolyte probe (HEP) method used to screen the performance of cathode materials. The chapter begins with an overview of the process, then looks at efforts to validate the various assumptions and approximations associated with the analysis. The chapter concludes by comparing the results of the HEP measurements to literature values obtained using more traditional methods, then discussing the comparison and implications for the future application of the method.

Chapter 5 presents the determination of the details of phase compatibility in the $\text{LaO}_{1.5}\text{-GaO}_{1.5}\text{-NiO}$ quasi-ternary system. The system contains several materials with potential SOFC applications, and the details of phase stability between them is indicative of behavior during high-temperature processing or long-term operation.

Chapter 6 summarizes the conclusions from the various studies of this thesis. This chapter also discusses future work that could build upon the conclusions in each study, including phase stability, using HEP methods to screen electrode materials, and investigating the initial and long-term performance of cathodes created using the results presented in Appendix A.

Appendix A presents the wet synthesis of powders used to create mixed $\text{La}_2\text{NiO}_4\text{-LSGM}$ cathodes. The phase purity of powders fired at various temperatures is presented, along with the investigation of the firing temperature required to create a mechanically stable cathode. The appendix concludes by presenting initial measurements of electrochemical performance device microstructure.

CHAPTER 2

Background

2.1. Energy Outlook

Global energy production and consumption is a growing issue. [1] As population rises, and more countries continue to industrialize, energy demand rises, leading to more rapid consumption of fossil fuels and increased carbon production, contributing to global climate change. The U.S. Energy Information Administration (US-EIA) predicts that world total energy consumption will grow by 48% by 2040, equivalent to a 1.4% increase each year, and world net electricity generation will increase by 69%. However, the mix of energy sources for electricity generation is also expected to change, as shown in Fig. 2.1. While coal provided about 40% of the world's electricity in 2012, it is predicted to plateau while contributions from natural gas and renewables grow much faster. By 2040, coal, natural gas, and renewable sources will contribute roughly equal amounts to the world's electricity generation.

Renewable sources are expected to be the fastest growing source of electricity, increasing by about 2.9% per year and supplying 29% of the world's electricity in 2040, compared to 22% in 2012. The majority of this growth is expected to come from non-hydropower sources such as wind and solar contriwer renewables, particularly wind and solar, as shown in Fig.

2.2, though hydropower still accounts for the majority of renewable electricity generation. As intermittent power more to the electrical grid, large scale energy storage may be necessary in order to efficiently match electricity supply and demand. Despite substantial increases in renewable energy, however, fossil fuels are still expected to account for 57% of the world's electricity and 78% of the world's total energy consumption in 2040. Utilizing those fuels, including natural gas, more efficiently could significantly reduce the amount of carbon released into the atmosphere from energy use.

2.1.1 Energy and Carbon in the United States

Electricity generation remains the largest area of energy use in the United States, accounting for 38% of all energy use in 2015, as shown in Fig. 2.3. Electricity generation also remains highly inefficient, with 67% of the energy input (over 25% of the total U.S. energy consumption) wasted. Although renewables including wind and solar have grown, and less carbon-intensive natural gas has begun to displace coal usage, electricity generation is also the largest area of carbon emissions in the United States, accounting for about 38% of all carbon emissions, as shown in Fig. 2.4. While coal accounts for only 38% of the energy input for electricity generation, it is responsible for 76% of the carbon emissions from electricity generation. In fact, coal used for electricity generation is the second largest source for carbon emissions in the U.S. (29% of total emissions) behind petroleum used for transportation (33% of total emissions). While renewable energy technologies show promise for long term solutions to issues of carbon emissions, they will not likely dominate the energy scene in the U.S. or around the world in the near future. In the meantime, there are major opportunities to increase the amount of useable energy produced while simultaneously reducing carbon emissions by more efficiently using less carbon intensive fuels such as natural gas.

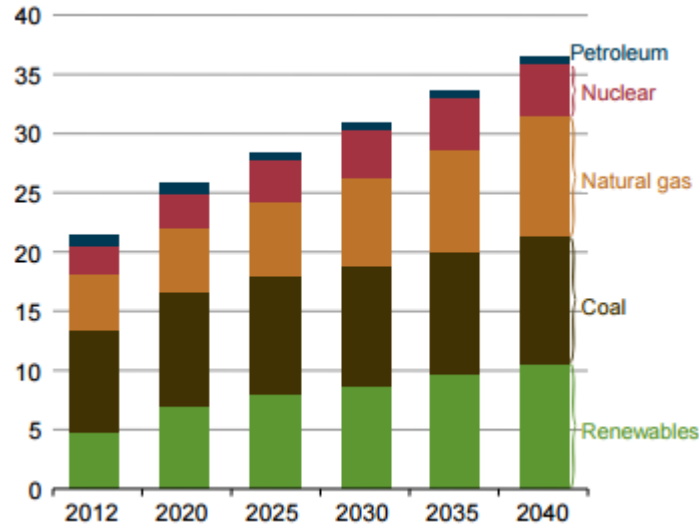


Figure 2.1: World net electricity generation by energy source projections by the U.S. Energy Information Administration. [1] Values are in trillions of kWh.

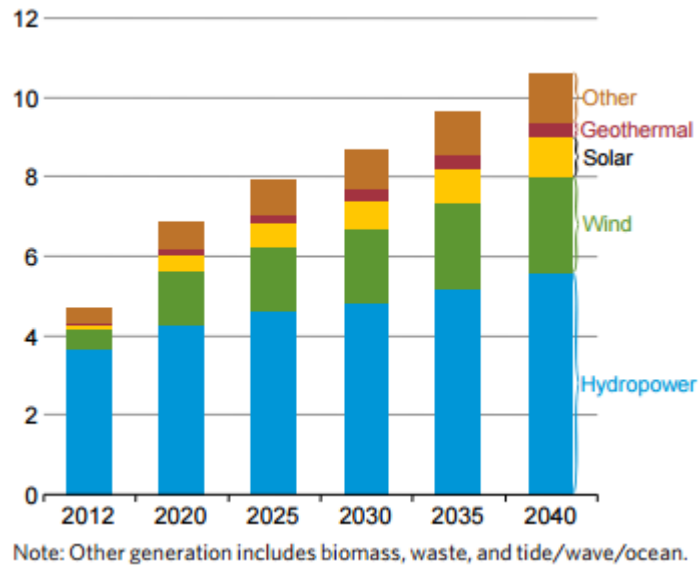
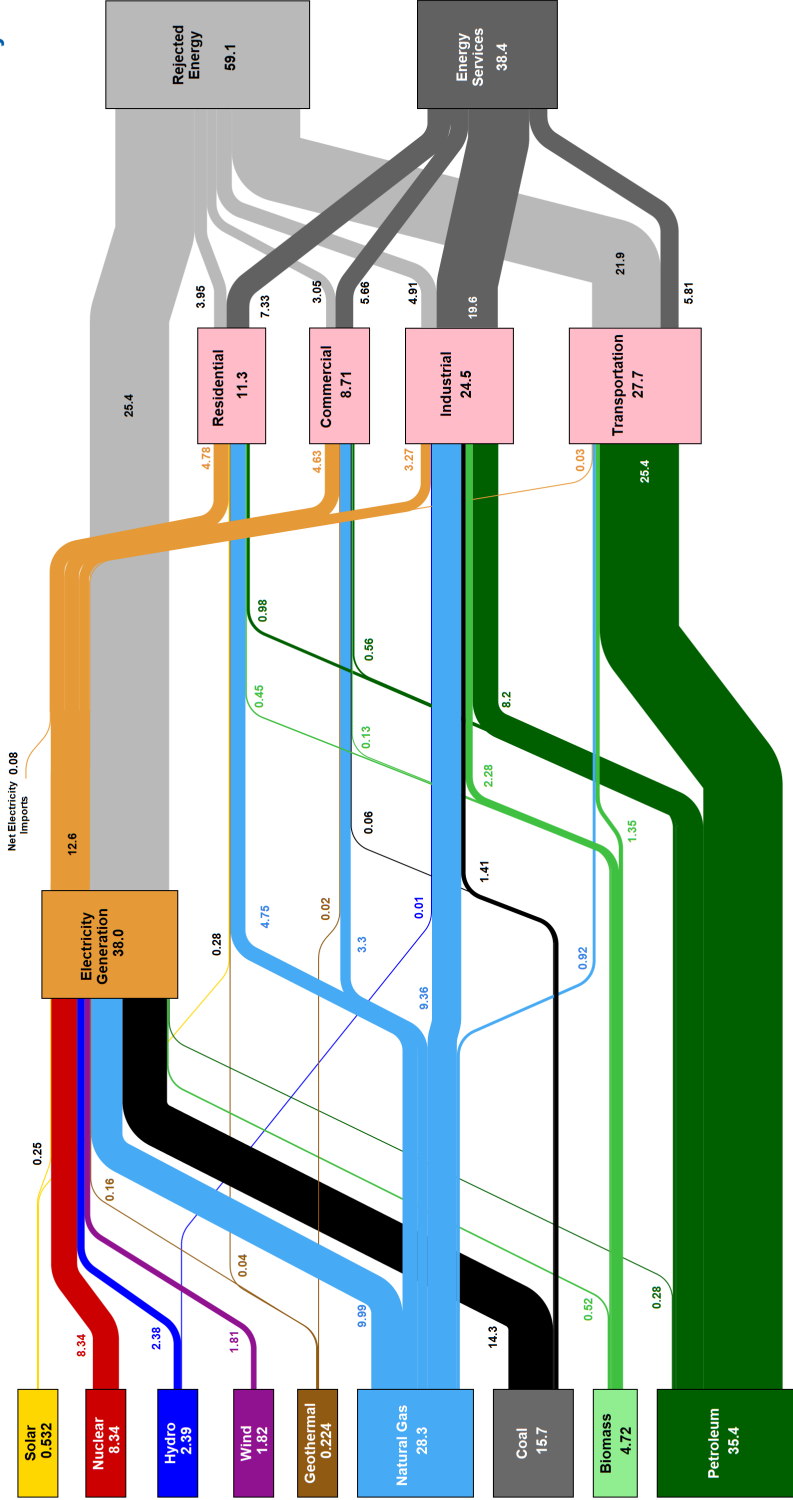


Figure 2.2: World net energy generation from renewable sources projected by the U.S. Energy Information Administration. [1] Values are in trillions of kWh.

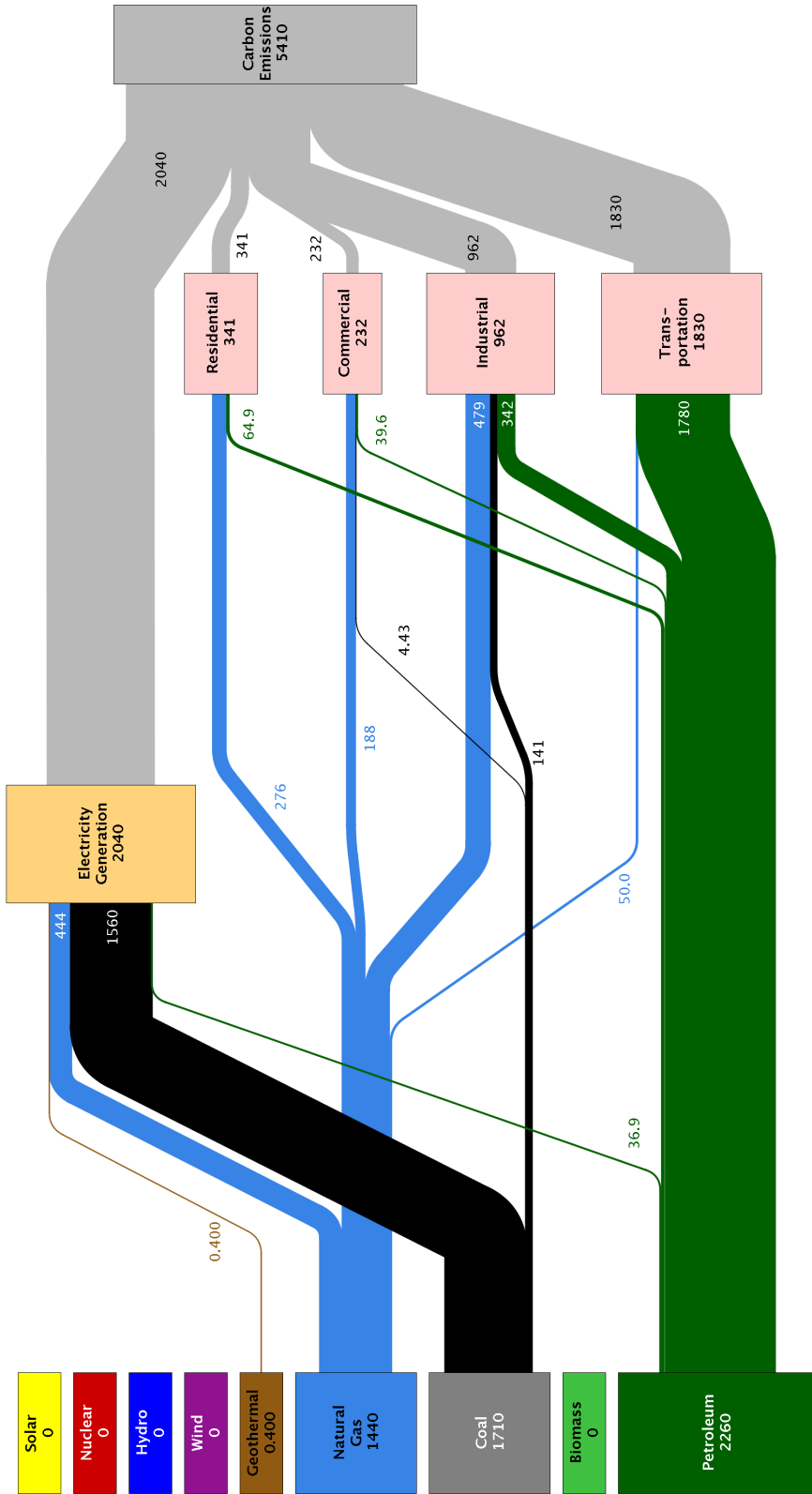
Estimated U.S. Energy Consumption in 2015: 97.5 Quads



Sources: LLNL, March, 2016. Data is based on DOE/EIA MER (2015). If this information or a reproduction of it is used, credit must be given to the Lawrence Livermore National Laboratory and the Department of Energy, under whose auspices the work was performed. Distributed electricity represents only retail electricity sales and does not include self-generation. EIA reports consumption of renewable resources (i.e., hydro, wind, geothermal and solar) for electricity in BTP-equivalent values by assuming a typical fossil fuel plant heat rate. The efficiency of electricity production is calculated as the total retail electricity delivered divided by the primary energy input into electricity generation. End use efficiency is estimated as 0.68 for the residential sector, 0.65 for the commercial sector, 0.68 for the industrial sector, and 0.18 for the transportation sector. Totals may not equal due to independent rounding. LLNL-TR-410521

Figure 2.3: Flow chart of energy usage in the United States in 2015, developed by Lawrence Livermore National Laboratory under the auspices of the U.S. Department of Energy.

Estimated U.S. Carbon Emissions in 2014: ~5,410 Million Metric Tons



Source: LLNL 2015. Data is based on DOE/EIA-0035(2015-03), March, 2015. If this information or a reproduction of it is used, credit must be given to the Lawrence Livermore National Laboratory and the Department of Energy, under whose auspices the work was performed. Carbon emissions are attributed to their physical source, and are not allocated to end use for electricity consumption in the residential, commercial, industrial and transportation sectors. Petroleum consumption in the electric power sector includes the non-renewable portion of municipal solid waste. Combustion of biologically derived fuels is assumed to have zero net carbon emissions - the lifecycle emissions associated with producing biofuels are included in commercial and industrial emissions. Totals may not equal sum of components due to independent rounding errors. LLNL-MI-410527

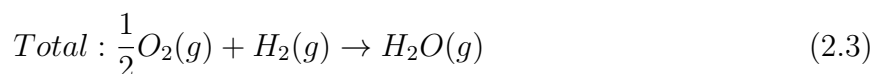
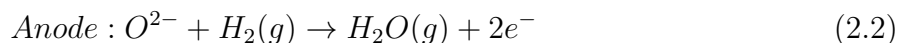
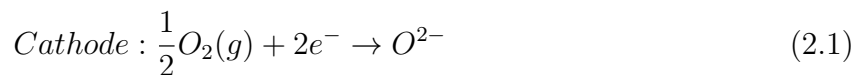
Figure 2.4: Flow chart of carbon emissions in the United States in 2014, developed by Lawrence Livermore National Laboratory under the auspices of the U.S. Department of Energy.

2.2. Solid Oxide Fuel Cells

Solid oxide fuel cells (SOFCs) are electrochemical energy conversion devices that directly convert the chemical energy of a fuel into electrical energy and heat. Unlike traditional power plants that rely on heat cycles, SOFCs are not limited by Carnot efficiencies, allowing them to achieve efficiencies around 60% for direct power generation, or as high as 85% in combined heat and power (CHP) systems that utilize the waste heat for useful purposes. SOFCs are modular in nature, allowing for distributed power generation with systems generating hundreds of kilowatts, whereas traditional power plants typically operate on the scale of hundreds of megawatts owing to economy of scale. The modular nature facilitates the use of SOFCs in CHP systems, allowing for the full utilization of their potential for high efficiency power generation.

2.2.1 Operation

SOFCs are layered devices consisting of a two porous electrodes separated by a solid electrolyte layer as shown in Fig. 2.5. Fuel gas flows to the anode, while the cathode is exposed to oxygen or air. Oxygen gas in the cathode is reduced to oxygen ions which are incorporated into the electrolyte and diffuse to the anode, where they oxidize the fuel. The half reactions at each electrode as well as the overall reaction for a device operating with hydrogen as a fuel are as such:



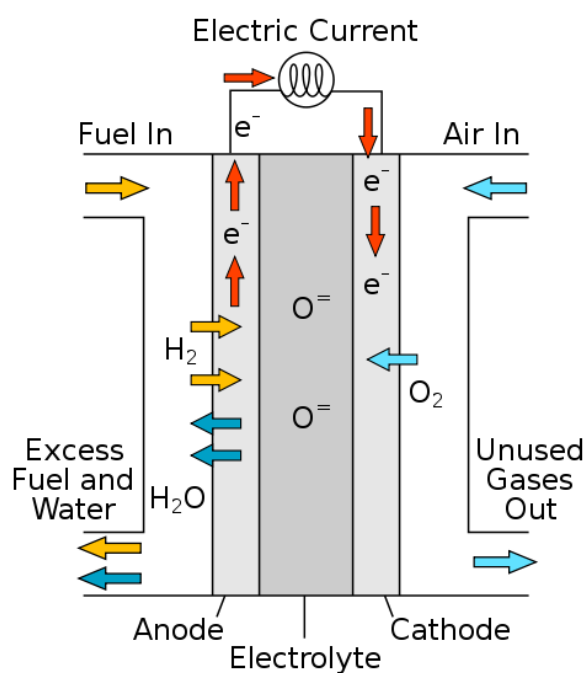


Figure 2.5: Diagram of the structure and operation of a SOFC.

The flux of negatively charged oxygen ions across the electrolyte must be balanced by a flux of electrons in the opposite direction. Using an electrolyte material with high ionic conductivity but minimal electronic conductivity forces the electric current through an external load. In commercial systems, multiple cells are stacked together with interconnect layers separating the cells. The interconnects provide electrical connectivity between cells, while separating the gas environments and providing gas flow channels to distribute fuel to the anode and air or oxygen to the cathode. Multiple stacks can then be combined into larger modules depending on the power requirements of an application.

Other investigations look at running devices in reverse as solid oxide electrolysis cells (SOECs) that use electricity to create a fuel from feedstock, or as reversible solid oxide cells (ReSOCs). [2–4] These devices operate in electrolysis mode to convert excess electricity to a chemical fuel that can later be converted back to electricity by operating in fuel cell mode,

allowing for large scale energy storage that could assist in load-leveling issues inherent with emerging renewable energy technologies such as wind and solar.

2.2.2 Advantages and Challenges

The primary advantage of fuel cells over traditional combustion-based power generation is the high efficiency enabled by the direct conversion between chemical and electrical energy, as explained above. However, many types of fuel cells exist, each defined by the material of the electrolyte. SOFCs have several advantages over other types of fuel cells for many applications. Many other fuel cells use liquid electrolytes that restrict device geometry and can cause corrosion issues. [5,6] The solid electrolyte in SOFCs eliminates corrosion concerns, and enables a wide range of geometries including tubes. [7–9] SOFCs also have the highest operating temperature of all fuel cells. All of the key processes in SOFCs are thermally activated, so high operating temperatures (traditionally 800-1000 °C) are necessary in order to achieve sufficient reaction rates in the electrodes and ionic conductivity in the electrolyte. This high temperature eliminates the need for precious metal catalysts such as platinum used in many other fuel cells. It also provides the ability to internally reform and directly operate on carbon-containing fuels including natural gas and carbon monoxide, giving SOFCs much better fuel flexibility. Finally, the high temperature facilitates the extraction of useable heat generated from the exothermic reaction of oxidizing the fuel, increasing efficiencies in CHP systems.

On the other hand, high operating temperature exacerbate many of the barriers to the commercialization of SOFCs. Traditional operating temperatures are too high for the use of cheap materials such as glasses and stainless steels for gas seals and interconnects. High operating temperatures also accelerate degradation and shorten device lifetime. While the high temperature increases the mobility of oxygen in the electrolyte layer, it also increases

cation mobility, accelerating coarsening and the possible formation of unwanted interfacial layers between the electrolyte and electrode materials. Additionally, stresses caused by the mismatch of the thermal expansion coefficients of the layers can degrade interfaces when the devices are cycled between operating and ambient temperatures. For these reasons, major efforts are being made to develop SOFCs capable of operating at intermediate temperatures.

2.3. SOFC Materials and Microstructures

2.3.1 Electrolytes

The electrolyte is a dense layer that transports oxygen ions from the cathode to the anode, but prohibits the flow of gasses and electrons. Electrolyte materials must therefore have high ionic conductivity and low to negligible electronic conductivity. They must also be able to be fired to full density in order to prevent gas transport or electrical shorting through pores or pinholes. Electrolytes are in contact with both electrode materials as well as both air and fuel atmospheres during operation, so they must exhibit good chemical stability with both electrode materials as well as under oxidizing and reducing environments. Finally, matching the thermal expansion coefficients of the electrolyte and electrodes is important to minimize the risk of cracking or delamination when transitioning between processing, operating, and ambient temperatures.

Perovskites and fluorite-related structures, shown in Fig. 2.6 and 2.7, respectively, often support high concentrations of oxygen vacancies, particularly through doping, making them ideal candidates for electrolytes. The conductivities of several common electrolyte materials are shown in Fig. 2.8. Yttria-stabilized zirconia (YSZ) is the prototypical SOFC electrolyte material. However, its conductivity below 800 °C is too low for efficient fuel cell operation. The two most common alternatives to YSZ for intermediate temperatures are

doped ceria materials, such as gadolinia-doped ceria (GDC or CGO), and strontium- and magnesium-doped lanthanum gallate (LSGM). [10] The primary drawback of GDC is a significant electronic conductivity under reducing conditions that can decrease device voltage and efficiency. [10] The studies in this thesis work focused on electrolytes made from YSZ and LSGM.

2.3.1.1 Yttria-Stabilized Zirconia (YSZ)

Doping ZrO_2 with 8 mol% Y_2O_3 stabilizes the high temperature cubic fluorite structure, while simultaneously maximizing ionic conductivity through the addition of oxygen vacancies. As such, 8 mol% YSZ, sometimes referred to as fully-stabilized YSZ, is the most common electrolyte composition. YSZ and other doped zirconia materials show minimal electronic conductivity for oxygen partial pressures as high as 10^2 atm down to as low as 10^{-25} – 10^{-20} atm, giving them good stability under typical fuel cell operation. [12] High ionic conductivity, negligible electronic conductivity, and prevalence in literature make YSZ an excellent electrolyte for high temperature SOFC studies.

2.3.1.2 Strontium- and Magnesium-Doped Lanthanum Gallate (LSGM)

Like YSZ, LSGM shows negligible electronic conductivity and good stability under both oxidizing and reducing conditions. The solubility range and electrochemical properties of LSGM have been well characterized. [13–15] It exhibits an ionic conductivity significantly higher than that of YSZ, with the maximum conductivity generally achieved with 10-20% doping for both strontium and magnesium. [13] The primary difficulty with LSGM is its reactivity with common electrode materials, including $\text{La}_{1-x}\text{Sr}_x\text{MnO}_3$ (LSM), $\text{La}_{1-x}\text{Sr}_x\text{Cr}_{1-y}\text{Fe}_y\text{O}_{3-\delta}$ (LSCF), and materials containing cobalt. [10] Additionally, the substitution of nickel on gallium sites significantly increases the electronic conductivity of LSGM and can lead to the

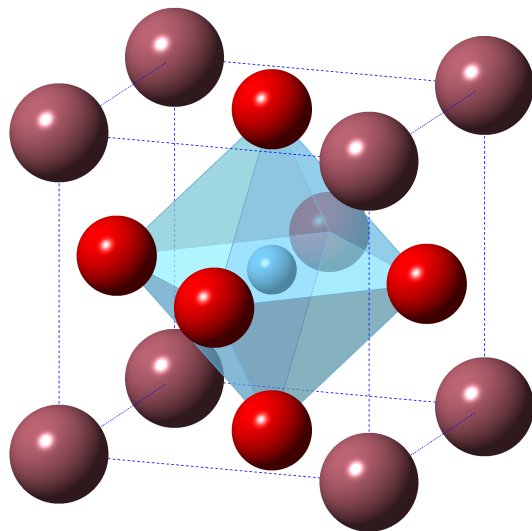


Figure 2.6: Ideal cubic perovskite structure ABO_3 , with A-site cations on the corners, a B-site cation in the cube center, and oxygen on the face centers.

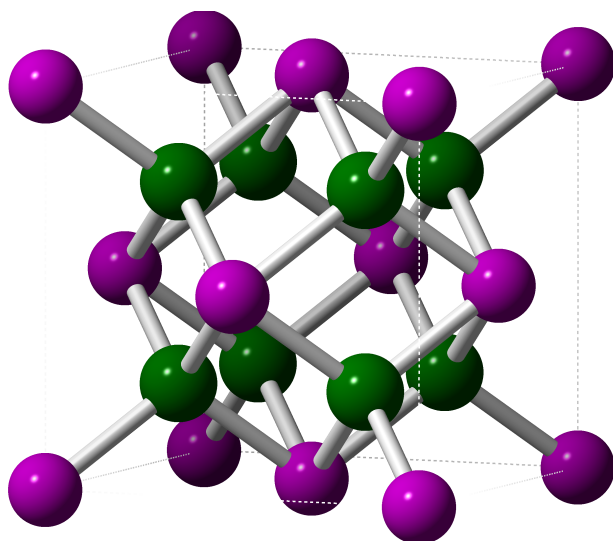


Figure 2.7: AX_2 Fluorite crystal structure. Cations form an FCC lattice, with anions occupying the tetrahedral sites.

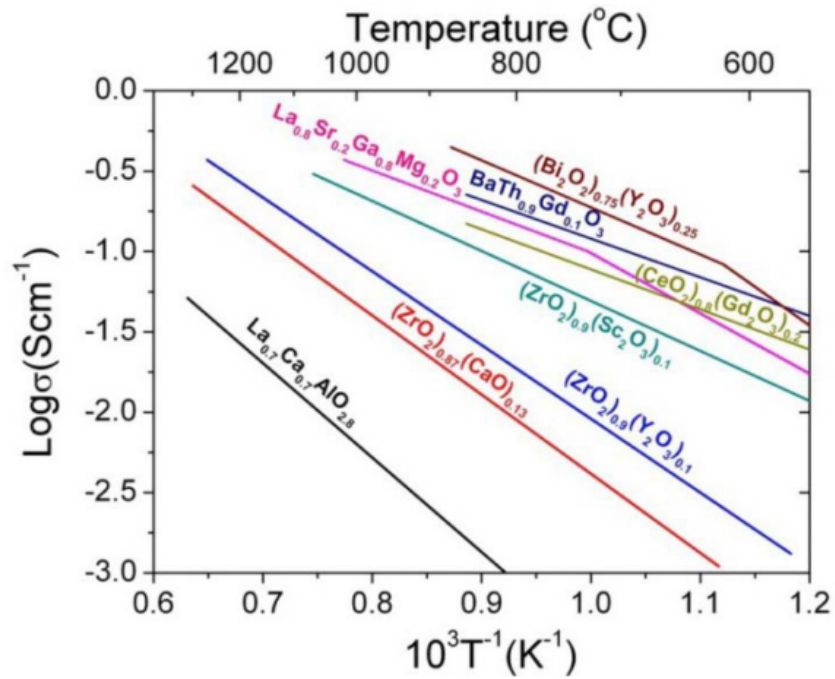


Figure 2.8: Conductivity of several common SOFC electrolyte materials. [11]

formation of interfacial phases, drastically reducing device performance. [15–17] As such, it is vital to identify electrode materials that show good performance and long term stability with LSGM in order to make LSGM-based cells viable.

2.3.2 Electrodes

The cathode and anode materials act as catalysts for the half reactions listed in Eq. 2.1 and 2.2 respectively. The cathode must be stable under oxidizing conditions, while the anode must be stable under the reducing conditions of the fuel. Electrode materials also must be electronically conductive to supply or collect the electrons involved in the half reactions. As discussed above, the electrode materials must be chemically compatible with the electrolyte to prevent the formation of unwanted phases during processing and operation, and all layers must have similar thermal expansion coefficients to prevent interfacial stresses from forming.

When considering stacking cells, both electrodes must also be chemically compatible with the interconnect material. Finally, the electrode structure must be porous in order to allow for oxygen and fuel to flow to the reaction sites, and to remove the exhaust gasses in the anode.

2.3.2.1 Electronic Conductors

Traditional electrode materials exhibit high electronic conductivity, but little to no oxygen ion conductivity. Nickel oxide is commonly used in the anode, where it is reduced to nickel metal during operation. Although nickel-based anodes show high performance with hydrogen as a fuel, they are susceptible to sulfur impurities and the deposition of carbon known as coking when operating on other fuels such as natural gas. Improved resistance to sulfur and coking can be achieved through the use of some conductive oxides as anode or anode support layers, though nickel-based anodes remain the most prevalent. [18–21] The most common cathode materials are doped perovskites and perovskite-related materials, such as LSM, where cation vacancies lead to intrinsic p-type conductivity through small polaron hopping that can be increased by the substitution of Sr^{2+} on La^{3+} sites, compensated by the oxidation of Mn^{3+} to Mn^{4+} . [22]

If the electrode material does not conduct oxygen ions, the reaction can only take place where the electrolyte, electrode, and pore phases meet and are able to transport oxygen ions, electrons, and gas species, respectively. The lines where all three phases meet is known as the triple phase boundary (TPB). The linear-specific TPB resistance (conductance per unit length) is determined by the electrode and electrolyte materials, temperature, and gas composition. For given materials and operating conditions, however, electrode performance can be optimized by increasing the TPB density by modifying electrode microstructure as discussed in section 2.3.2.3.

2.3.2.2 Mixed Ionic-Electronic Conductors (MIECs)

The use of electrode materials with both electronic and oxygen ion conductivity, particularly in the cathode, has led to major improvements in SOFC performance. The ability to transport oxygen ions through the bulk of the electrode material allows the electrode half reaction to take place on the surface of the electrode particles, rather than only at the TPB. [23] It is common to characterize these materials by both their oxygen surface exchange coefficient k and their oxygen bulk diffusivity D . [24] Methods typically used to measure these parameters include ion-exchange depth profiling (IEDP) on bulk or thin film samples, [25,26] and conductivity relaxation on bulk samples. [26,27] A utilization length describing the thickness of the region in an electrode actively contributing to the reaction can be established, and is proportional to $\sqrt{D/k}$. [23] In a material limited by surface exchange, the utilization length will be large in order to maximize the surface area available for reaction. If a material is instead limited by diffusion, the utilization length will be small in order to limit the distance an oxygen ion must diffuse to reach the electrolyte.

Because the reaction is not limited to the TPB, the linear-specific TPB resistance does not apply to MIEC electrodes with particle sizes smaller than the utilization length. Instead, the performance of electrode materials is often reported as the area-specific surface resistance R_S . The surface resistance is commonly measured using thin films of electrode material on electrolyte substrates as discussed in section 2.4, so it is generally more sensitive to oxygen surface exchange than to diffusion. A comparison of common MIEC cathode materials is shown in Fig. 2.9. Again, perovskites are the most common, including the (La,Sr)(Co,Fe)O₃ family of La_{0.6}Sr_{0.4}FeO_{3- δ} (LSF), La_{0.6}Sr_{0.4}Fe_{0.8}Co_{0.2}O_{3- δ} (LSFC), La_{0.6}Sr_{0.4}Co_{0.8}Fe_{0.2}O_{3- δ} (LSCF), and La_{0.6}Sr_{0.4}CoO_{3- δ} (LSC). [28] Other examples include Sm_{0.5}Sr_{0.5}CoO_{3- δ} (SSC) and Ba_{0.5}Sr_{0.5}Co_{0.8}Fe_{0.2}O_{3- δ} (BSCF), which has shown excellent power densities in devices with samarium-doped ceria (SDC) electrolytes and SDC-Ni anodes. [29]

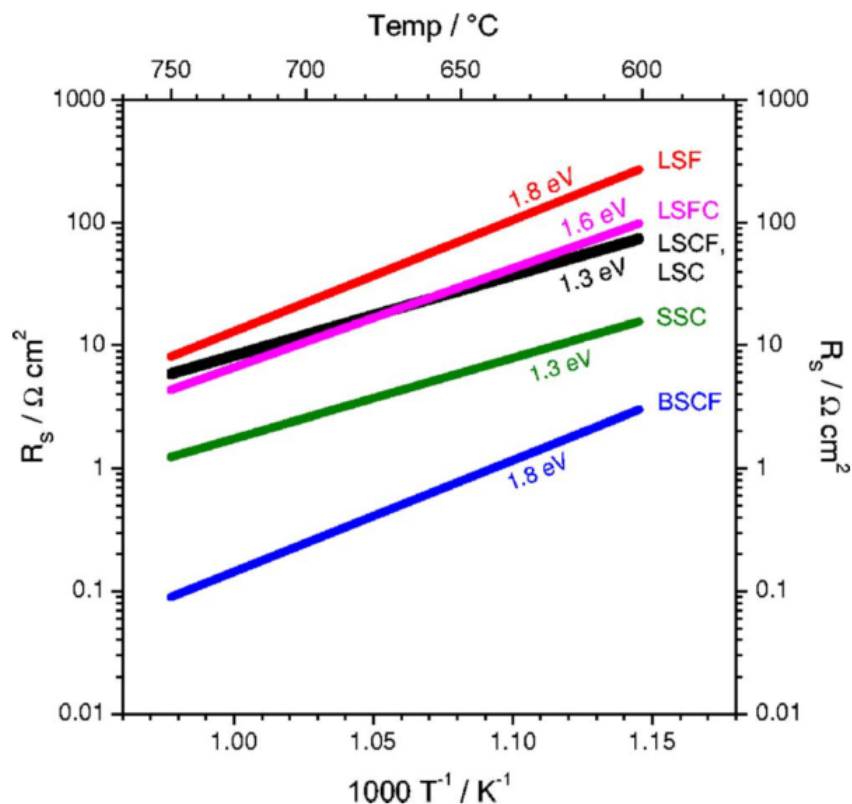


Figure 2.9: Area-specific surface resistance versus inverse temperature for common cathode materials using thin film electrodes. [28]

Another group of materials that has recently gained attention is the Ruddlesden-Popper series $A_{n+1}B_nO_{3n+1}$ ($A = \text{La, Nd, Pr}$) ($B = \text{Ni, Cu, Co}$), where n typically ranges from one to three. These layered structures consist of single layers of AO rocksalt separating groups of n layers of ABO_3 perovskite, as shown in Fig. 2.10. These structures are capable of supporting both oxygen interstitials in the rocksalt layers, and oxygen vacancies in the perovskite layers. [30] As n decreases, the rocksalt layers become more dominant, and the oxygen deficiency decreases, to the point where $n=1$ has a slight oxygen excess. Lanthanum and praseodymium nickelates ($A = \text{La, Pr}$) ($B = \text{Ni}$) are the most common, and show good performance as cathode materials, though their electronic conductivities are somewhat lower than typical perovskite oxides. [30–33]

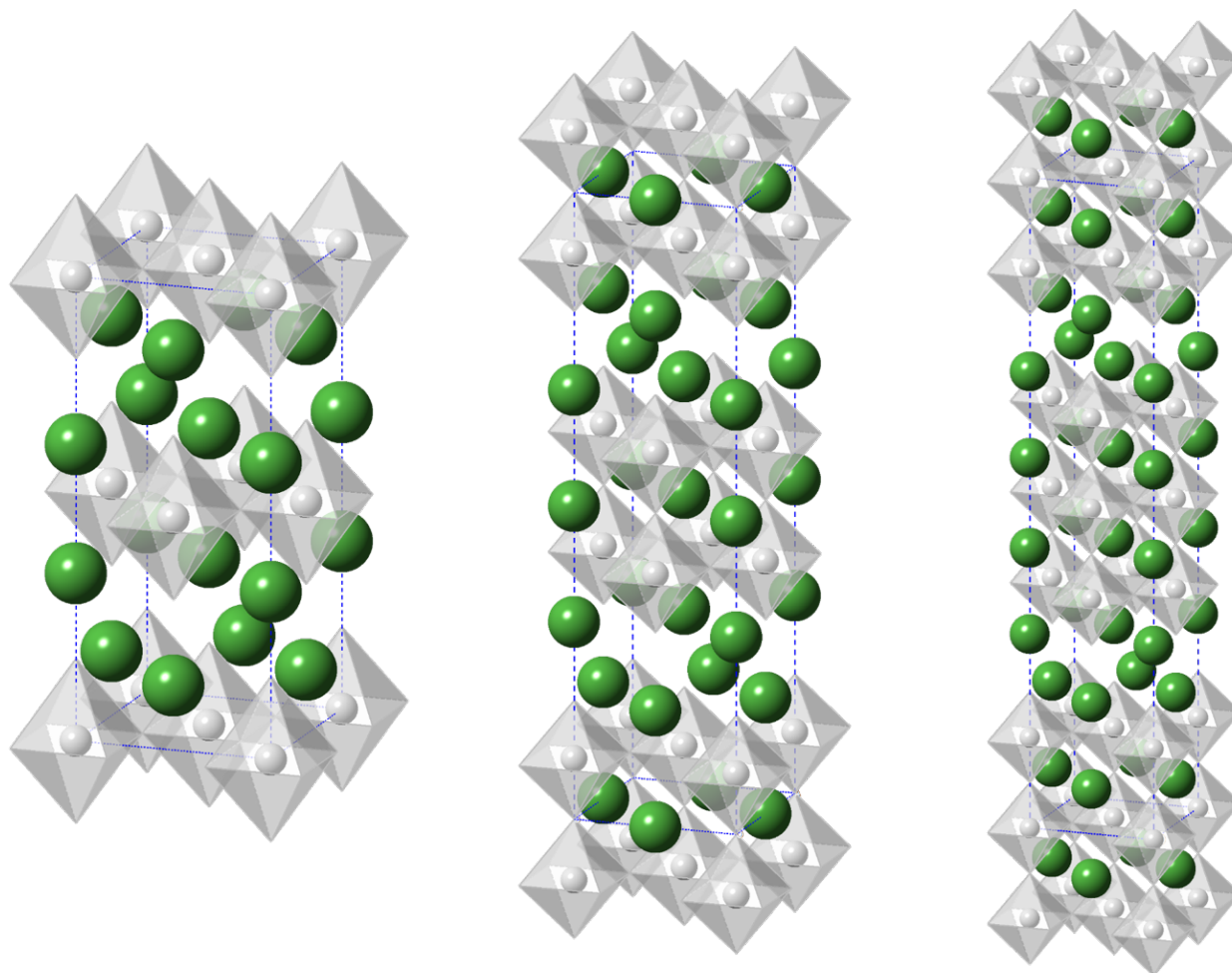


Figure 2.10: Ruddlesden-Popper series $A_{n+1}B_nO_{3n+1}$ crystal structure for $n=1$ (left), $n=2$ (center), and $n=3$ (right). A-site atoms are shown in green, and BO_6 octahedra in grey. The structure consists of AO rocksalt layers separating n layers of ABO_3 perovskite. Unit cells are outlined by dashed blue lines.

2.3.2.3 Microstructures

The microstructure of electrodes must be optimized to balance gas transportation, phase connectivity, mechanical stability, and reaction site density. There are three main types of cathode structures, illustrated in Fig. 2.11. The first is a simple porous layer of the electrode material. This microstructure is primarily reserved for MIEC electrode materials,

as the only TPB exists at the interface between the electrode layer and the dense electrolyte layer. In order to provide TPB throughout the thickness of the cathode layer, a composite microstructure consisting of an ion conductor (typically the electrolyte material) mixed in with the electronic conductor, as shown in Fig. 2.11b, is often employed. In this structure, connectivity of each phase (ion conductor, electron conductor, pore) is necessary to ensure the added TPB density remains active. For example, if a particle of the ion conductor is isolated from the dense electrolyte layer, no oxygen incorporated at the TPB involving that particle can travel to the anode to react with the fuel. Modifying the porosity and relative amounts of the electron and ion conductor phases can optimize the structure to achieve the highest density of active TPB. [34]

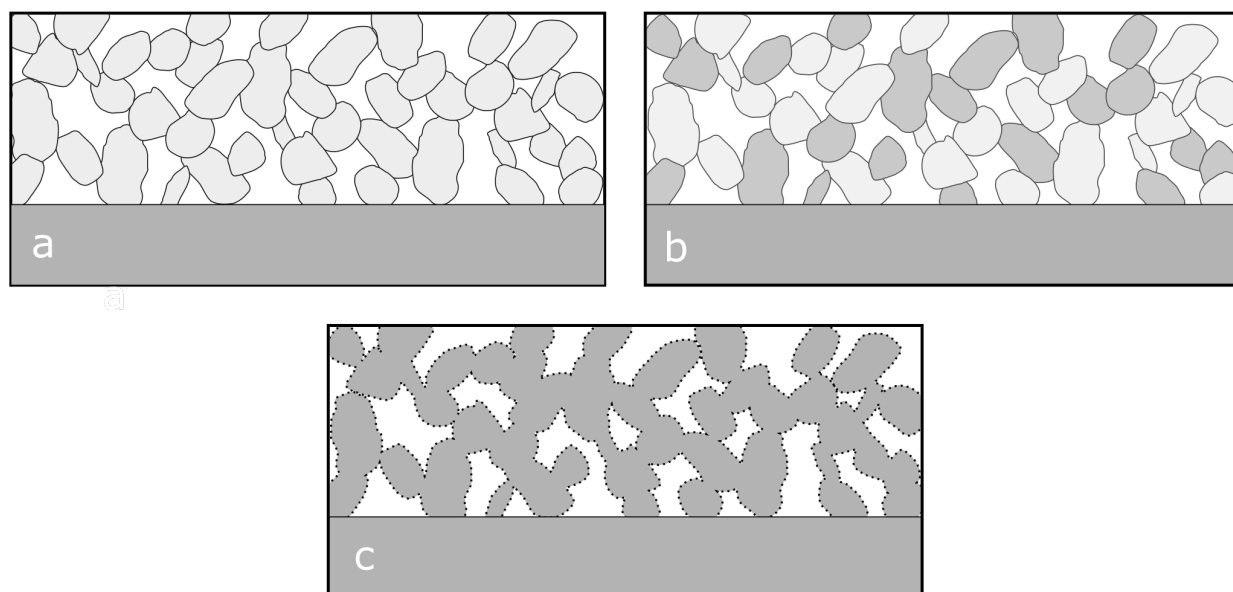


Figure 2.11: Representation of electrode microstructures: (a) porous layer of electrode material, (b) porous composite mixture of electrode and electrolyte materials, and (c) porous electrolyte scaffold infiltrated with electrode nanoparticles from solution. Light grey represents the electrode material, dark grey the electrolyte material, and white is pore. The dense electrolyte layer is shown on the bottom.

Another emerging microstructure is an infiltrated electrode, shown in Fig. 2.11c. A porous ionically conductive scaffold is fired, then a solution containing a stoichiometric ratio of metal nitrates is infiltrated into the electrode, coating the scaffold. Subsequent drying and firing in air then converts the nitrates to a network of oxide nanoparticles on the surface of the scaffold. Infiltrated geometries have shown high performance in many systems, including Ni/YSZ [35–37] and Ni/LSGM [18] anodes, and LSCF/SSC, [38] LSCF/GDC and SSC/GDC, [39] and Pr_2NiO_4 [33, 40] cathodes. Compared to more conventional composite mixture structures, infiltrated electrodes allow for lower loading of the infiltrated material, and support lower firing temperatures. The small infiltrate particles provide high TPB and surface area densities, but also accelerate coarsening, making long-term stability a concern.

2.4. Patterned Electrode and Combinatorial Studies

Materials properties and performance are best compared when geometric factors such as microstructures have been removed. For SOFC electrode materials, this corresponds to the TPB linear-specific resistance for electronically-conducting electrodes, and area-specific surface resistance for MIEC electrode materials. The TPB resistance of metal electrodes such as nickel has been measured by pressing a bent wire into the surface of an electrolyte pellet, [41–47] and TPB resistance in an actual electrode has been measured using 3D reconstruction methods to measure TPB density, [48] but the most common method is to vapor deposit thin films of electrode material onto electrolyte substrates, and then lithographically pattern the electrode layer, creating well-defined electrodes with known area and TPB length.

2.4.1 Triple Phase Boundary Linear-Specific Resistance

Patterned electrode studies have measured the TPB linear-specific resistance in several systems, including Pt/YSZ, [49, 50] Ni/YSZ, [51, 52] Ni/LSGM, [52] LSM/YSZ, [53] and $(\text{La}_{0.87}\text{Ca}_{0.13})_{0.95}\text{MnO}_3$ (LCM)/YSZ. [54] Multiple patterns with different TPB lengths but a constant electrode-electrolyte interface area are often used in order to eliminate possible contribution from effects including porosity or pinholes in the electrode film, wavy interfaces, and oxygen transport through the bulk of the thin electrodes. In particular, LSM exhibits enough oxygen ion conductivity at high temperatures to enable bulk transport of oxygen through very thin films. [55, 56]

2.4.2 Area-Specific Surface Resistance

As discussed above, the reaction is not limited to the TPB when using MIEC electrode materials, so TPB linear-specific resistance is not relevant. Instead, it is common to measure the area-specific surface resistance (conductance per unit of electrode area). The process is essentially identical to the measurement of TPB linear-specific resistance using lithographically patterned thin film electrodes, often using circular electrodes with various diameters.

2.4.3 Combinatorial Measurements

While patterned thin film methods have proven to be reliable, the sample preparation requires the deposition of high quality films with appropriate composition and microstructure, along with lithographic patterning. IEDP measurements of surface exchange and diffusivity can utilize easily prepared bulk samples, but involve high temperature isotope exchange and secondary ion mass spectrometry (SIMS) profiling steps. A faster and simpler measurement method is desired to facilitate more rapid screening of the key properties for a wide range of

materials and compositions. Some combinatorial methods have been applied to oxide materials, [57, 58] including a method using a limited-contact geometry to characterize porous cathodes and to find the optimal composition of a mixed LSM/YSZ cathode. In general, however, the application of combinatorial measurements to oxide SOFC electrode materials has been limited due to the lack of appropriate measurement techniques.

2.5. $\text{LaO}_{1.5}\text{-GaO}_{1.5}\text{-NiO}$ Quasi-Ternary System

The $\text{LaO}_{1.5}\text{-GaO}_{1.5}\text{-NiO}$ quasi-ternary system provides a useful simplification of the LSGM-Ni phase space. The details of this system are applicable to SOFCs, because it contains LaGaO_3 (the parent phase of LSGM), NiO (a common anode material which is reduced to nickel metal during cell operation), and the Ruddlesden-Popper series of lanthanum nickel oxide phases which have shown promising performance as SOFC cathodes. [30, 31] The thermodynamic phase compatibility in this phase space can provide insight into interactions during processing and long term stability between LSGM electrolytes and lanthanum nickel oxide and NiO electrodes.

2.5.1 Bounding Quasi-Binary Systems

The three bounding quasi-binary systems have been well characterized, and form the starting point for investigations into the quasi-ternary system. The $\text{GaO}_{1.5}\text{-LaO}_{1.5}$ system (Fig. 2.12) contains two line compound binary oxides: LaGaO_3 , and monoclinic $\text{La}_4\text{Ga}_2\text{O}_9$, which is a common impurity in the synthesis of LSGM. [59] LaGaO_3 has an orthorhombic structure at room temperature (LGO), but undergoes a transition to a rhombohedral structure (LGR) around 420 K. It has also been shown that the incorporation of nickel can stabilize the rhombohedral structure. [60, 61] Three eutectics also appear, with the lowest appearing between

Table 2.1: Effective ionic radii compiled by Shannon. [64] CN = coordination number, IR = ionic radius, LS = low spin, HS = high spin.

| Ion | CN | IR [pm] |
|------------------|------|---------|
| La ³⁺ | 6 | 117.2 |
| | 12 | 150 |
| Ga ³⁺ | 6 | 76 |
| Ni ²⁺ | 6 | 83 |
| Ni ³⁺ | 6 LS | 70 |
| | 6 HS | 74 |

GaO_{1.5} and LaGaO₃ at 1596 K (1323 °C). Therefore, melting behavior in the gallium-rich corner of the quasi-ternary system is expected. The only bounding binary system that shows any solid solubility is the NiO-GaO_{1.5} system (Fig. 2.13). Table 2.1 shows that gallium and nickel have similar ionic radii, whereas lanthanum is much larger. The similar ionic radii of nickel and gallium and the ability for Ni²⁺ to be reduced to Ni³⁺ allow for significant substitution between the two, with negligible substitution involving lanthanum. Although there is no significant solubility of nickel in Ga₂O₃, both the NiGa₂O₄ spinel and NiO halite phases show considerable solid solubility ranges at higher temperatures.

The LaO_{1.5}-NiO system contains the Ruddlesden-Popper series La_{n+1}Ni_nO_{3n+1}, as shown in Fig. 2.14. As mentioned above, the n=1-3 phases have shown promising performance as SOFC cathodes. At lower temperatures, the n=1, n=2, n=3, and n=∞ (LaNiO₃) are all stable. Each phase appears as a line compound, indicating no solubility between lanthanum and nickel. As temperature increases, higher n phases decompose into lower n phase and NiO. Above 1500 K, La₂NiO₄ (n=1) is the only stable binary oxide in the LaO_{1.5}-NiO system.

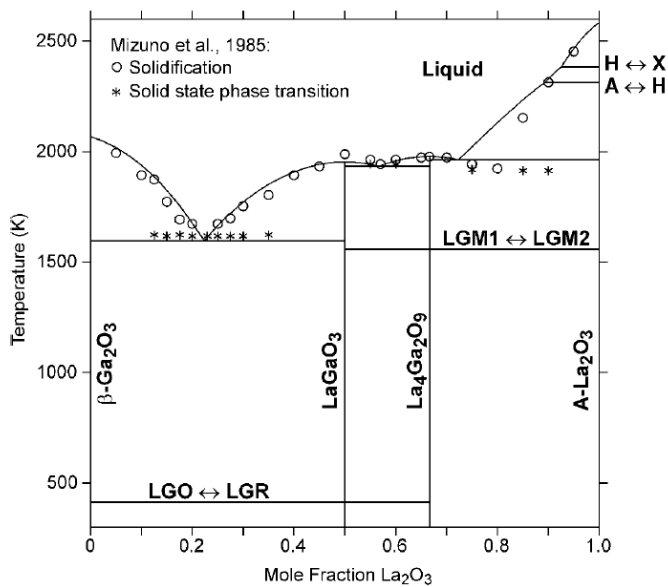


Figure 2.12: $\text{GaO}_{1.5}\text{-LaO}_{1.5}$ quasi-binary phase diagram calculated by Zinkevich et al. [62] with experimental solidification measurements overlaid.

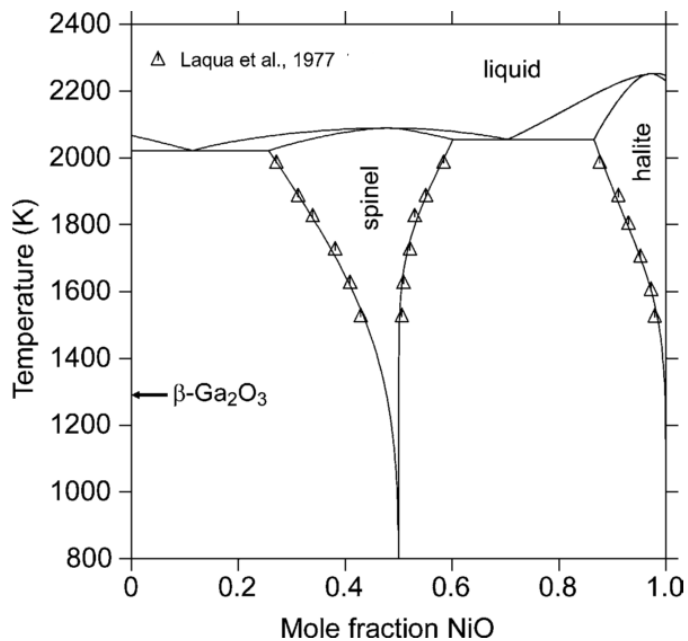


Figure 2.13: $\text{Ga}_2\text{O}_3\text{-NiO}$ quasi-binary phase diagram calculated by Zinkevich et al. [63] with experimental points overlaid. Note that a 1:1 mole fraction of Ga_2O_3 to NiO places the spinel NiGa_2O_4 at 0.5 mole fraction NiO.

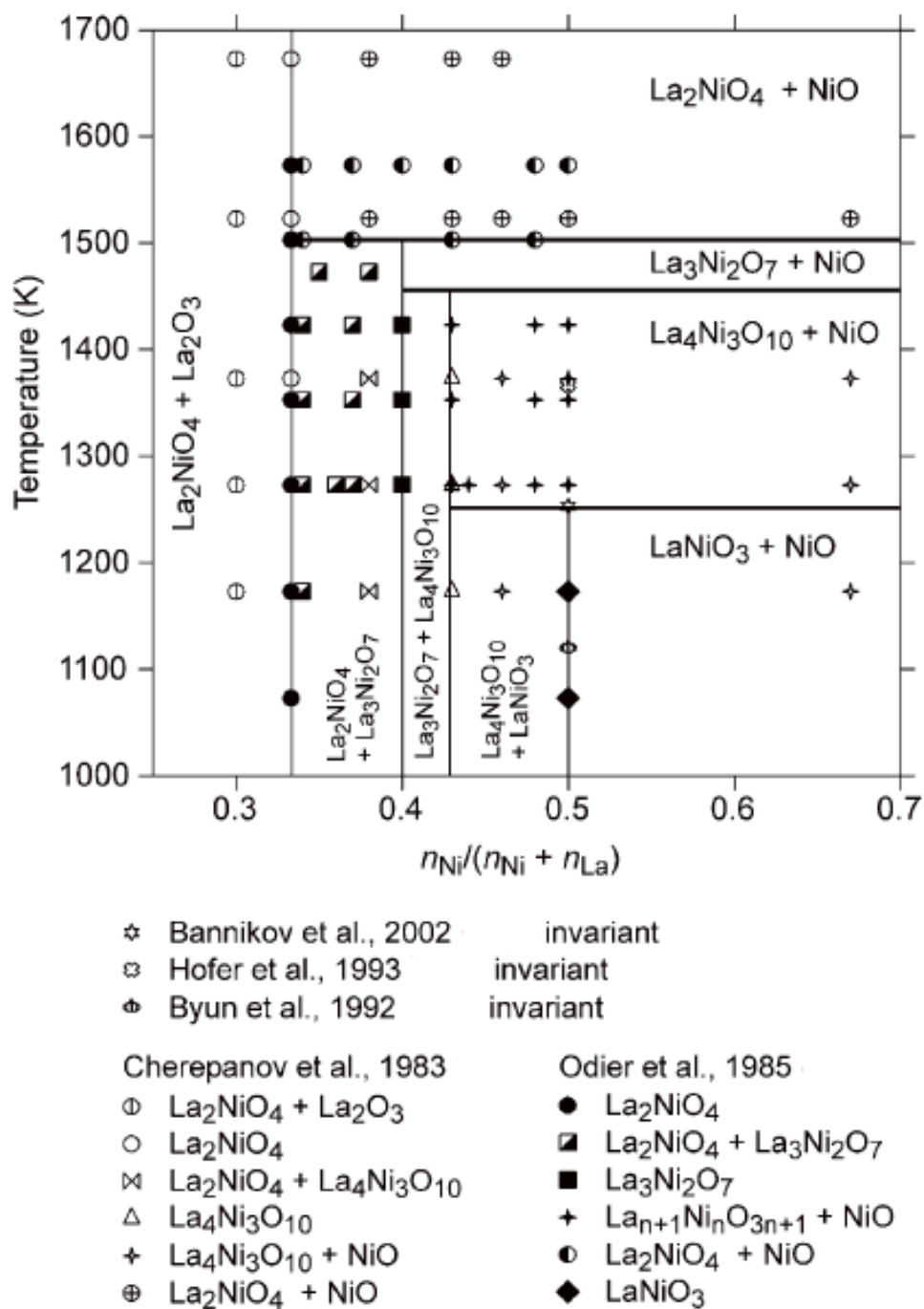


Figure 2.14: $\text{LaO}_{1.5}$ -NiO quasi-binary phase diagram calculated by Zinkevich et al. [65] with experimental observations overlaid.

2.5.2 Quasi-Ternary System

Previous work has been done to map out an isothermal section of the $\text{LaO}_{1.5}\text{-GaO}_{1.5}\text{-NiO}$ quasi-ternary phase diagram at 1300 °C. The first diagram by Hrovat et al. reported tie lines extending from LaGaO_3 to NiO and La_2NiO_4 . [66] This was later significantly revised by Solak et al. through calculations followed by experimental observations. [67] The revision introduced solubility ranges corresponding to substitutions between gallium and nickel, and a phase in the gallium-rich corner with an overall composition of $\text{LaNiGa}_{11}\text{O}_{19}$. Additionally, $\text{La}_4\text{Ni}_3\text{O}_{10}$, which is normally not stable above 1200 °C, was observed to be stabilized by the addition of gallium. A similar effect has also been observed in the stabilization of the $k=1$ and $k=2$ phases of $\text{Zn}_k\text{In}_2\text{O}_{k+3}$ phases through the substitution of gallium for indium. [68, 69] A tie line between $\text{La}_4\text{Ga}_2\text{O}_9$ and gallium-stabilized $\text{La}_4\text{Ni}_3\text{O}_{10}$ also disrupted the previously reported compatibility between LaGaO_3 and La_2NiO_4 . Later work applying the CALPHAD-method (Calculation of Phase Diagrams) theoretical fitting to the system along with further numerical modeling introducing minor adjustments including a varying lanthanum content in $\text{La}_2(\text{Ni,Ga})\text{O}_4$, and concluded that there is no equilibrium between LaGaO_3 and La_2NiO_4 , resulting in the diagram in Fig. 2.15. [70] Overall, much of the work in the quasi-ternary system has been by theoretical calculations and based on limited experimental evidence. Furthermore, recent works sintered mixtures of LSGM and La_2NiO_4 and reported no observation of the formation of interfacial phases. [71, 72] A more detailed experimental study to establish the phase compatibility relationships and solubility limits in the $\text{LaO}_{1.5}\text{-GaO}_{1.5}\text{-NiO}$ quasi-ternary system would provide more insight into the processing of LSGM electrolytes with NiO anodes and $\text{La}_{n+1}\text{Ni}_n\text{O}_{3n+1}$ cathodes.

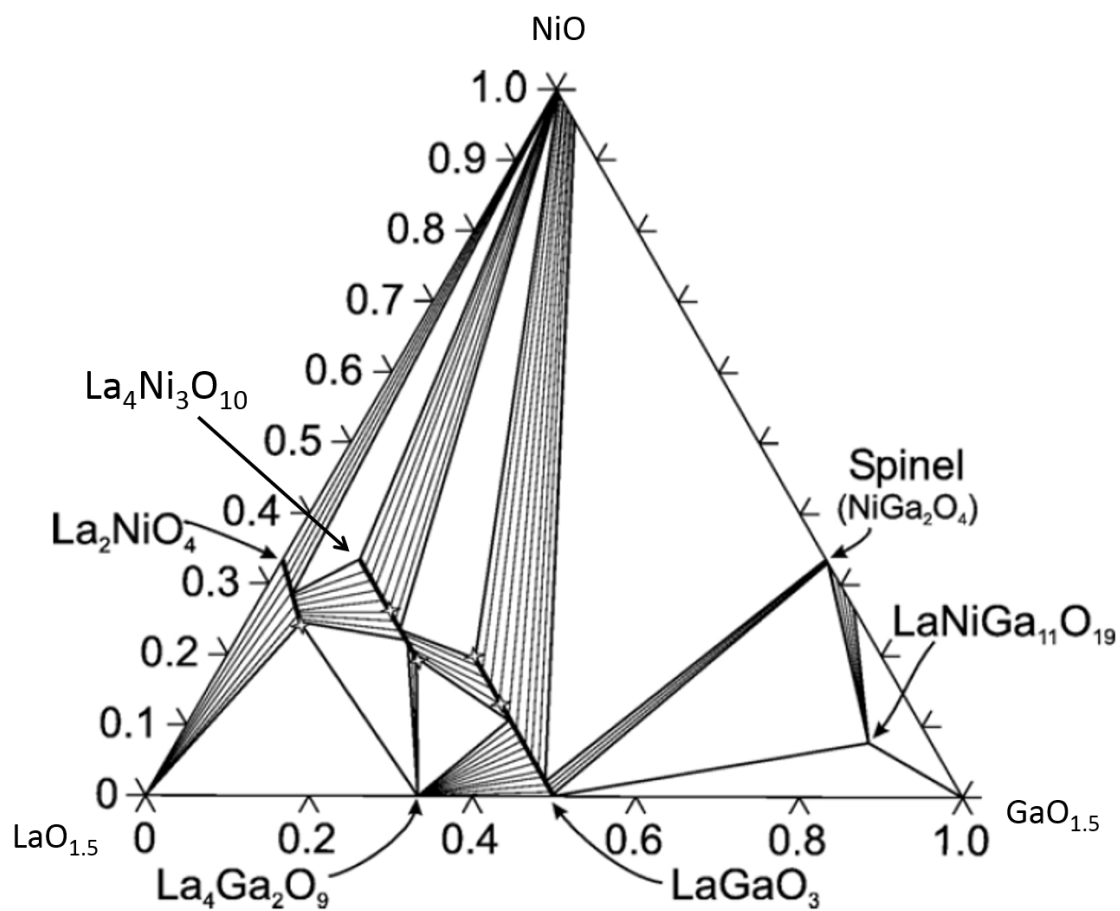


Figure 2.15: Isothermal section of the $\text{LaO}_{1.5}$ - $\text{GaO}_{1.5}$ - NiO quasi-ternary phase diagram at $1300\text{ }^\circ\text{C}$ from CALPHAD theoretical fitting of experimental observations. [70]

CHAPTER 3

Sample Preparation and Characterization

3.1. Solid State Synthesis

Solid state synthesis was used to prepare pellet samples of various materials. Commercial precursor powders were dried overnight in a furnace between 150 and 200 °C in order to eliminate adsorbed water before weighing out the desired ratio of powders to within ± 0.5 mg (2-2.5 g total powder for each sample). One exception was La_2O_3 powder, which spontaneously forms hydroxides and carbonates when exposed to air. [73] For samples containing lanthanum, La_2O_3 powder was heated to 1000 °C at 7 C/min and held for one hour to decompose the powder to its oxide before quenching inside a desiccator to prevent the formation of hydroxides upon cooling. Thermogravimetric analysis performed on powder prepared by this method showed no mass loss up to 900 °C, compared to a mass loss around 15% for undried powder, as shown in Fig. 3.1. The first two mass loss steps have been attributed to the loss of water, while the third has been attributed to the loss of carbon dioxide, through processes shown in Fig. 3.2. If La_2O_3 powder that has been exposed to air for long periods of time is not decomposed back to the oxide and is weighed according to the molar mass of La_2O_3 , the sample composition will be substantially lanthanum-deficient compared to the

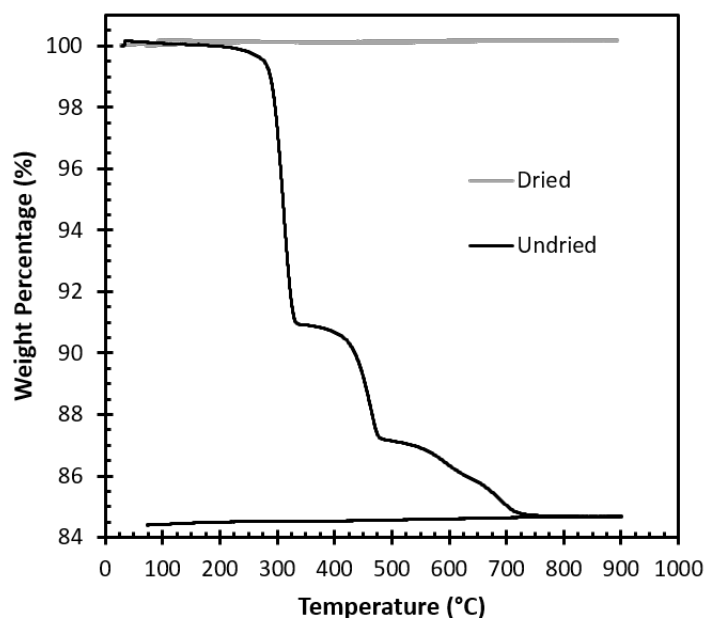


Figure 3.1: Thermogravimetric analysis of La_2O_3 powder with and without treatment at 1000°C for one hour to decompose the powder to its oxide form.

target composition.

The dried and weighed powders were mixed manually under acetone or ethanol using an agate mortar and pestle, then allowed to dry. Approximately one gram of the powder mixture was pressed with 115 MPa of uniaxial pressure for approximately 60 seconds in a steel die with a diameter of half an inch using a Carver hydraulic press. Stearic acid dissolved in isopropanol was applied to the die cavity and punches before pressing to act as a lubricant

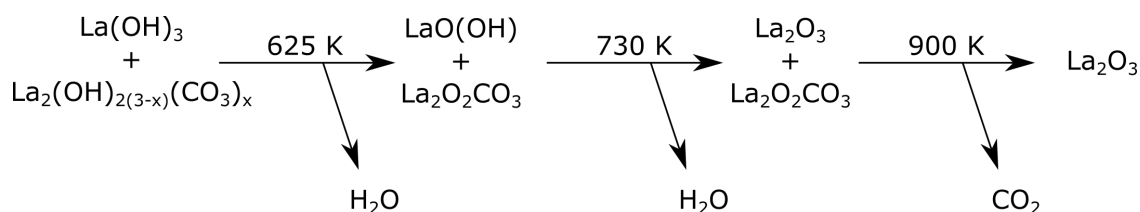


Figure 3.2: Decomposition steps of lanthanum hydroxides and carbonates to lanthanum oxide corresponding to the three mass loss steps visible in Fig. 3.1. Adapted from Bernal et al. [73]

and release agent. The resulting pellets were buried in the rest of the powder inside a small lidded alumina crucible that was nested inside two larger lidded crucibles in order to prevent contamination from the walls of the alumina crucible and to minimize the volatilization of cations from the pellet that could alter the composition. An initial calcination of 20 hours at 1000 °C to start the reaction was followed by regrinding and mixing the pellet powder before pressing a new pellet and sintering, using the same pressing methods, sacrificial powder, and alumina crucible assembly described above. All heating and cooling steps used a rate of 5 °C/min in order to minimize the formation of thermal stresses from uneven heating or cooling, both in the pellet and in the furnace insulation, heating elements, and thermocouple. The temperature and time of the final sintering depended on the material being synthesized, but generally ranged from 1100-1400 °C for 4-72 hours, ending with slow cooling at 5 °C per minute or fast cooling by removing the crucible assembly from the furnace at temperature, then disassembling the crucibles and allowing the inner crucible to rapidly cool in air. This rapid air quenching was used to lock in the high temperature phase behavior of the samples without allowing for any significant cation diffusion to take place during cooling.

3.2. X-ray Diffraction and Whole Pattern Fitting

X-ray diffraction (XRD) was used to identify the phases present in samples, as well as their lattice parameters and relative weight fractions. Some early measurements were performed using a Rigaku DMAX diffractometer. However, the Rigaku DMAX uses a nickel filter which can interfere with measurements of nickel-containing materials, so the majority of measurements used a Scintag XDS2000 diffractometer. Parameters for a typical scan were a 2θ range of 20-70°, with a step size of 0.05°, and a dwell time of 3-4 seconds. These parameters were sufficient to detect multiple peaks for each phase with adequate distinction between peaks and background variability, while maintaining a scan time around one hour. The

surfaces of pellets used for XRD measurements were ground using silicon carbide paper to ensure a flat surface and to eliminate any surface effects. For scans seeking accurate lattice parameters, sample powders were mixed with approximately 20 wt% of an internal silicon standard (Alfa Aesar, 99.9985%), and the silicon peaks were used as references to correct for instrument error. The resulting spectra were analyzed using whole pattern fitting (WPF) using MDI Jade software. When fitting the full 2θ range, a 6th order polynomial background was fit. For many measurements of relative weight fractions, smaller 2θ ranges containing the most intense peak for each phase present and a parabolic background were used for WPF.

3.3. Phase Stability Investigations

Several methods using XRD are available for determining phase boundaries and solubility limits when mapping phase boundaries and phase diagrams. Each has advantages and disadvantages, and each was applied in this work.

3.3.1 Conventional Phase Analysis

The simplest method examines the phases present at various compositions, and identifies solubility limits and phase boundaries between compositions showing dissimilar phases. This method requires a large number of samples to be prepared, does not determine phase boundaries with precision, and is susceptible to detection limits of XRD methods. However, it does not require previous knowledge of the phase space, and can be applied to previously unexplored phase spaces or when other methods prove difficult.

3.3.2 Vegard's Law

If accurate measurements of lattice parameters can be obtained, Vegard's Law can yield precise phase boundary measurements. For phases that follow Vegard's Law, the lattice parameters vary linearly with the composition of the phase. When the solubility limit is exceeded, the slope will change, or go flat if the phase rule requires fixed compositions for all phases present (e.g., in a triphasic region of an isothermal ternary phase diagram). Thus, the inflection points in plots of lattice parameter versus composition correspond to various phase boundaries. Once the Vegard's Law behavior of a phase is established, the composition of that phase present in other multi-phase samples can be found simply by measuring the lattice parameters of that phase. In order to ensure accurate lattice parameter measurements, an internal silicon standard is typically mixed with sample powders, as discussed in section 3.2. Vegard's Law can determine phase boundaries much more precisely than conventional phase analysis, but is most beneficial when some information exists about which solid solutions are present in the phase space of interest.

3.3.3 Disappearing Phase Method

The disappearing phase method is similar to Vegard's Law, but relies on tracking the weight fraction of each phase rather than lattice parameters. Plotting the relative phase weight fractions versus composition in a multi-phase region and extrapolating to the points where one or more phases disappear(s) yields the boundary between two regions. Determining the composition of each phase in a multi-phase region is more difficult using the disappearing phase method compared to Vegard's Law approaches where lattice parameters are indicative of composition. However, the disappearing phase method is a useful alternative when changes in lattice parameters are difficult to track, whether because of narrow single-phase regions,

complicated crystal structures, or very small lattice parameter changes.

The disappearing phase method was used to identify the position of vertices of triphasic regions in a ternary phase space. Figure 3.3 shows an example of two triphasic regions in a portion of an imaginary ternary system, where the vertices residing on the line of solid solubility labeled 1 are to be determined, but the other vertex locations are known. In region, A, the vertex resides at one extreme of the range of solid solubility. A series of samples in the triphasic region along the dashed line can be used to identify the solubility limit, thus identifying the location of the vertex. Region B is somewhat more complicated, as there is no way to identify a line in region B that will intersect the vertex. Instead, a series of samples cutting across the triphasic region can be used to identify the boundaries between region B and the bounding biphasic regions, as marked with red asterisks in Fig. 3.3. If the locations of the other vertices of region B are known, tie lines can be extrapolated from the vertices, through the triphasic-biphasic boundaries (red asterisks), to the point where they intersect solid solution 1, identifying the position of that vertex. If X , Y , and Z are the amounts of the three components of the diagram, and solution 1 resides at a constant level of X , the composition of the solid solution 1 vertex of region B can be calculated as:

$$Y_3 = Y_1 + (Y_2 - Y_1) \frac{X_3 - X_1}{X_2 - X_1} \quad (3.1)$$

$$Z_3 = Z_1 + (Z_2 - Z_1) \frac{X_3 - X_1}{X_2 - X_1} \quad (3.2)$$

Here, (X_1, Y_1, Z_1) is the composition of the known vertex, (X_2, Y_2, Z_2) is the composition of the triphasic-biphasic boundary, and (X_3, Y_3, Z_3) is the composition of the vertex being identified. In region A, if the position of the bottom right vertex is known, the same method can determine the vertex residing on solid solution 2 employing the same samples used to determine the solubility limit of solution 1. It should be noted, however, that extrapolating

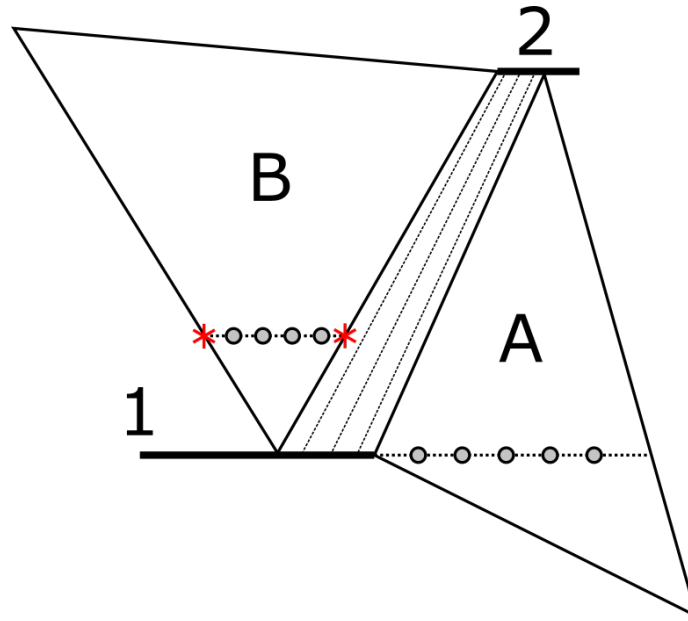


Figure 3.3: Example portion of a ternary phase diagram illustrating two ways to identify vertices of triphasic regions.

through a triphasic/biphase border far from the unknown vertex will amplify the uncertainty of the measurement.

3.4. Electrical Characterization

3.4.1 Four-Point Probe Electrical Conductivity

The room temperature conductivity σ (or resistivity ρ) of some samples was measured using the four-point geometry shown in Fig. 3.4, with geometric corrections for a disc as outlined by Smits and listed in Eq. 3.3: [74]

$$\rho = \frac{V}{I} w C \left(\frac{d}{s} \right) F \left(\frac{w}{s} \right) \quad (3.3)$$

Here, I is the current applied between the two outer probes, V is the measured voltage between the two inner probes, and w is the thickness of the disc. C is a correction factor based on the ratio of the disc diameter d and the probe spacing s :

$$C = \frac{\pi}{\ln 2 + \ln \left(\frac{(d/s)^2 + 3}{(d/s)^2 - 3} \right)} \quad (3.4)$$

F is a correction factor based on the ratio of the disc thickness and probe spacing. Values of F were determined by fitting a sixth order polynomial to the factors reported by Smits and listed in Table 3.1. [74] The voltage was measured for currents ranging from -0.1 mA to 0.1 mA, and the slope provided V/I for Eq. 3.3. The measurement process was repeated after rotating the sample by 90° , and then repeated two more times on the other face of the disc, again rotating 90° between measurements. This provided four measurements in total in order to eliminate effects from any anisotropy in the sample.

The measured conductivity of each sample was also corrected for porosity, determined by calculating the relative density of each sample. The pellets were weighed and their thicknesses and diameters were measured with a micrometer in order to calculate the density of each sample. The theoretical density was determined using measured lattice parameters from XRD and assuming a formula unit equal to the overall composition synthesized. Dividing the actual density by the theoretical density yielded relative densities typically around 70% (30% porosity) for the samples measured using this method. The pore volume fractions p were then used to correct the measured conductivities using the Bruggemann symmetric model, where pores were treated as an insulating phase in a composite structure: [75]

$$\sigma_c = \frac{\sigma_0}{1 - \frac{3}{2}p} \quad (3.5)$$

Here, σ_c is the corrected conductivity and σ_0 is the measured conductivity.

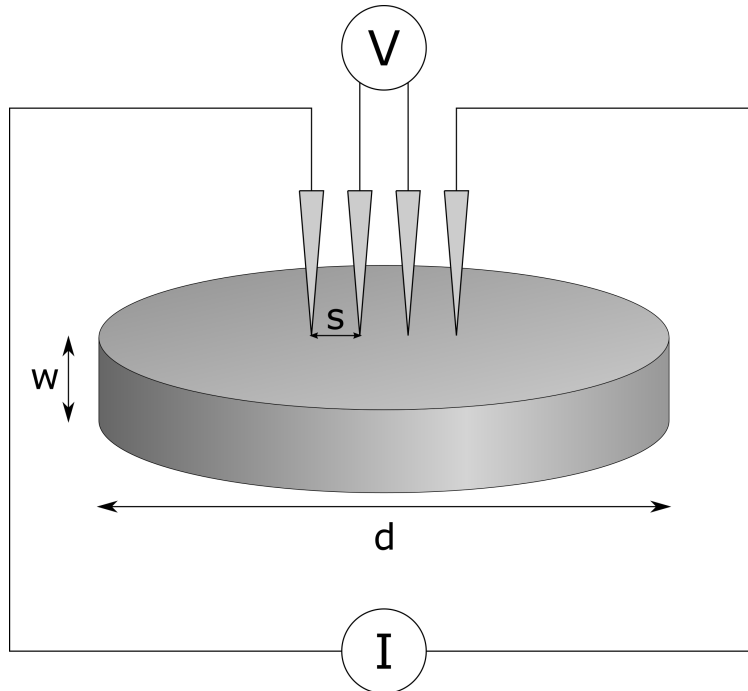


Figure 3.4: Diagram of the four-point probe geometry used for room temperature electrical conductivity measurements.

Table 3.1: Resistivity correction factor $F(w/s)$ for four-point conductivity measurements on samples of finite thickness w using a probe spacing s as illustrated in Fig. 3.4. Adapted from Smits. [74]

| w/s | $F(w/s)$ |
|---------|----------|
| 0.4 | 0.9995 |
| 0.5 | 0.9974 |
| 0.5555 | 0.9948 |
| 0.5250 | 0.9898 |
| 0.7143 | 0.9798 |
| 0.8333 | 0.9600 |
| 1.0 | 0.9214 |
| 1.1111 | 0.8907 |
| 1.25 | 0.8490 |
| 1.4286 | 0.7938 |
| 0.16666 | 0.7225 |
| 2.0 | 0.6336 |

3.4.2 Electrochemical Impedance Spectroscopy

Electrochemical impedance spectroscopy allows for the separation and characterization of multiple elements or processes that contribute to a system's overall electrical resistance. A sinusoidal voltage is applied to a system, and the resulting sinusoidal current is measured. Repeating the measurement over a range of frequencies yields the frequency-dependent impedance, a complex analogue to DC resistance determined by a time-dependent version of Ohm's Law:

$$V(t) = I(t) * Z(\omega) \quad (3.6)$$

Here, V is the voltage, I is the current, t is time, Z is the impedance, and ω is the frequency. Solving for impedance and inserting the sinusoidal nature of the voltage and current yields

$$Z(\omega) = \frac{V(t)}{I(t)} = \frac{V_m \sin(\omega t + \phi_V)}{I_m \sin(\omega t + \phi_I)} = Re(Z) + jIm(Z) = |Z| \cos(\theta) + j|Z| \sin(\theta) \quad (3.7)$$

$$\text{where } \theta = \phi_V - \phi_I \quad (3.8)$$

$$\text{and } |Z| = \frac{V_m}{I_m} \quad (3.9)$$

Here, ϕ_V and ϕ_I are the phase angles of the voltage and current respectively relative to some reference. Equation 3.7 illustrates the two most common ways to report impedance. The first is the real part $Re(Z)$ relating to the in-phase component of the voltage and current, and the imaginary part $Im(Z)$ relating to the out-of-phase component. The second is the amplitude $|Z|$ and the phase angle θ between the voltage and current.

Different processes contributing to a system's total impedance, including ion diffusion, electrochemical reactions, and gas transport operate on different characteristic time scales, and thus respond at different frequencies. When the frequency of the applied voltage is too high for a process to respond, its contribution is lost, similar to a material becoming trans-

parent to electromagnetic waves above its plasma frequency. When the frequency matches the characteristic frequency of a process, the resonance increases the phase angle, introducing a large imaginary component. Plots of the imaginary component or phase angle versus frequency (Bode plots) show peaks corresponding to the various processes at their characteristic frequencies, as shown in Fig. 3.5. Alternatively, plots of the $Im(Z)$ vs. $Re(Z)$ (Nyquist plots) typically show characteristic semi-circular arcs for each process, as shown in Fig. 3.6.

The impedance response is commonly analyzed using equivalent circuit models. The impedance of a resistor is equal to its resistance, with no imaginary component. Capacitors have only a negative imaginary component that varies inversely with frequency:

$$I_C = C \frac{dV_C}{dt} = C (\omega V_m \cos(\omega t)) = \omega C V_m \sin\left(\omega t + \frac{\pi}{2}\right) \quad (3.10)$$

$$Z_C = \frac{V_C(t)}{I_C(t)} = \frac{V_m \sin(\omega t)}{\omega C V_m \sin\left(\omega t + \frac{\pi}{2}\right)} = -\frac{j}{\omega C} \quad (3.11)$$

Note that j is the imaginary number, and a phase angle reference of $\phi_V = 0$ is used. Inductors are similar to capacitors, but show a positive imaginary component that varies linearly with frequency:

$$V_L = L \frac{dI_L}{dt} = L (\omega I_m \cos(\omega t)) = \omega L I_m \sin\left(\omega t + \frac{\pi}{2}\right) \quad (3.12)$$

$$Z_L = \frac{V_L(t)}{I_L(t)} = \frac{\omega L I_m \sin\left(\omega t + \frac{\pi}{2}\right)}{I_m \sin(\omega t)} = j\omega L \quad (3.13)$$

Because most systems measured have more capacitive contributions than inductive contributions, the negative of the imaginary component is commonly plotted against the real component so that the data reside in the first quadrant. When combining elements in an equivalent circuit, their impedances add using the same rules for resistors in a DC circuit. One of the most common elements is a resistor and capacitor in parallel, which results in perfect semi-circular arcs commonly seen in Nyquist plots. It is also common to replace the

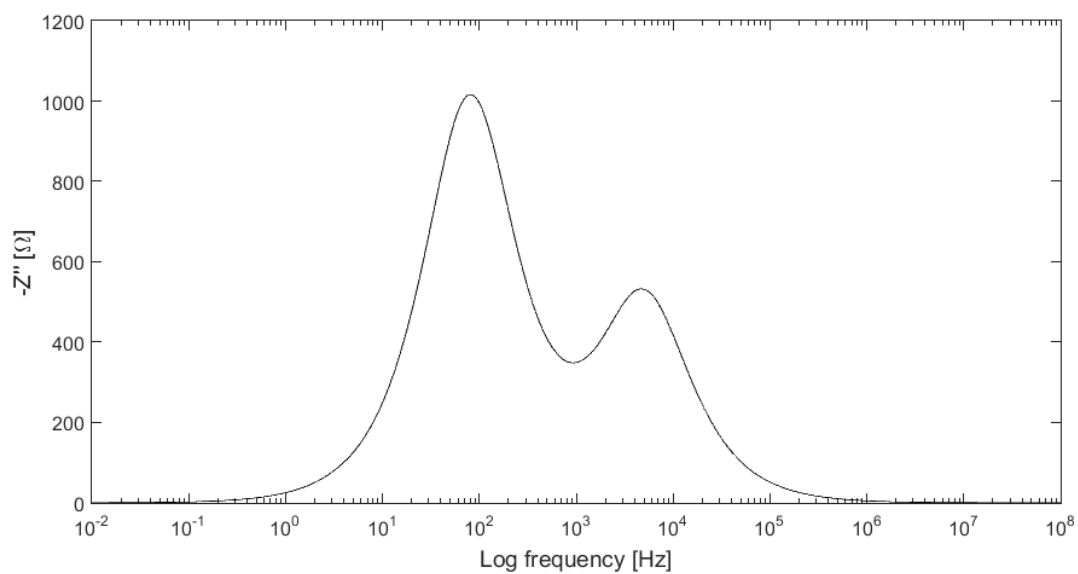


Figure 3.5: Schematic Bode plot of the imaginary component of the impedance as a function of frequency for two (RC) elements.

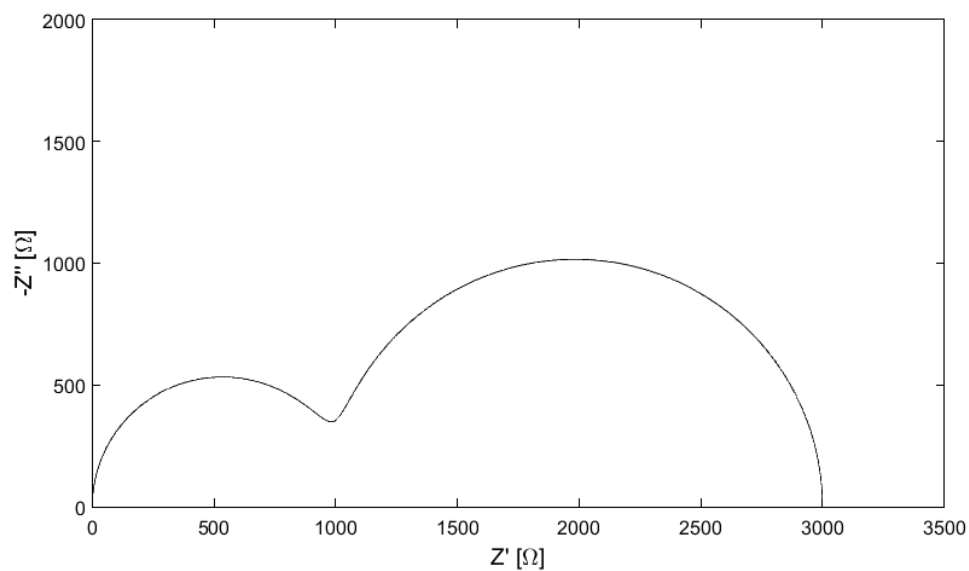


Figure 3.6: Schematic Nyquist plot of the imaginary and real components of the impedance for two (RC) elements.

capacitor with a constant phase element (CPE), which acts as a non-ideal capacitor. Inductors, resistors, and capacitors have constant phase angles of 90° , 0° , and -90° respectively. As suggested by the name, CPEs also have a constant phase angle, but the exact angle can be anywhere between 90° and -90° . When an appropriate equivalent is chosen that can be explained by physical processes, the relative contributions and frequency responses of those processes in a system can be determined.

CHAPTER 4

Hemispherical Electrolyte Probe for Screening Cathode Materials

One of the bottlenecks for identifying new SOFC materials is characterizing materials properties that enable a direct comparison of materials performance without the effects of electrode microstructure. For electronically conductive electrodes, the TPB linear-specific resistivity is commonly measured, while the area-specific surface resistance is commonly measured for MIEC electrodes where the reaction extends beyond the TPB, as discussed in section 2.4. This chapter describes the development of a novel characterization technique that can rapidly compare the performance of potential SOFC electrode materials by measuring TPB linear-specific resistivity (ρ_{TPB}) and area-specific surface resistance (R_S) using a hemispherical electrolyte probe (HEP).

4.1. Overview of Process

The geometry for HEP measurements is shown in Fig. 4.1. It consists of a probe made from an electrolyte material pressed into the flat surface of a dense pellet made from the electrode material of interest. In this work, probes made from 8 mol% YSZ with a tip radius

r of 4.7 mm and a cylindrical section length L of 1.3 mm were custom ordered from Ortech Advanced Ceramics (Sacramento, CA, USA). The probes were tumble polished using a rock polisher with a rubber barrel. The probes were added to the barrel along with size 600 silicon carbide grit (20 μm average particle size) and plastic beads from Kingsley North, Inc. (Norway, MI, USA) and water to fill approximately 1/3 of the barrel. The probes were left in the tumble polisher for one week to smooth out ridges left on the hemispherical surface from the machining of the probes. After polishing, silver paste was applied to the flat end of the probes to ensure good electrical contact. Commercial powders of $\text{La}_{0.8}\text{Sr}_{0.2}\text{MnO}_3$ (LSM), $\text{Sm}_{0.5}\text{Sr}_{0.5}\text{CoO}_{3-\delta}$ (SSC), and $\text{La}_{0.6}\text{Sr}_{0.4}\text{Fe}_{0.8}\text{Co}_{0.2}\text{O}_{3-\delta}$ (LSFC) were pressed into pellets using the procedure outlined in section 3.1, then fired for 4 hours at 1200 $^\circ\text{C}$. A pellet of $(\text{La}_{0.87}\text{Ca}_{0.13})_{0.95}\text{MnO}_3$ (LCM) was synthesized from La_2O_3 , CaO , and MnO_2 powders using solid state synthesis with a calcination step of 12 hours at 1200 $^\circ\text{C}$, and a final firing of 1270 $^\circ\text{C}$ for 24 hours. XRD measurements confirmed phase purity. The resulting relative densities of the pellets are listed in Table 4.1. Both faces of the pellets were ground flat using silicon carbide paper of increasing grit number, followed by polishing with diamond suspensions with particle sizes of 6, 3, and 1 μm , cleaning the surface by sonicating in water before and after each diamond polishing step. Polishing the electrolyte probe and electrode pellets is important to ensure as ideal of a contact as possible in order to obtain accurate measurements.

The electrolyte probe and an electrode pellet were pressed between two gold foils in the sample holder shown in Fig. 4.2. A spring adjusted by a screw compresses the HEP assembly between two alumina rods. An s-type thermocouple (platinum rhodium 10% / platinum) connected to a multimeter was positioned above the assembly in order to ensure accurate temperature measurements. Gold wires connected the gold foils to the coaxial cables of the frequency response analyzer (FRA) through separate alumina tubes coated in platinum

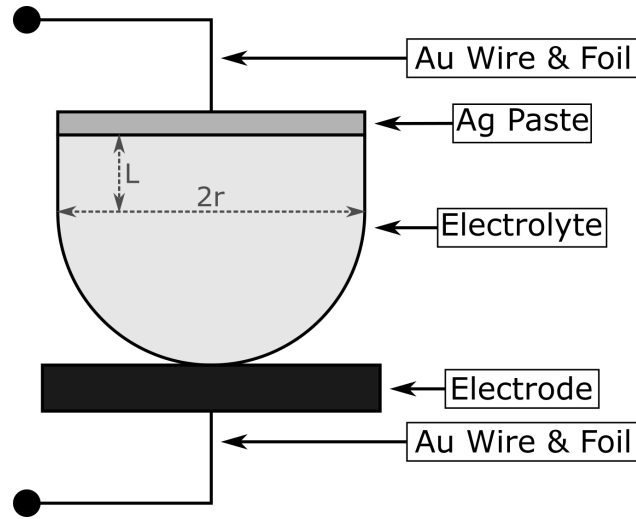


Figure 4.1: Schematic of the geometry used for hemispherical electrolyte probe (HEP) measurements.

paste. During measurements, the platinum coating was connected to ground to shield the lead wires and decrease stray immittance from the apparatus. The contact between the probe and pellet ideally creates a spatially limited circular interface with TPB around the perimeter, as in Fig. 4.3A. The small circular contact on the fairly resistive YSZ probe produces an electrical spreading resistance caused by the bowing of equipotential lines near the contact: [76]

$$R_{Spread} = \frac{\rho}{4a} \quad (4.1)$$

Table 4.1: Relative densities of the electrode pellets along with activation energies from literature and this work for ρ_{TPB} (LSM, LCM) or R_S (SSC, LSFC).

| | Density | Lit. E_a [eV] | HEP E_a [eV] |
|------|---------|-----------------|----------------|
| LSM | 93% | 1.42 [53] | 1.30 |
| LCM | 83% | 1.14 [54] | 1.23 |
| SSC | 89% | 1.6 [28] | 1.49 |
| LSFC | 93% | 1.6 [28] | 1.79 |

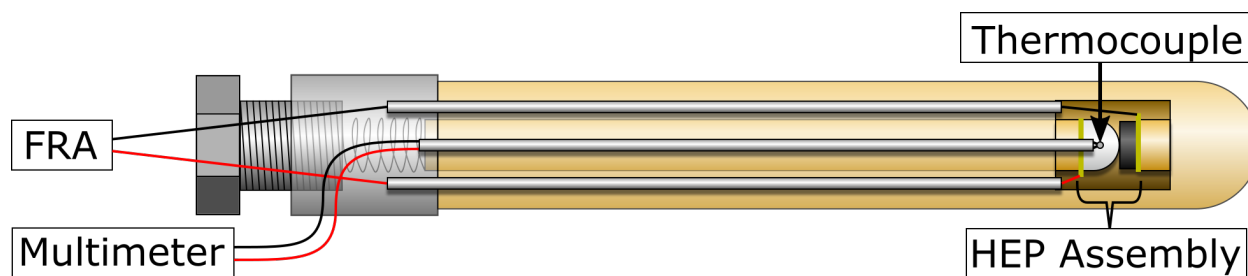


Figure 4.2: Schematic of the sample holder used for HEP measurements. Spring-loaded alumina rods pressed the HEP assembly between gold foils, with a screw to adjust the pressure. Platinum-coated alumina tubes shielded the wires that connected the thermocouple to a multimeter and the gold foils to the frequency response analyzer (FRA).

where ρ is the resistivity of the probe, and a is the contact radius. In reality, the contact is likely more complex, with contact between multiple asperities within the overall contact area, as in Fig. 4.3B. While the details of the contact area are important for the analysis of ρ_{TPB} , it should not have much an effect on the spreading resistance, as Holm showed that as long as there are many points of contact spaced closely together, the overall spreading resistance remains close to the solution in Eq. 4.1. [77]

The electrochemical properties of the HEP assembly were characterized using impedance spectroscopy (section 3.4.2). Measurements were performed using both Agilent Technologies

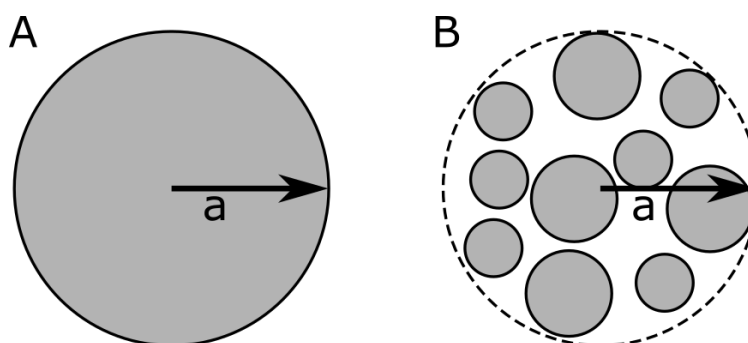


Figure 4.3: Idealized (A) and more realistic (B) contact profile between the electrolyte probe and electrode pellet.

4192A (Santa Rosa, CA, USA) and Solartron 1260 (Berwyn, PA, USA) frequency response analyzers (FRAs) using a voltage amplitude of 50 mV. The Agilent FRA supplied the high frequency data (13 MHz – 1 kHz), while the Solartron FRA supplied the lower frequency data (10 kHz – 10 mHz). In the overlapping frequencies of 1-10 kHz, both data sets were used. For measurements with LSM and LCM, a Solartron 1296 dielectric interface was used in tandem with the 1260 FRA in order to more reliably measure the large impedances associated with those measurements. The measured impedance spectra were fit to equivalent circuits using the Equivalent Circuit for Windows software. [78]

Representative impedance spectra are shown in Fig. 4.4. The high frequency arc (MHz range) was attributed to the response of the ionic conduction in the electrolyte probe, while the lower frequency arcs were attributed to the polarization resistance associated with the electrode reactions. LSFC measurements showed an additional mid-frequency arc that has previously been attributed to ion transfer between the LSFC electrode and YSZ electrolyte. [79] The expected probe resistance is calculated as the sum of the contributions from the spreading resistance in Eq. 4.1 (R_{Spread}), the resistance of the cylindrical section (R_{Cyl}), and the resistance of the hemispherical section (R_{Hemi}). The hemispherical term was calculated by approximating the contact as a truncation of the hemisphere at the point where the probe's cross-sectional radius is equal to the contact area, then integrating over a sphere from its center to the point of truncation:

$$R_{Hemi} = \int_0^{x_f} \frac{\rho dx}{A} = \int_0^{x_f} \frac{\rho dx}{\pi y^2} = \frac{\rho}{\pi} \int_0^{x_f} \frac{dx}{R^2 - x^2} = \frac{\rho}{\pi} \left(\frac{\tanh^{-1} \left(\frac{x_f}{r} \right)}{r} \right) \quad (4.2)$$

for which

$$x_f = x_{(y=a)} = \sqrt{r^2 - a^2} \quad (4.3)$$

resulting in

$$R_{Hemi} = \frac{\rho}{\pi r} \tanh^{-1} \left(\frac{\sqrt{r^2 - a^2}}{r} \right) \quad (4.4)$$

The total probe resistance is therefore

$$R_{Probe} = R_{Cyl} + R_{Hemi} + R_{Spread} = \frac{\rho L}{\pi r^2} + \frac{\rho}{\pi r} \tanh^{-1} \left(\frac{\sqrt{r^2 - a^2}}{r} \right) + \frac{\rho}{4a} \quad (4.5)$$

It should be noted that R_{Hemi} assumes parallel equipotential lines throughout the hemispherical section, whereas R_{Spread} arises from bowed equipotential lines near the contact. However, the spreading resistance effect is mostly confined to a region close to the contact, on the order of a few times the contact diameter. [80] Therefore, as long as the contact is small compared to the size of the probe, the equipotential lines in the bulk of the probe should be essentially parallel.

The resistivity ρ of a slice of one YSZ probe was measured as a function of temperature (Fig. 4.5) to provide accurate values that were in agreement with literature values. [10] The geometric factors r and L are also known, so the only unknown on the right hand side of Eq. 4.5 is the contact radius a . This allows the measured probe resistance to be converted to a contact radius, which is used to normalize the measured polarization resistance to calculate the linear-specific TPB resistance or area-specific surface resistance:

$$\rho_{TPB} = l_{TPB} R_{Pol} = 2\pi a R_{Pol} \quad (4.6)$$

$$R_S = A R_{Pol} = \pi a^2 R_{Pol} \quad (4.7)$$

Equation 4.6 assumes a circular contact with TPB only around the perimeter, while Eq. 4.7 assumes that the whole contact area actively contributes to the reaction. While the reality of the contact is likely more complicated, these assumptions provide a good estimation.

Through this analysis, a single impedance spectrum provides both the polarization resistance and geometric factors necessary to calculate ρ_{TPB} and R_S used to directly compare electrode performance between the different types of electrodes.

4.2. Surface Roughness Using Optical Profilometry

As mentioned above, polishing the surfaces of the probes and pellets is important for obtaining intimate contact. The polished surfaces of a YSZ probe and the LSM and LCM pellets were characterized using a Bruker ContourGT Optical Profiler, which uses white light interferometry to obtain a 3D map of the surface with high resolution. The pellet surfaces were very smooth, with surface roughnesses around 8-15 nm. As shown in Fig. 4.6, however, the probe surface was significantly rougher. The calculated surface roughness was around 1.5-2.0 μm , and the surface contained pits on the order of 5-10 μm deep and 10-50 μm across. This irregular surface likely allowed for gas transport under the electrode/electrolyte contact and increased the TPB length relative to the perimeter of the overall contact. As discussed above, however, the spreading resistance in the electrolyte is not heavily affected by the details of the contact beyond the overall contact size, so the estimation of the contact radius and area using Eq. 4.5 should be accurate.

4.3. Assumptions and Validation

The HEP method relies heavily on obtaining an accurate measure of the contact size from the probe resistance. If the conversion of the probe resistance to a contact radius using Eq. 4.5 is inaccurate, the normalization of the polarization resistance to ρ_{TPB} and R_S will be inaccurate. As such, several experiments were performed in efforts to validate assumptions and the behavior of HEP measurements.

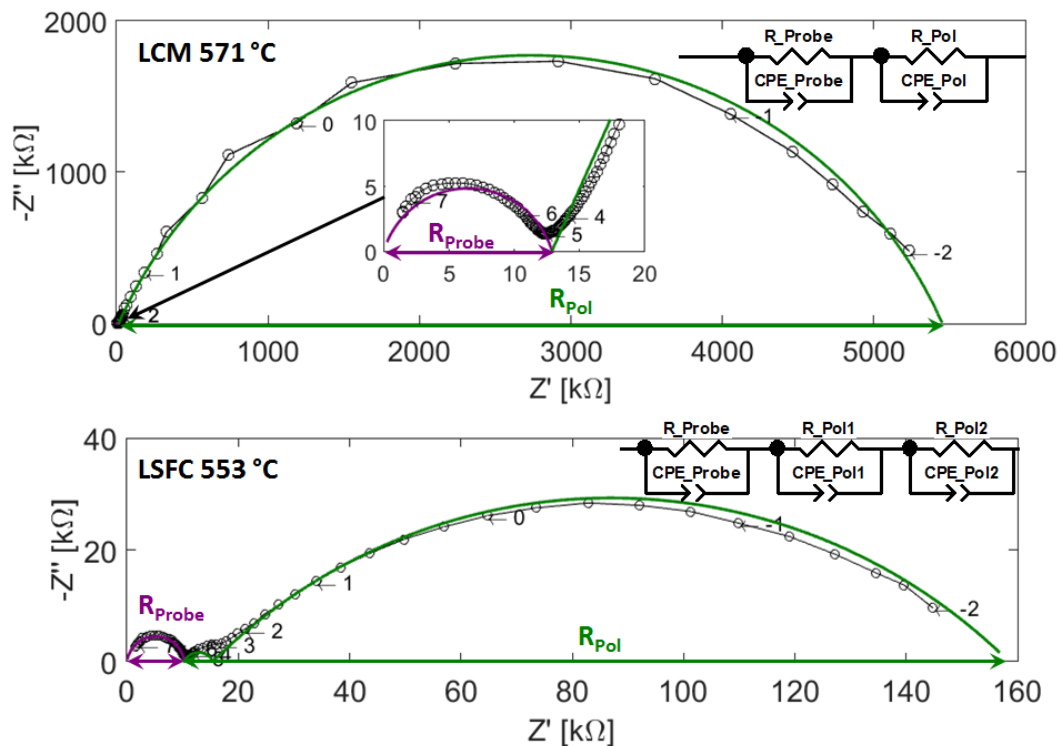


Figure 4.4: Representative HEP impedance spectra for an electronic conductor (LCM, top) and a mixed conductor (LSFC, bottom), with numbers indicating frequency decades. The purple arcs represent the probe contribution, while the green arcs represent the electrode polarization resistance contribution. The equivalent circuits used in each case are also shown.

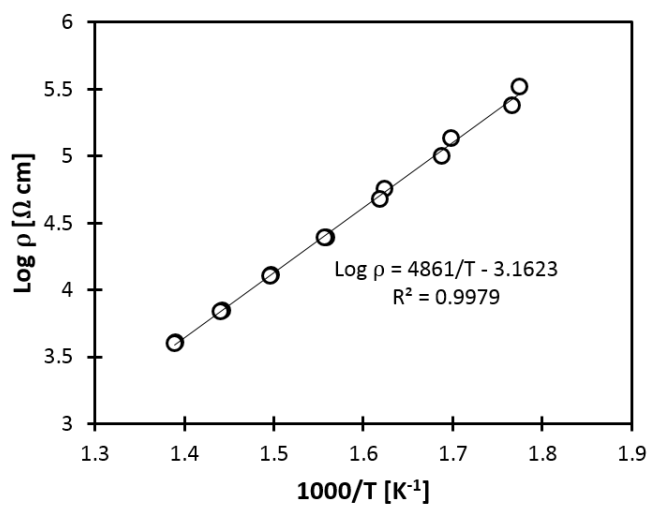
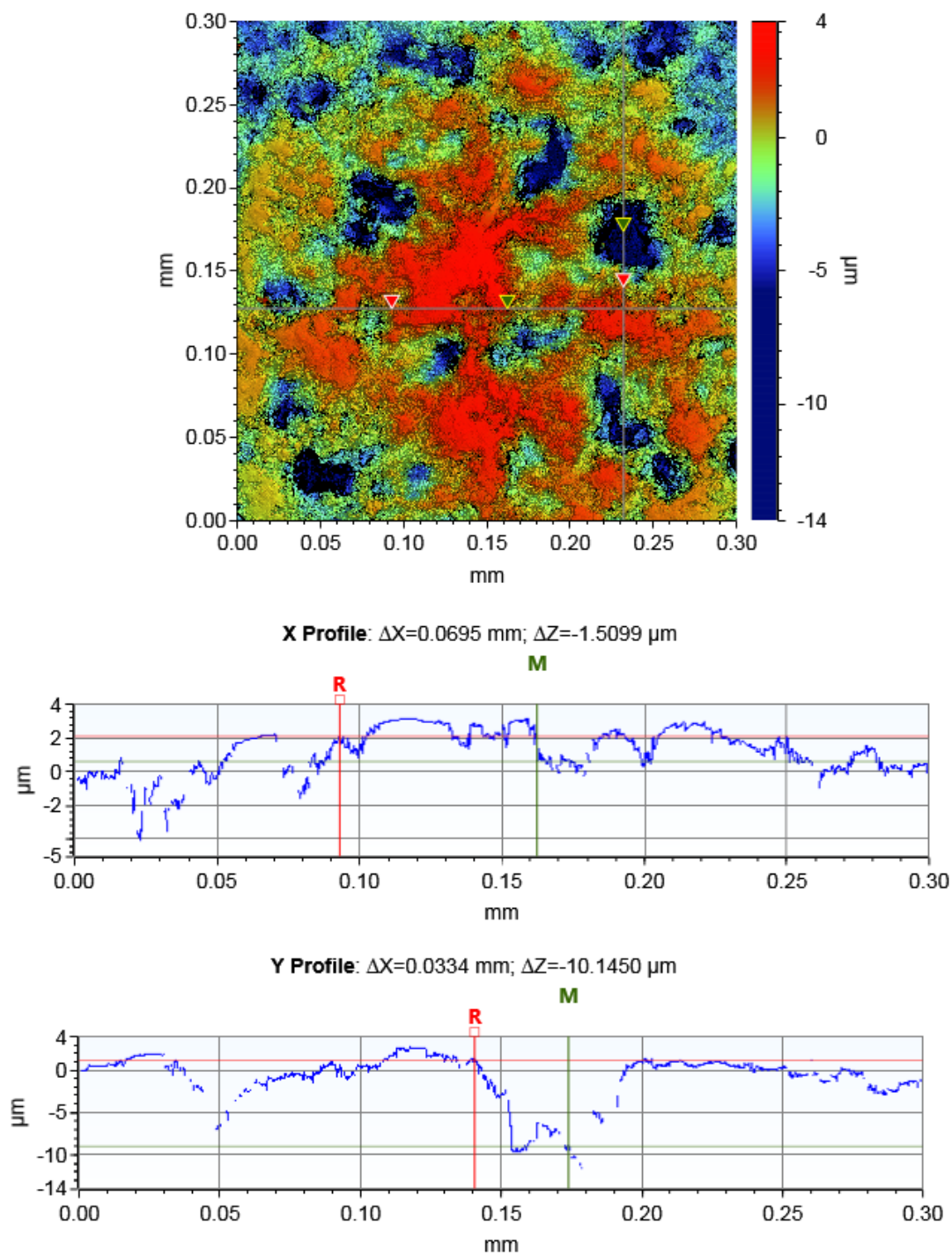


Figure 4.5: Measured resistivity of a slice taken from a YSZ probe.



4.3.1 Dependence of Polarization Resistance of Contact Size

When calculating ρ_{TPB} , a circular contact with TPB around the circumference is assumed. Since ρ_{TPB} is fixed at a constant temperature, the measured polarization resistance between a YSZ probe and an electronic conductor should vary inversely with the contact radius. If rough contact between the probe and pellet creates TPB throughout the contact area with some average area density of TPB, however, the polarization resistance should vary inversely with the square of the contact radius. Identifying the dependence of the polarization resistance on the contact radius could help identify which behavior is present in HEP measurements. Measurements of LSM and LCM pellets were performed at various contact pressures controlled by adjusting the screw on the sample holder. It should be noted that these early measurements were performed with unpolished probes made from 3 mol% YSZ. Unfortunately, as shown in Fig. 4.7 and 4.8, the variation was too large to obtain conclusive results. Part of the issue may have been the difficulty of attaining a sufficiently wide range of contact areas, as all measurements produced contact radii between 125 and 250 μm . A possible explanation for the small range of contact sizes is that changing the contact pressure changes the number and size of asperity contact points within the overall contact area (Fig. 4.3B), without changing the overall size of the contact area.

4.3.2 Effect of DC Bias

During some of the measurements investigating the relationship between contact radius and probe resistance, the polarization resistance drifted significantly over time. A concern was that repeated measurements were building up a polarization at the electrode/electrolyte interface and changing the electrochemical behavior. Measurements using no DC bias spend equal amounts of time polarizing the system in each direction, so residual polarization would

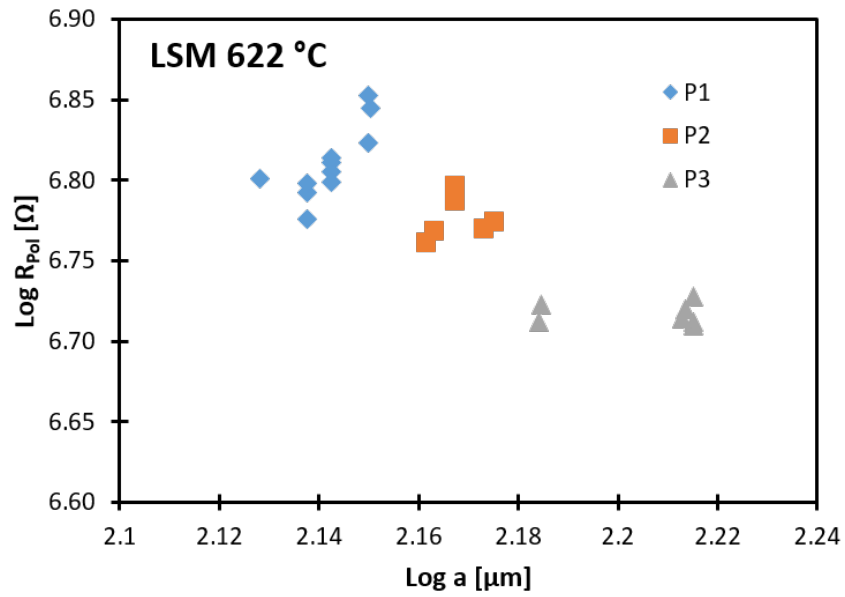


Figure 4.7: Dependence of polarization resistance on contact radius for LSM. Each data set represents measurements at the same contact pressure.

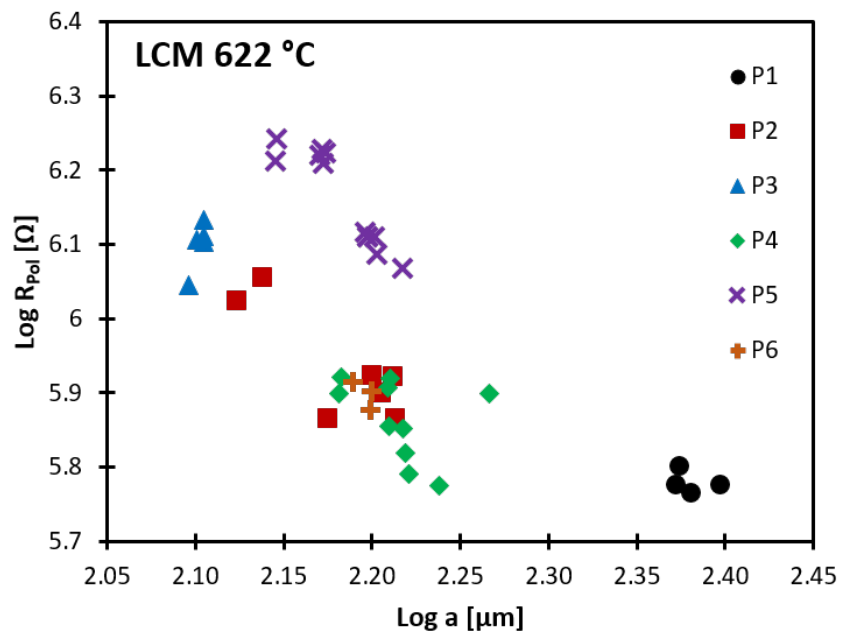


Figure 4.8: Dependence of polarization resistance on contact radius for LCM. Each data set represents measurements at the same contact pressure.

only be expected to build up if the reaction proceeds one direction faster than the other direction. If this is the case, the polarization resistance should have a significant dependence on DC biases of different signs. The effect of DC bias on the polarization resistance was investigated using measurements with an unpolished 3 mol% YSZ probe and an LSM pellet immediately following the contact radius dependence measurements in section 4.3.1. Figure 4.9 shows a possible slight trend of lower polarization resistance at negative DC biases (with the probe at a more negative potential and the electrode pellet at a more positive potential), but the more dominating trend, as shown in Fig. 4.10, is an overall decrease in the polarization resistance over time, independent of DC bias. One explanation for this behavior is the large contact pressure applied during these measurements. The contact pressure had been increased in efforts to obtain a large contact radius. Large compressive strains in the YSZ may have increased the local resistivity of the YSZ by effectively squeezing out oxygen vacancies. Forming an oxygen vacancy results in a net expansion in the material in a process known as chemical expansivity. [81] Compressive strains thus increase the formation energy of oxygen vacancies, lowering their equilibrium concentration. The local pressure in the contact between asperities can be significantly higher than what would be expected with the force evenly distributed throughout the contact area, and local thermal relaxation may have relieved some local strain over time, allowing for the oxygen vacancy concentration to return to its original value. No further experiments were performed to support or refute this explanation, but subsequent experiments maintained low contact pressure, corresponding to contact radii around 80-100 μm and did not see significant relaxation over the timescale of the measurements.

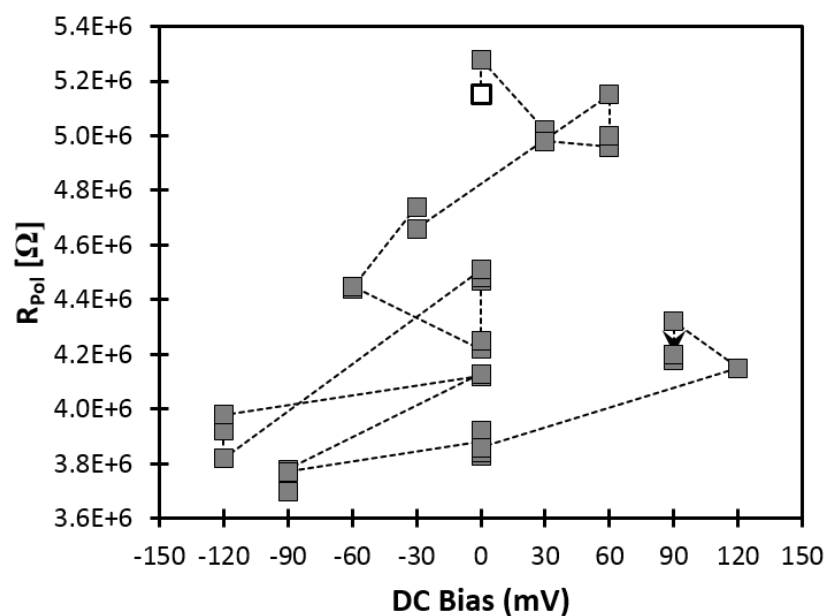
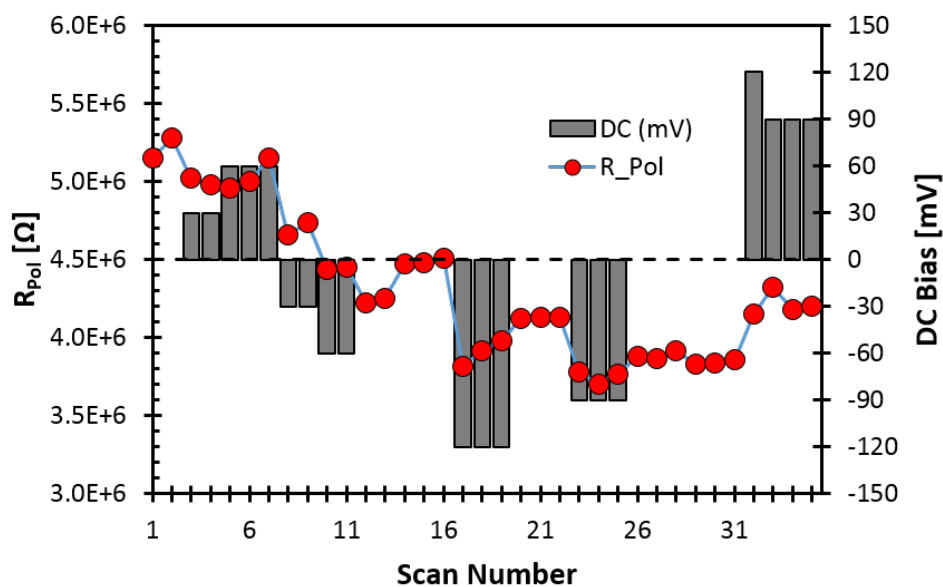


Figure 4.9: Dependence of LSM polarization resistance at 622 °C on DC bias (AC amplitude of 50 mV). The first measurement is marked with an open square, and the dashed line tracks the measurement order, which is also shown in Fig. 4.10.



4.3.3 Spreading Resistance of a Large Hemisphere

The spreading resistance in Eq. 4.1 is the solution for a circular contact on a semi-infinite plane. As long as the contact radius is sufficiently small compared to the radius of the probe, however, the hemispherical section can be approximated as a semi-infinite plane. This assumption was tested by confining a liquid electrolyte (table salt dissolved in deionized water) to a hemisphere and a large cylinder, as shown in Fig. 4.11. In each case, a steel rod just touching the surface of the water was used as the spatially-limited contact, while aluminum foil served as a bottom contact. The size of the steel rod (1.58 mm diameter) was chosen such that the ratio between the radius of the steel rod and radius of the saltwater hemisphere was similar to the ratio between the contact radius and probe radius. A thick layer of nail polish was applied to the sides of the steel rod, with only the circular end exposed to minimize contributions from the meniscus that forms around the tip of the rod. Impedance spectra of two systems were measured using the Agilent 4192A FRA. The same saltwater solution was confined to a small plastic box with aluminum foil electrodes on opposite faces, using impedance to measure the resistivity of the solution. The measured resistivity was then used in Eq. 4.1 to calculate the expected spreading resistance. The average resistance of each system is shown in Fig. 4.12, with the dashed line corresponding to the spreading resistance calculated according to Eq. 4.1. The resistance in the cylindrical geometry was slightly lower than expected, potentially owing to the formation of a meniscus around the rod, despite the nail polish coating, resulting in local current distributions that were not ideal. Nevertheless, average hemispherical resistance showed good agreement with predictions, but with a high degree of variability. Accurately positioning the rod such that the tip of the rod was just inside the wall of the hemisphere proved difficult, and the measured resistance was strongly dependent on the positioning. Despite this, the hemisphere and cylinder geometries both show similar spreading resistances to the solution of Eq. 4.1.

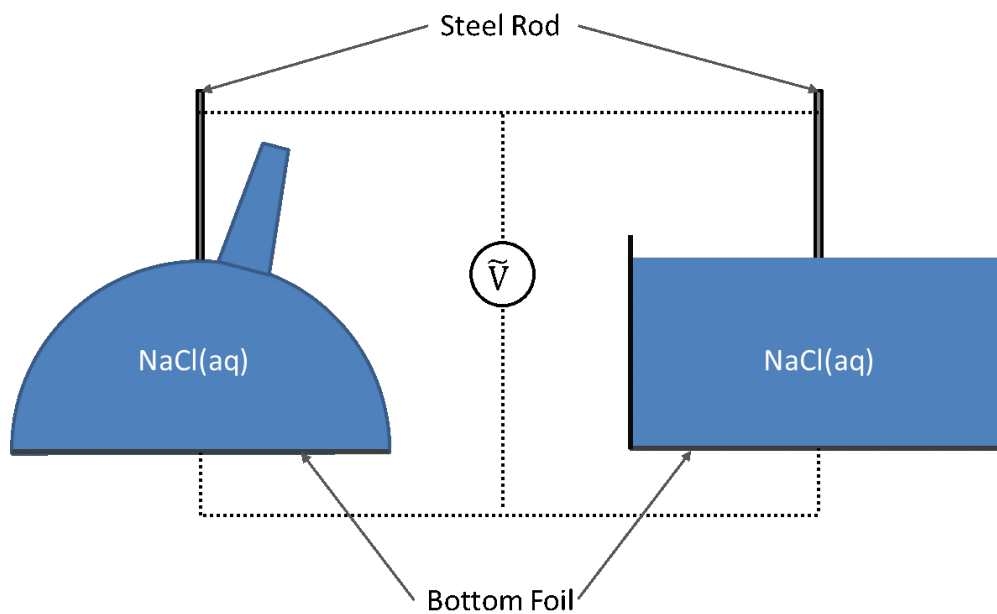


Figure 4.11: Schematic of geometry used to test the spreading resistance of a circular contact on a hemisphere and large cylinder.

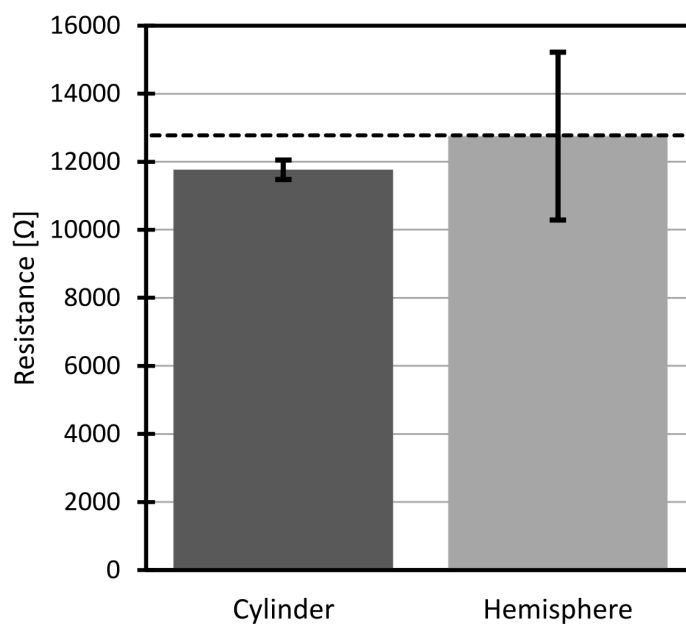


Figure 4.12: Expected spreading resistance (dashed line) and measured resistances using a saltwater electrolyte in the cylindrical and hemispherical geometries shown in Fig. 4.11

4.3.4 Effect of Polishing

Measurements of the LSM pellet were performed at 520 °C after various electrode pellet polishing stages. The linear-specific TPB resistances calculated were normalized by the literature values, and are shown in Fig. 4.13. It should be noted that the polishing particle size is not equal to the surface roughness of the pellets. Optical profilometry measurements reported surface roughness around 70-150 nm for the roughest measure (22 μm polishing particle size) and 8-15 nm for the smoothest measure (1 μm polishing particle size). The LSM measurements trended toward the literature value as the pellet surface was polished smoother. Extrapolating the trend predicts a crossover with literature around 0.1-0.2 μm polishing size. The mean free path of oxygen was estimated as a reference length scale for gas transport: [82]

$$\lambda = \frac{k_B T}{\sqrt{2} \pi d^2 p} \quad (4.8)$$

Here, λ is the mean free path of a gas molecule, k_B is Boltzmann's constant, T is temperature, d is the collision diameter (0.367 nm for oxygen), and p is the pressure (101325 Pa in ambient conditions). This predicts a mean free path around 180 nm for oxygen at 520 °C, which is larger than the surface roughness of the pellet. Therefore, for regions in contact with the asperities of the YSZ probe, collisions with the probe or pellet become increasingly important compared to collisions with other gas molecules as the pellet surface becomes smoother. This may cut off gas transport under the local contact between asperities, reducing the amount of active TPB available to participate in the reaction, and increasing the polarization resistance.

The same measurements were repeated with the LCM pellet, but showed no clear trend. However, the YSZ probe had been used in multiple previous experiments, and showed a visible dark spot on the tip after LCM measurements that may have indicated contamination from the LSM pellet and/or evidence for local polarization of the YSZ. It has been reported

that electrochemically treated and subsequently characterized interfaces between YSZ and LSM show significant cation interdiffusion under the influence of cathodic polarization. [83] Therefore, it is important to limit the polarization between the probe and pellet and to ensure clean probe surfaces before testing.

4.3.5 Mechanical Confirmation of Contact Size by Probe Resistance

Hertzian elastic contact theory (Hertz 1896) was used to check the plausibility of the contact radii calculated using the measured probe resistance. Elastic theory predicts that a sphere

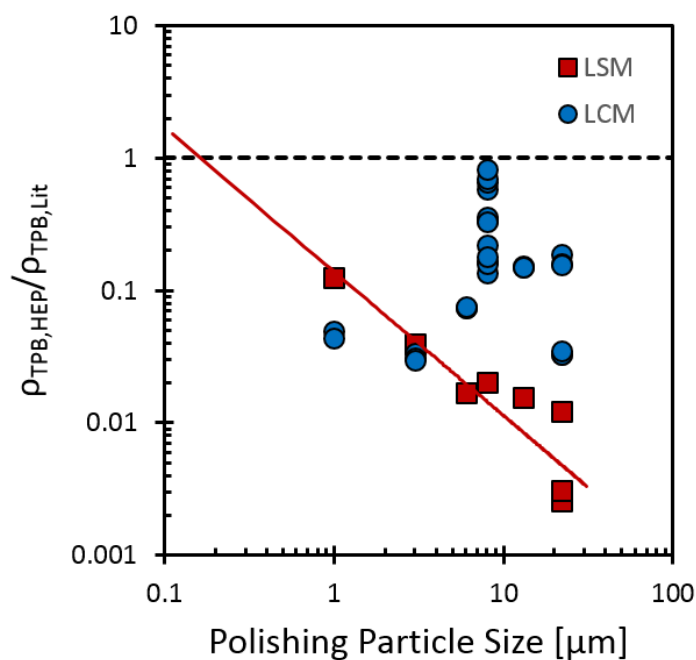


Figure 4.13: Normalized linear-specific TPB resistance for LSM and LCM at 520 C for various pellet surface polishing stages. The YSZ probe showed signs of potential contamination and/or local polarization after the LCM measurements.

pressed into a flat surface will create a circular contact with radius:

$$a = \left(\frac{3Fr}{4E^*} \right)^{\frac{1}{3}} \quad (4.9)$$

$$\text{where } \frac{1}{E^*} = \frac{1 - \nu_1^2}{E_1} + \frac{1 - \nu_2^2}{E_2} \quad (4.10)$$

The indentation depth can also be estimated using the radius of the probe and contact radius:

$$d = \frac{a^2}{r} \quad (4.11)$$

The force of contact F was calculated using Hook's Law:

$$F = -kx \quad (4.12)$$

In these equations, r is the sphere radius, ν_1 and ν_2 are the Poisson ratios of the two materials, and E_1 and E_2 are the elastic moduli of the two materials. The spring constant k of the spring in the sample holder was measured to be 3400 N/m by removing the screw, and using a load cell to measure the spring force as a function of its compression. The amount of compression in the spring x during HEP measurements was found by measuring the distance between the screw head and the metal sleeve on the sample holder when the probe was just touching the pellet, then tightening the screw and measuring the new distance and taking the difference. Measurements of the probe resistance on an LSFC pellet were used to calculate the contact area for comparison with elastic theory calculations, and are compared in Fig. 4.14, while the elastic constants used are listed in Table 4.2. The predicted contact radii are similar to those calculated from the probe resistance, especially over the 80-100 μm range (corresponding to indentation depths of 1.3-2.1 μm) where most of the finalized HEP measurements experiments resided (see Fig.).

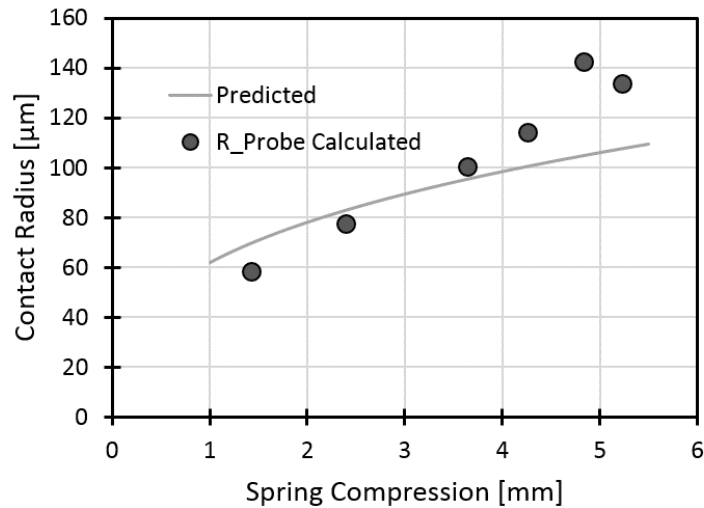


Figure 4.14: Contact radius of a YSZ probe on an LSFC pellet predicted from Hertzian elastic contact theory and calculated from the probe resistance.

Table 4.2: Elastic constants used to predict the contact area between a YSZ probe and LSFC pellet. The LSFC stiffness was estimated from data on $\text{La}_{0.8}\text{Sr}_{0.2}\text{CoO}_3$ (LSC), and the LSFC poisson's ratio was assumed to be 0.3.

| | E [GPa] | ν [] |
|------|-----------|-----------|
| YSZ | 205 [84] | 0.31 [84] |
| LSFC | 60 [85] | 0.3 |

4.4. Finalized Measurements

A finalized set of HEP measurements using the lessons learned from section 4.3 were performed using polished 8 mol% YSZ probes on LSM, LCM, LSFC, and SSC pellets. The resulting polarization resistances are shown in Fig. 4.15. For each measurement, the contact pressure was adjusted such that all of the measurements had similar probe resistances, and thus similar contact radii, as shown in Fig. 4.16. The dashed lines in Fig. 4.16 illustrate the expected resistances for contact radii of various sizes, with the slopes corresponding to the activation energy of the resistivity of the YSZ probes. Each term in Eq. 4.5 has a linear

dependence on the resistivity, so for a constant contact size, the probe resistance is expected to show the same activation energy as the YSZ resistivity. The polarization resistances show the expected ranking of materials, with the MIEC materials (LSFC, SSC) showing significantly lower polarization resistances compared to the electronic conductors (LSM, LCM). Literature values have shown lower resistances for LCM [54] compared to LSM [53] and for SSC compared to LSFC. [28] The resistances were normalized using Eq. 4.6 and 4.7.

4.4.1 Triple Phase Boundary Linear-Specific Resistance

The linear-specific TPB resistances of LSM and LCM calculated using Eq. 4.6 are plotted in Fig. 4.17 along with literature values from patterned electrode studies. Multiple sequential scans were recorded and independently fit at each temperature, and the variability between scans was smaller than the symbols, except for the lowest temperature LSM measurement, where the high impedance introduced more variability. For this point, the variability in $\log \rho_{TPB}$ was ± 0.15 . For both materials, the activation energies from HEP measurements are within about 0.1 eV of those obtained from the literature using patterned electrodes (see Table 4.1 for a list of activation energies). However, HEP measurements for both materials underestimate ρ_{TPB} by a factor of about 3 compared to literature values. This discrepancy could arise from an underestimation of the total TPB length arising from the roughness of the probe surface.

4.4.2 Mixed Conductor Area-Specific Resistance

The polarization resistances for LSFC and SSC were normalized to an area-specific surface resistance according to Eq. 4.7, and are compared against literature values from patterned thin film studies in Fig. 4.18. The reaction pathways for the two measurement techniques are somewhat different. In patterned thin film electrode measurements, oxygen is incorpo-

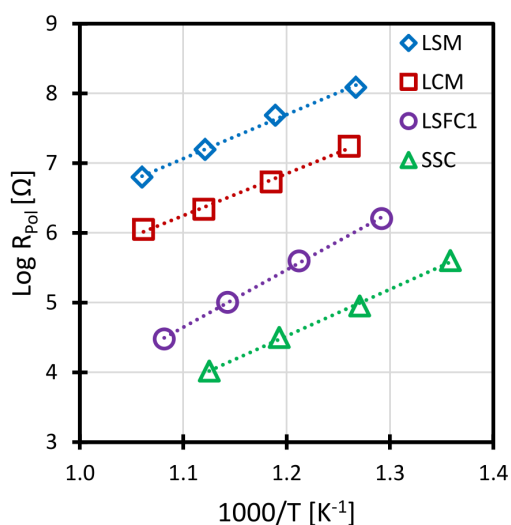


Figure 4.15: Measured polarization resistances from finalized HEP measurements. The results show the expected ranking of performance, with the MIEC materials showing significantly lower resistances compared to the electronic conductors.

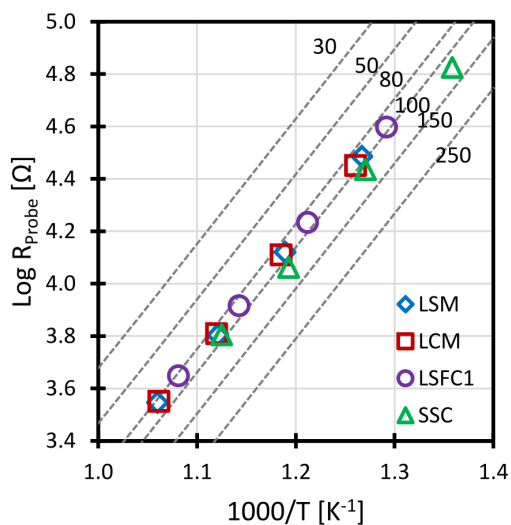


Figure 4.16: Measured probe resistances for finalized HEP measurements. The dashed lines show values corresponding to various contact radii, with values listed in μm . The slope of the dashed lines corresponds to the resistivity of the YSZ probes. There is good agreement, in terms of the activation energy of the resistivity of YSZ and also of the probe radii, with only two or three outliers not falling in the 80-100 μm range

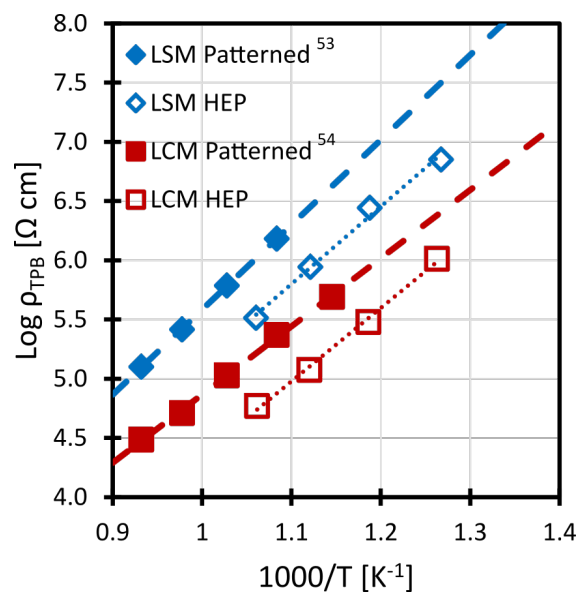


Figure 4.17: Temperature dependence of the linear-specific TPB resistance for LSM and LCM. Closed symbols show the results of patterned electrode studies from the literature, while open symbols show the results from HEP measurements in this work.

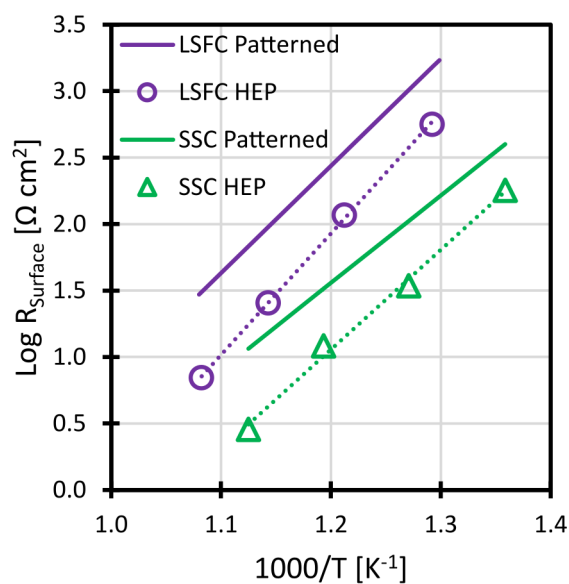


Figure 4.18: Area-specific surface resistance of LSFC and SSC from HEP measurements in this work compared with patterned electrode measurements from literature. [28]

rated on one side of the electrode, then diffuses through the electrode before transferring to the electrolyte. In HEP measurements, oxygen exchange occurs on the same side as the electrolyte, with lateral diffusion through the electrode and transferring to the electrolyte. However, both pathways involve surface exchange and oxygen diffusion over a short distance, so the behavior should be fairly similar. As with the ρ_{TPB} measurements, the HEP results underestimate the magnitude of the surface resistance by a factor of about 3 compared to literature values. The activation energies were also approximately 0.2 eV larger than the literature values, as shown in Table 4.1. The ionic conductivity of the MIEC materials should allow for the reaction area to extend beyond the contact perimeter by a distance that depends on the balance of oxygen surface exchange and oxygen ion diffusion. A rough approximation can be found using a characteristic length $L_C = D^*/k^*$, where D^* is the oxygen tracer diffusivity, and k^* is the corresponding surface exchange coefficient. [79] For both LSFC and SSC, L_C is on the order of 100 μm . [79, 86] Adding the area within 100 μm of the contact perimeter for a contact radius of 100 μm would increase the total area by a factor of 4. Therefore, the extension of the reaction area beyond the contact perimeter may explain the underestimation of R_S observed in HEP measurements.

Measurements on LSFC were repeated using a larger contact radius of about 150 μm (LSFC2) and using a different YSZ probe (LSFC3) in order to test the reproducibility of the surface resistance measurements. The probe and polarization resistances from these measurements are shown in Fig. 4.19A while the calculated area-specific surface resistance is shown in Fig. 4.19B. The polarization resistance decreased significantly with increasing contact radius, but the calculated surface resistances showed little variation between experiments, indicating good reproducibility.

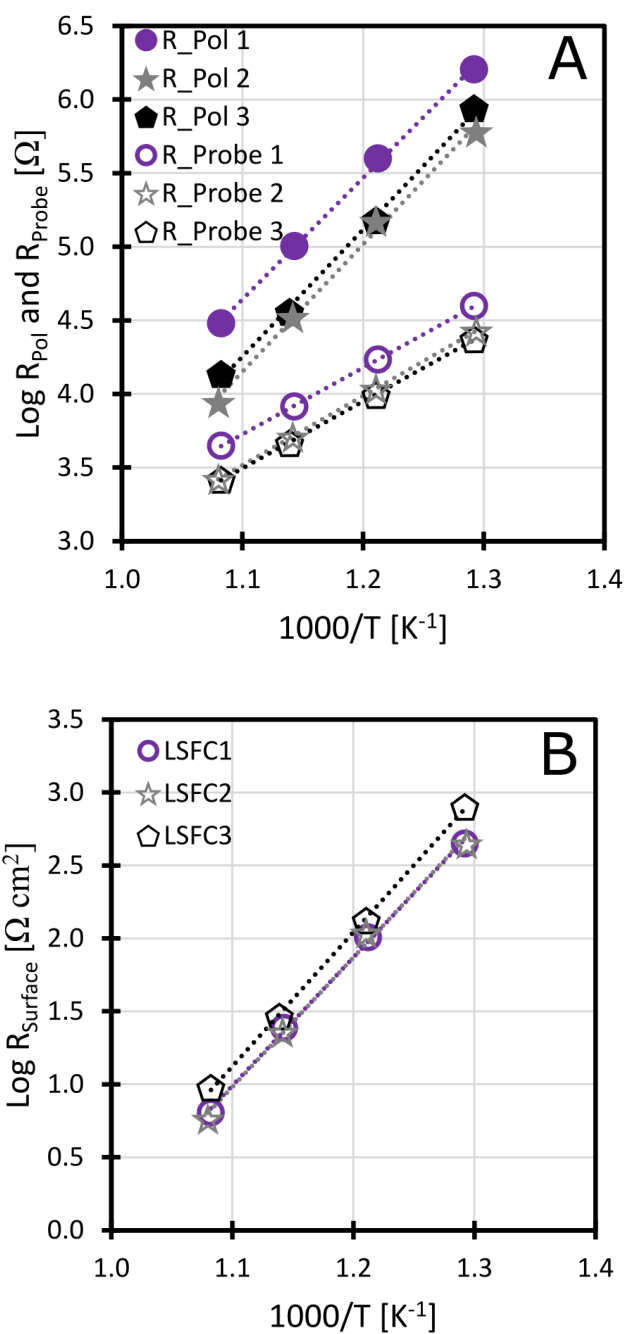


Figure 4.19: Probe and polarization resistances (A) and normalized area-specific surface resistances (B) for LSFC measurements used to investigate reproducibility. LSFC1 and LSFC2 used the same YSZ probe with different contact radii (100 μm and 150 μm respectively), while LSFC used a different probe with a contact radius around 150 μm .

4.5. Conclusions

In all the cases shown above, the normalized resistances were lower than literature values by about a factor of 3. It is unlikely that the measurement of the polarization resistance would introduce an error that large. The more likely source of the discrepancy is the geometric factors in the form of an underestimation of the total TPB length for ρ_{TPB} or active reaction area for R_S . The analysis of electronic conductors assumes that TPB exists only along the perimeter of the electrolyte-electrode contact, but the roughness of the probe surface (Fig. 4.6) could allow for gas flow underneath the overall contact area, creating additional active TPB throughout the contact area. The low surface resistance results for MIEC materials suggests that there is sufficient gas transport underneath the contact and oxygen ion conductivity in the MIEC materials to allow the entire contact area to actively contribute to the electrode reaction. They also suggest that a significant amount of area beyond the contact area is contributing to the reaction. Indeed, it is expected for MIEC electrodes that the active area extends beyond the contact perimeter by a distance that is dependent on the oxygen diffusion coefficient, similar to the utilization length sometimes discussed in porous MIEC electrode studies. [23] Given that utilization lengths are typically on the order of a few microns, the associated extension of the active area is insufficient to explain the apparent factor of 3 enhancement. Given the difference in geometric factors between the ρ_{TPB} and R_S analysis, it is unclear whether the same factor of 3 discrepancy in each analysis arises from a common physical explanation, or is simply coincidence.

Regardless, the results suggest that for both linear-specific TPB resistance measurements and area-specific surface polarization resistance measurements, an experimental correction factor derived from measurements using a known material could be used to calibrate future HEP measurements to obtain more accurate values. Even without calibration, the HEP results provide reasonably accurate measurements of activation energies and a reliable rank-

ing of electrode performance. For example, if a set of materials with unknown properties is measured using a consistent contact size between measurements, a direct comparison of the polarization resistances will provide a ranking of the overall electrochemical performance of the materials. This procedure could be used to quickly identify potential new cathode materials (or anode materials if the measurements could be performed in fuel atmospheres) before moving to other characterization techniques for a more in-depth analysis of the top candidates. Finally, although YSZ was the only electrolyte material used in this work, it should be possible to fabricate probes made from other electrolyte materials, or to coat the YSZ probes with a layer of other electrolyte materials to investigate more electrolyte/electrode pairings.

CHAPTER 5

Phase Compatibility in the $\text{LaO}_{1.5}\text{-GaO}_{1.5}\text{-NiO}$ System

As discussed in section 2.5, the $\text{LaO}_{1.5}\text{-GaO}_{1.5}\text{-NiO}$ system contains several phases of interest for SOFCs using LSGM electrolytes. This work sought to refine the phase compatibility relationships and solubility limits by mapping out an isothermal section of the quasi-ternary diagram at 1400 °C. The study temperature of 1400 °C was chosen to enhance reaction kinetics in order to reach equilibrium. In addition to being necessary when mapping phase diagrams, reaching equilibrium provides insight into the long-term stability of devices and the potential for the formation of interfacial phases that can be difficult to detect. [87] The study temperature also has important ramifications for device processing, as the anode and electrolyte layers are often co-fired at temperatures between 1400 and 1470 °C. [19, 88–90] Finally, the fact that the binary systems show little difference at lower temperatures suggests that the behavior at 1400 °C can be informative of behavior at lower operating temperatures.

Samples were prepared using solid state synthesis methods (section 3.1) with a final firing step of 72 hours at 1400 °C, followed by air quenching in order to preserve the phase behavior at 1400 °C. The XRD methods described in section 3.2 were used to identify the

phases present as well as the lattice parameters and relative weight fractions of those phases. A few samples were subjected to a second firing for 72 hours at 1400 °C, but showed no significant change beyond the initial 72 hours. A table of all samples used in this study is listed in Appendix B.

5.1. Solubility Limit Determination

Initial work sought to determine solubility limits using Vegard’s Law as described in section 3.3.2. For the phases studied, however, the lattice parameter changes could not be reliably resolved, owing to the small changes in lattice parameter vs. composition, whether in single phase lines or multi-phase compatibility triangles. One explanation is the similar ionic radii of gallium and nickel (see Table 2.1). The large orthorhombic structures of the Ruddlesden-Popper phases and the potential for a variable $\text{Ni}^{2+}/\text{Ni}^{3+}$ ratio may have further frustrated Vegard’s Law efforts. Instead, this work heavily employed conventional phase analysis (section 3.3.1) and the disappearing phase method (section 3.3.3). The sample compositions used in this study are shown in Fig. 5.1. Two samples in the gallium-rich corner marked as stars showed melting behavior, likely related to the eutectic between LaGaO_3 and $\text{GaO}_{1.5}$ at 1323 °C mentioned in section 2.5.1. As a result, the gallium-rich corner is shown as a cross-hatched region in Fig. 5.1 and subsequent figures. The solubility limits of the Ruddlesden-Popper series $\text{La}_{n+1}\text{Ni}_n\text{O}_{3n+1}$ as well as LaGaO_3 were determined using conventional phase analysis.

All phases appear as lines of constant lanthanum content, with solid solubility corresponding to substitutions between nickel and gallium. The previous diagram from CALPHAD calculations predicted an increase in lanthanum content in La_2NiO_4 with increasing gallium content, but no samples along the line between La_2NiO_4 and $\text{La}_4\text{Ga}_2\text{O}_9$ showed evidence of a third phase which would be expected in the case of varying lanthanum content.

As discussed in Chapter 2, gallium and nickel have similar ionic radii, while lanthanum is significantly larger, making substitutions involving lanthanum unlikely. The single-phase and multi-phase compositions closest to each solubility limit are listed in Table 5.1. No solubility of nickel in $\text{La}_4\text{Ga}_2\text{O}_9$ has been previously reported, and a sample with the composition $\text{La}_4(\text{Ga}_{0.95}\text{Ni}_{0.05})_2\text{O}_9$ showed evidence of La_2NiO_4 , indicating negligible solubility. The $n=2$ phase $\text{La}_3\text{Ni}_2\text{O}_7$ is not stable at the study temperature of 1400 °C, and was previously unreported in the ternary system, but samples below the lower stability limit of gallium in $\text{La}_4(\text{Ni,Ga})_3\text{O}_{10}$ showed evidence of $\text{La}_3\text{Ni}_2\text{O}_7$. Subsequently, single-phase samples of $\text{La}_3(\text{Ni,Ga})_2\text{O}_7$ were synthesized. The stabilization of $\text{La}_3\text{Ni}_2\text{O}_7$ at higher temperatures through the addition of gallium mirrors the observation of stabilized $\text{La}_4(\text{Ni,Ga})_3\text{O}_{10}$ by Solak et al., and may be expected given that the two phases have closely related structures.

Table 5.1: Solubility limits determined using conventional phase analysis and disappearing phase methods, including standard errors based on uncertainties in the linear regression. Phase analysis results list the single-phase and multi-phase samples closest to the solubility limits.

| Solid Solution | Boundary | Phase Analysis | | Disappearing Phase |
|--|----------|----------------|-------------|--------------------|
| | | Single-Phase | Multi-Phase | |
| $\text{La}_2\text{Ni}_{1-x}\text{Ga}_x\text{O}_4$ | Low | 0 | 0 | - |
| | High | 0.10 | 0.15 | 0.094 ± 0.013 |
| $\text{La}_3(\text{Ni}_{1-x}\text{Ga}_x)_2\text{O}_7$ | Low | 0.25 | 0.20 | - |
| | High | 0.275 | 0.30 | 0.265 ± 0.008 |
| $\text{La}_4(\text{Ni}_{1-x}\text{Ga}_x)_3\text{O}_{10}$ | Low | 0.30 | 0.25 | - |
| | High | 0.55 | 0.575 | 0.565 ± 0.018 |
| $\text{LaGa}_{1-x}\text{Ni}_x\text{O}_3$ | Low | 0 | 0 | - |
| | High | 0.50 | 0.55 | 0.492 ± 0.012 |

The upper limits of gallium in the Ruddlesdon-Popper phases and the upper limit of nickel in LaGaO_3 were also determined using the disappearing phase method, as shown in Fig. 5.2-5.5. The resulting limits are listed in Table 5.1 along with the results of conventional

phase analysis, and are shown in Fig. 5.6. The lower solubility limits of $\text{La}_3(\text{Ni,Ga})_2\text{O}_9$ and $\text{La}_4(\text{Ni,Ga})_3\text{O}_{10}$ were taken to be halfway between the single-phase and multi-phase samples from conventional phase analysis. In most cases, the solubility limit determined by the disappearing phase method is slightly lower than the last observed single-phase composition. This is not surprising, as the amount of secondary phase just beyond the solubility limit should be small, and may be below the detection limits of XRD. Nevertheless, conventional

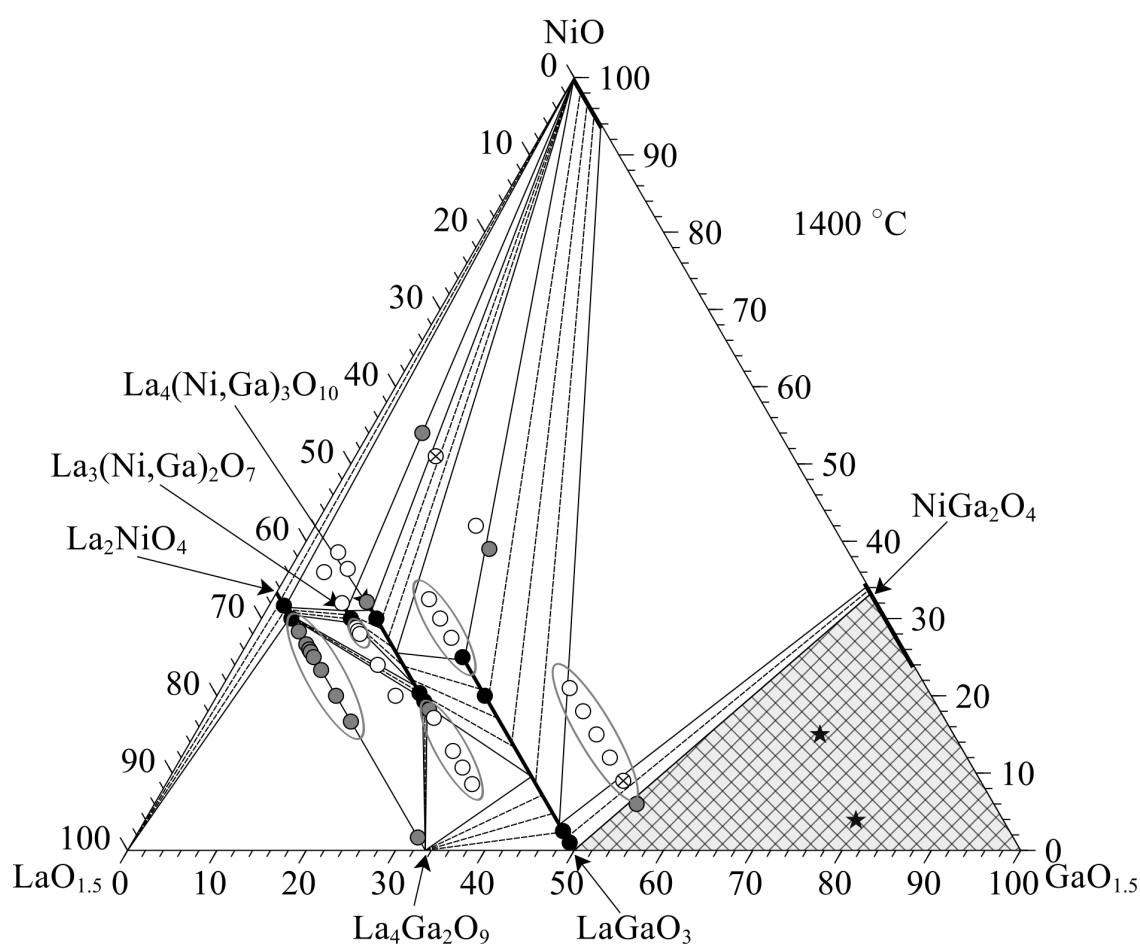


Figure 5.1: Sample compositions used in this study. Open circles were triphasic, shaded circles were biphasic, and black circles were monophasic. The two stars mark the compositions where melting behavior was observed. The circled lines of samples correspond to those used in Fig. 5.2-5.5 and 5.8. Circles with X's denote the two samples where trace amounts of a third phase were observed in a region expected to be biphasic.

phase analysis and the disappearing phase method yield consistent results, with solubility limits trending toward the last observed single-phase composition rather than the first multi-phase composition.

5.2. Compatibility Involving LaGaO_3

The disappearing phase method was also used to determine the details of phase relationships involving LaGaO_3 , as they are the most relevant for SOFCs using LSGM electrolytes. The results are shown in Fig. 5.7. The details of the phase relationships are defined by the positions of the vertices of the three triphasic regions labeled A, B, and C in Fig. 5.7. In each region, two vertices are known from literature or the solubility limit measurements from section 5.1. Region A has known vertices at the gallium-rich end of NiO and the nickel-rich end of NiGa_2O_4 . Region B has known vertices at $\text{La}_4\text{Ga}_2\text{O}_9$ and the gallium-rich end of $\text{La}_4(\text{Ni,Ga})_3\text{O}_{10}$. Region C has a known vertex at the nickel-rich end of LaGaO_3 and another assumed to reside at pure NiO with no significant gallium content. This assumption is strengthened by the observation of a sample with the overall composition $\text{La}_{0.4}(\text{Ga}_{0.35}\text{Ni}_{0.65})_{0.6}\text{O}_\delta$ in the NiO- LaGaO_3 biphasic region. If the NiO vertex of region C contained a significant amount of gallium, this sample would be expected to reside inside region C and would contain $\text{La}_4(\text{Ni,Ga})_3\text{O}_{10}$.

The position of the third vertex in each region was determined by using the disappearing phase method to find the boundary between the triphasic and a biphasic region, then extrapolating from a known vertex through the measured boundary to the point where it intersects the phase line of the third vertex, as explained in section 3.3.3. Samples along the line corresponding to 40 mol% $\text{LaO}_{1.5}$ were used to determine the LaGaO_3 vertex in region A. This line is parallel to the NiO- NiGa_2O_4 side of the triphasic region, so the amount of LaGaO_3 in each sample was essentially constant, around 80 wt%. Rigorously, the mole

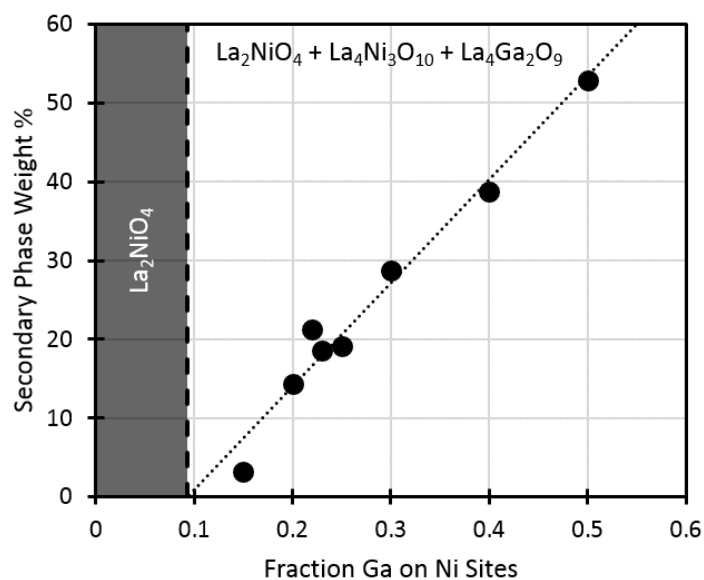


Figure 5.2: Disappearing phase method along the La_2NiO_4 line. Extrapolating to the point where secondary phases disappear yields the maximum solubility of gallium in La_2NiO_4 .

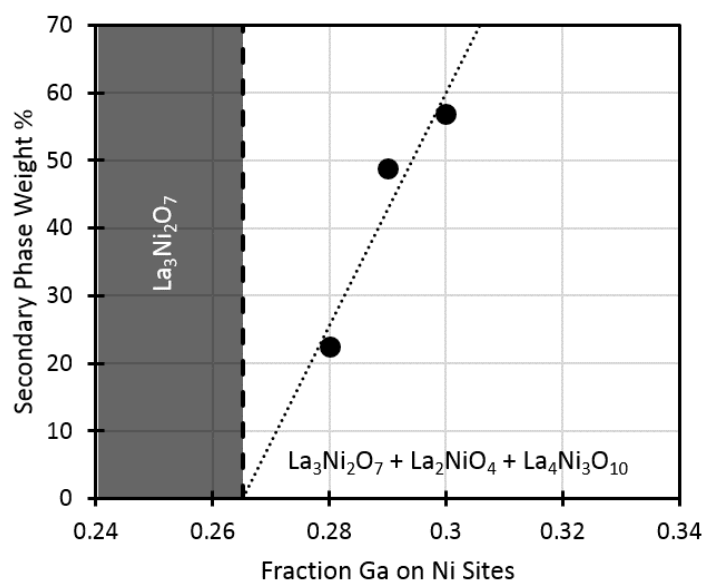


Figure 5.3: Disappearing phase method along the $\text{La}_3\text{Ni}_2\text{O}_7$ line. Extrapolating to the point where secondary phases disappear yields the maximum solubility of gallium in $\text{La}_3\text{Ni}_2\text{O}_7$.

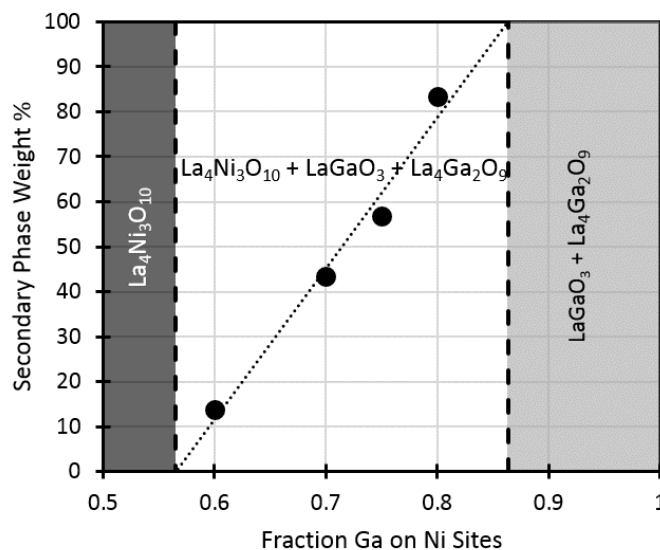


Figure 5.4: Disappearing phase method along the $\text{La}_4\text{Ni}_3\text{O}_{10}$ line. Extrapolating to the point where secondary phases disappear yields the maximum solubility of gallium in $\text{La}_4\text{Ni}_3\text{O}_{10}$. Extrapolating from $\text{La}_4\text{Ga}_2\text{O}_9$ through the point where $\text{La}_4\text{Ni}_3\text{O}_{10}$ disappears yields the LaGaO_3 vertex of region B in Fig. 5.7.

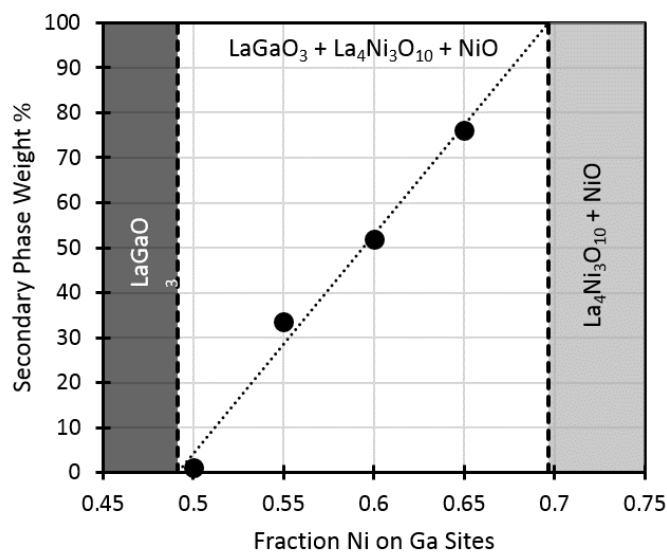


Figure 5.5: Disappearing phase method along the LaGaO_3 line. Extrapolating to the point where secondary phases disappear yields the maximum solubility of nickel in LaGaO_3 . Extrapolating from NiO through the point where LaGaO_3 disappears yields the $\text{La}_4\text{Ni}_3\text{O}_{10}$ vertex of region C in Fig. 5.7.

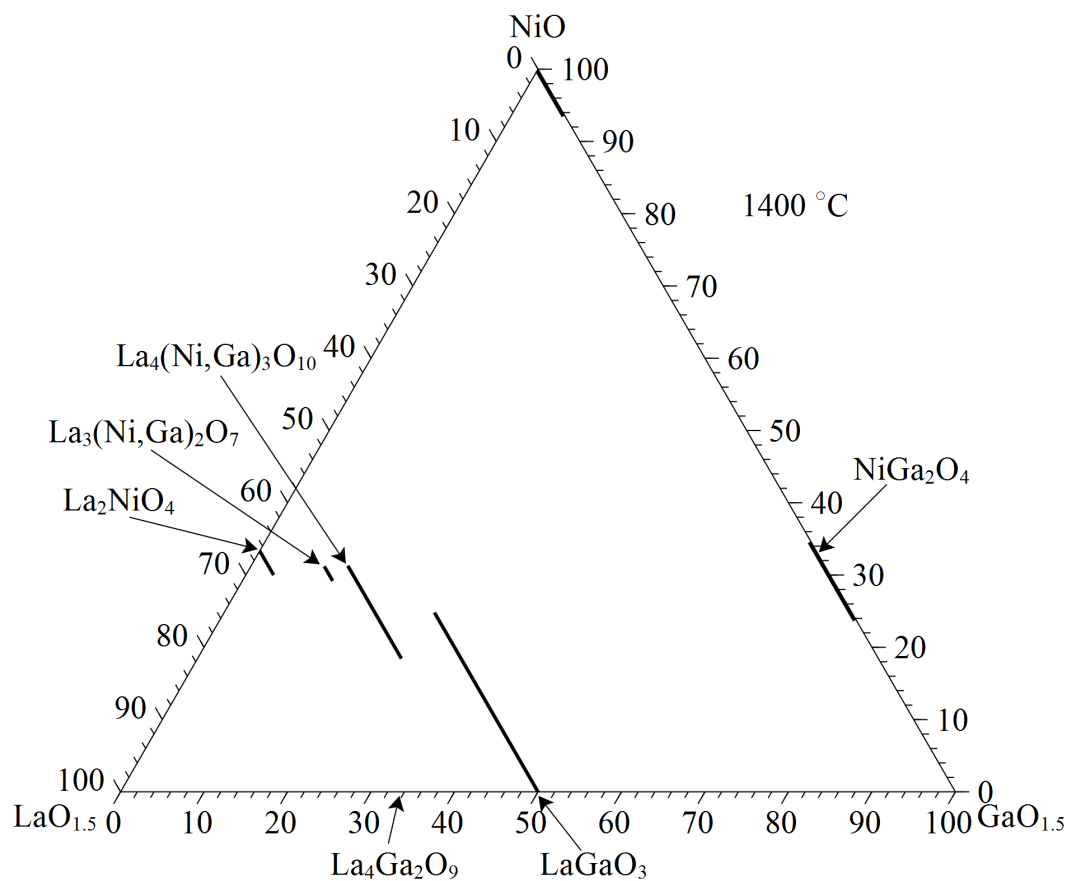


Figure 5.6: Ternary diagram showing measured solubility limits (listed in Table 5.1) corresponding to substitution between gallium and nickel. Solubility limits along the NiO-GaO_{1.5} binary from Zinkevich et al. [63]

fraction of LaGaO₃ should be constant, but the weight fraction would change depending on the relative molar mass of NiO and Ni_{0.33}Ga_{0.67}O_{1.33} (NiGa₂O₄ on a per-cation basis). The fact that the samples were mostly LaGaO₃ and the molar masses are fairly similar (74.7 g/mol for NiO, 87.4 g/mol for Ni_{0.33}Ga_{0.67}O_{1.33}), the weight fraction of LaGaO₃ was fairly constant. As such, the relative weight fractions of NiO and NiGa₂O₄ (normalized to the combined amount of NiO and NiGa₂O₄) were used for the disappearing phase method in region A, as shown in Fig. 5.8. In this case, two boundaries were able to be measured, and

extrapolating from the two known vertices through the measured boundaries yielded two points on the LaGaO_3 line within error of each other. In region B, samples along the line of $\text{La}_4(\text{Ni,Ga})_3\text{O}_{10}$ were used to find the border between region B and the $\text{La}_4\text{Ga}_2\text{O}_9$ - LaGaO_3 region (Fig. 5.4). Extrapolating from the vertex at $\text{La}_4\text{Ga}_2\text{O}_9$ through the measured border to a point on the LaGaO_3 line yielded the position of the third vertex in region B. Similarly, samples along the line of $\text{La}(\text{Ga,Ni})\text{O}_3$ in region C were used to find the border between

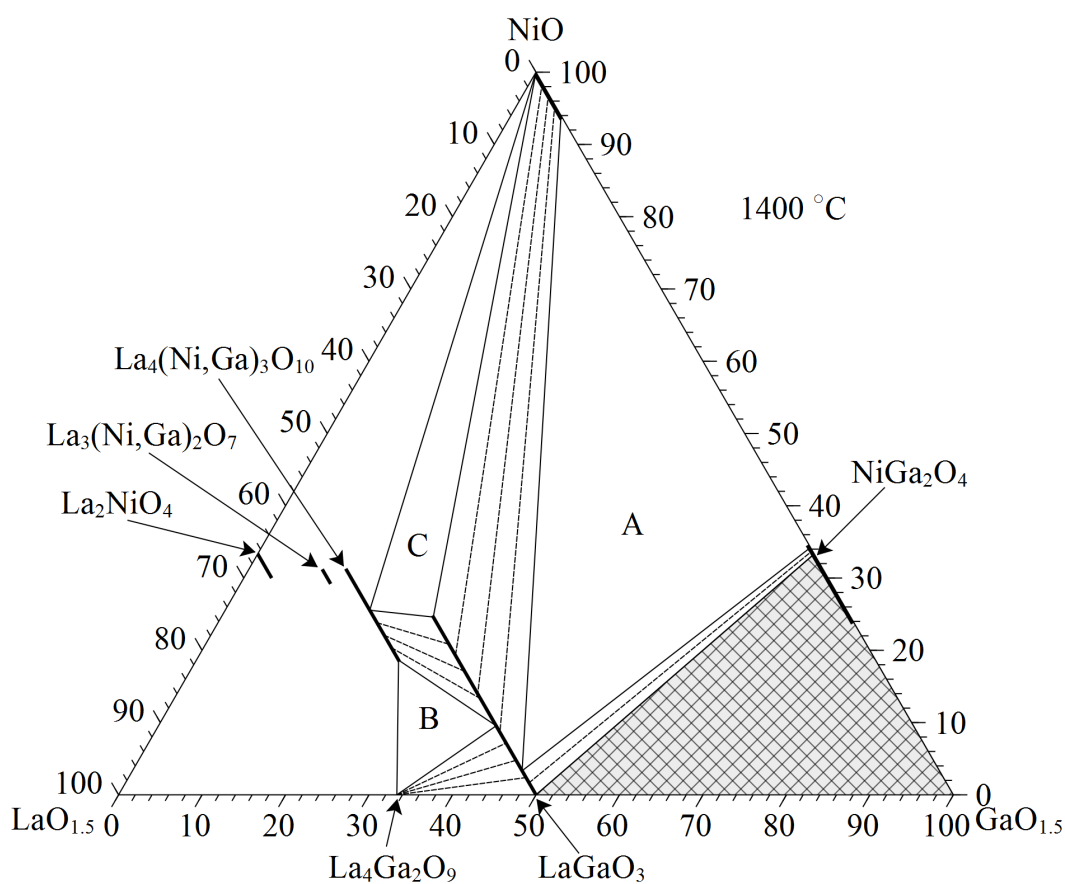


Figure 5.7: Ternary diagram showing phase relationships involving LaGaO_3 as determined using the disappearing phase method. The phase relationships are governed by the vertices of the triphasic regions labeled A, B, and C. The gallium-rich corner is shaded to indicate the presence of melting behavior.

region C and the NiO- $\text{La}_4(\text{Ni,Ga})_3\text{O}_{10}$ biphasic region (Fig. 5.5). Extrapolating from NiO through that border yielded the $\text{La}_4(\text{Ni,Ga})_3\text{O}_{10}$ vertex of region C. The resulting positions of all of the vertices are listed in Table 5.2.

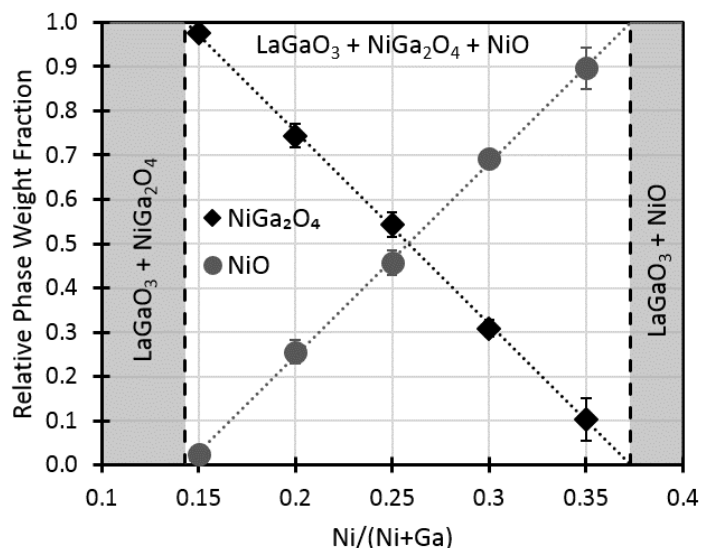


Figure 5.8: Disappearing phase method in region A along a line corresponding to 40 mol% $\text{LaO}_{1.5}$. The LaGaO_3 content was fairly constant (around 80 wt%), so relative weight fractions were plotted. Extrapolating to the point where each phase disappears yields the boundary between triphasic region (white) and the bounding biphasic regions (shaded). Extrapolating from the other vertices of region A in Fig. 5.7 through those boundaries yields the LaGaO_3 vertex.

5.2.1 Electrical Conductivity of $\text{La}_4(\text{Ni,Ga})_3\text{O}_{10}$

Figure 5.7 shows that $\text{La}_4(\text{Ni,Ga})_3\text{O}_{10}$ is the only Ruddlesden-Popper phase that exhibits thermodynamic equilibrium with LaGaO_3 . However, the equilibrium requires a high gallium content in $\text{La}_4(\text{Ni,Ga})_3\text{O}_{10}$. In order to investigate the effect of this high gallium content on the electrical properties of $\text{La}_4(\text{Ni,Ga})_3\text{O}_{10}$, the conductivities of single phase pellet samples with varying gallium content were measured using a four-point probe method described in section 3.4.1. The corrected conductivities are shown in Fig. 5.9. As the gallium content

increases, the conductivity is drastically reduced. At the gallium-rich end, the conductivity is four orders of magnitude lower than $\text{La}_4\text{Ni}_3\text{O}_{10}$ with no gallium content. The measurements were carried out at room temperature, so the measured conductivity is likely entirely electronic conductivity, which is critical for the performance of a cathode material.

5.3. Approximate Representation of the Full Phase Diagram

Figure 5.10 shows an approximate representation of the full $\text{LaO}_{1.5}\text{-GaO}_{1.5}\text{-NiO}$ quasi-ternary phase diagram. As in other diagrams, the cross-hatched region in the gallium-rich corner indicates where melting behavior was observed. This diagram is fully consistent with the conventional phase analysis observations at every composition in Fig. 5.1 with the exception of the two compositions marked with X's where trace amounts of a third phase were observed in a region expected to be biphasic. Trace amounts of $\text{La}_3\text{Ni}_2\text{O}_7$ were detected in the sample with the composition $\text{La}_{0.4}(\text{Ni}_{0.85}\text{Ga}_{0.15})_{0.6}\text{O}_\delta$, and trace amounts of NiO were detected in

Table 5.2: Vertex compositions for regions A, B, and C.

| Region | Vertex Phase | x | Source |
|--------|--|-------------------|-----------------------|
| A | $\text{Ni}_{1-x}\text{Ga}_x\text{O}$ | 0.06 | Zinkevich et al. [63] |
| | $\text{Ni}_{1+x}\text{Ga}_{2-x}\text{O}_4$ | 0.027 | Zinkevich et al. [63] |
| | $\text{LaGa}_{1-x}\text{Ni}_x\text{O}_3$ | 0.044 ± 0.061 | This work (5.2) |
| | | 0.089 ± 0.073 | This work (5.2) |
| B | $\text{La}_4\text{Ga}_2\text{O}_9$ | N/A | N/A |
| | $\text{La}_4(\text{Ni}_{1-x}\text{Ga}_x)_3\text{O}_{10}$ | 0.565 ± 0.056 | This work (5.1) |
| | $\text{LaGa}_{1-x}\text{Ni}_x\text{O}_3$ | 0.191 ± 0.100 | This work (5.2) |
| C | $\text{Ni}_{1-x}\text{Ga}_x\text{O}$ | 0 | Assumed |
| | $\text{LaGa}_{1-x}\text{Ni}_x\text{O}_3$ | 0.492 ± 0.036 | This work (5.1) |
| | $\text{La}_4(\text{Ni}_{1-x}\text{Ga}_x)_3\text{O}_{10}$ | 0.404 ± 0.055 | This work (5.2) |

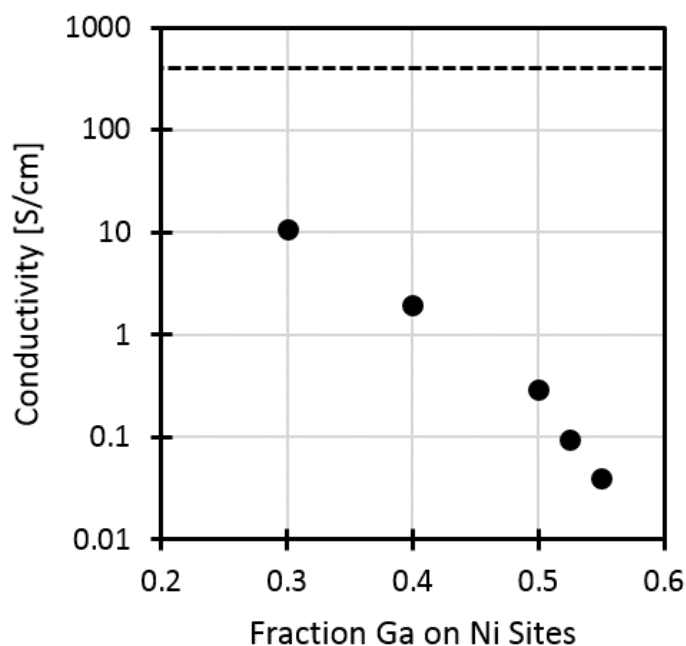


Figure 5.9: Room temperature four-point probe conductivity of $\text{La}_4(\text{Ni,Ga})_3\text{O}_{10}$ as a function of gallium content, corrected for porosity. The dashed line corresponds to the room temperature conductivity of pure $\text{La}_4\text{Ni}_3\text{O}_{10}$. [30]

the sample with the composition $\text{La}_{0.4}(\text{Ni}_{0.15}\text{Ga}_{0.85})_{0.6}\text{O}_\delta$. As previously reported by Solak et al., [67] equilibrium between La_2NiO_4 and LaGaO_3 is broken by the formation of $\text{La}_4\text{Ga}_2\text{O}_9$ and $\text{La}_4\text{Ni}_3\text{O}_{10}$. While La_2NiO_4 is the only binary oxide in the $\text{LaO}_{1.5}$ -NiO system that is stable at the study temperature of 1400 °C, both $\text{La}_3\text{Ni}_2\text{O}_7$ and $\text{La}_4\text{Ni}_3\text{O}_{10}$ were observed to be stabilized by the substitution of gallium for nickel. While $\text{La}_3\text{Ni}_2\text{O}_7$ is stable only over a narrow range, $\text{La}_4\text{Ni}_3\text{O}_{10}$ shows stability over a wide range of compositions. LaNiO_3 is the only phase along the $\text{LaO}_{1.5}$ -NiO binary that was not observed to be stabilized at this temperature by the substitution of gallium for nickel.

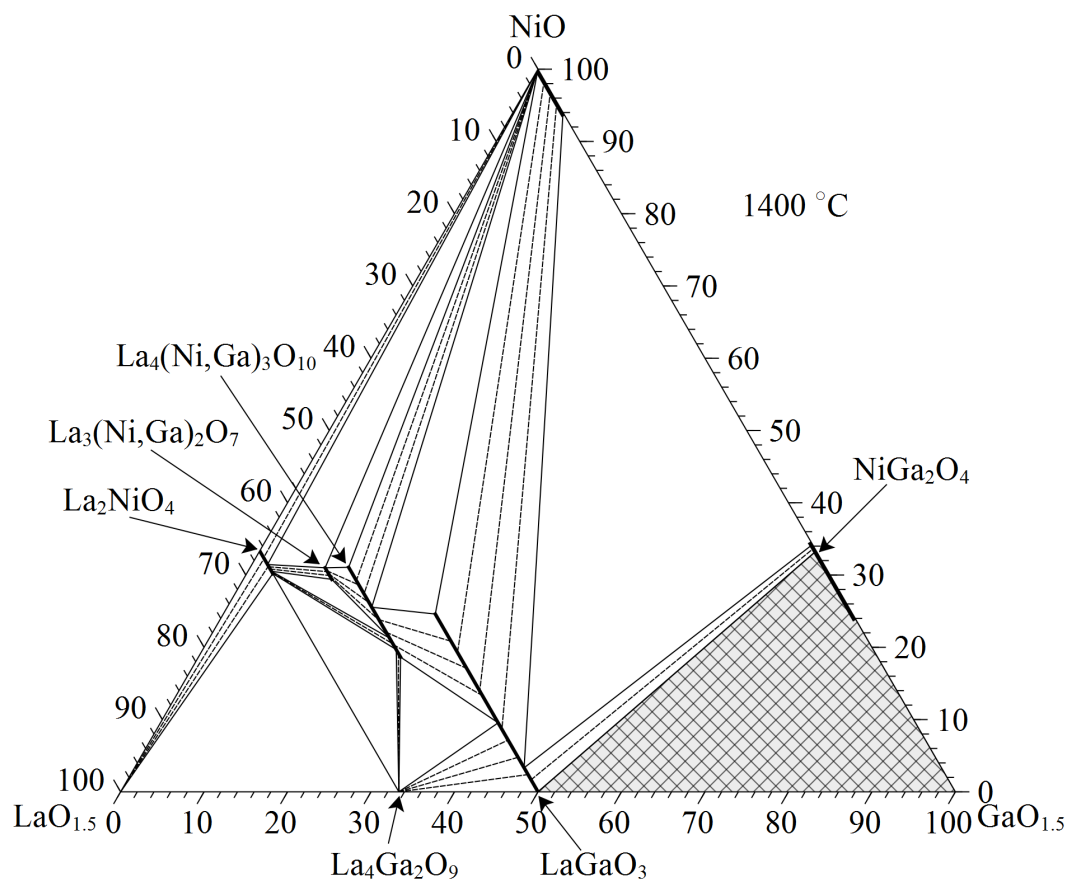


Figure 5.10: Approximate representation of the full $\text{LaO}_{1.5}$ - $\text{GaO}_{1.5}$ - NiO quasi-ternary phase diagram. The cross-hatched region at the gallium-rich corner indicates where melting behavior was observed.

5.4. Conclusions and Implications for SOFCs

Several important observations from the perspective of SOFC applications can be drawn from the diagram in Fig. 5.10. Of the three Ruddlesden-Popper phases with good cathode properties, only $\text{La}_4\text{Ni}_3\text{O}_{10}$ shows compatibility with LaGaO_3 which served as a proxy for LSGM electrolytes. Furthermore, the compatibility exists only with high gallium content in $\text{La}_4\text{Ni}_3\text{O}_{10}$ and high nickel content in LaGaO_3 ($\text{La}_4(\text{Ni}_{0.6}\text{Ga}_{0.4})_3\text{O}_{10} + \text{LaGa}_{0.5}\text{Ni}_{0.5}\text{O}_3$ at

one extreme, and $\text{La}_4(\text{Ni}_{0.44}\text{Ga}_{0.56})_3\text{O}_{10} + \text{LaGa}_{0.81}\text{Ni}_{0.19}\text{O}_3$ at the other extreme). With nickel increasing the electronic conductivity of the LaGaO_3 (LSGM) electrolyte, and gallium decreasing the conductivity of the $\text{La}_4\text{Ni}_3\text{O}_{10}$, this compatibility is not promising for the high temperature co-processing or long-term stability of $\text{La}_{n+1}\text{Ni}_n\text{O}_{3n+1}$ cathodes with LSGM electrolytes. On the anode side, NiO shows compatibility with a wide range of LaGaO_3 compositions. If the NiO is saturated with gallium ($\text{Ni}_{0.94}\text{Ga}_{0.06}\text{O}$), the diagram suggests that the nickel content in LaGaO_3 can be kept as low as 7% on gallium sites ($\text{LaGa}_{0.93}\text{Ni}_{0.07}\text{O}_3$), low enough to prevent a significant increase in electronic conductivity. [16, 17]

When the NiO is reduced to Ni metal during operation, the behavior of the excess gallium ultimately depends on the details of the operation conditions. For temperatures below 800 °C and oxygen partial pressures between 10^{-20} and 10^{-25} atm, Ga_2O_3 is expected to be stable, though higher operating temperature (around 1000 °C), or a more reducing fuel environment could reduce Ga_2O_3 to liquid gallium metal. [91, 92] If Ga_2O_3 is reduced, the gallium should be soluble in the nickel metal. [93] For the case of solid Ga_2O_3 , the formation of the NiGa_2O_4 spinel phase is also possible. Zinkevich et al predict a stable three-phase region of $\text{Ni} + \text{Ga}_2\text{O}_3 + \text{spinel}$, with 2-4% gallium dissolved in the nickel phase depending on temperature, and a spinel composition corresponding to the gallium-rich limit of the oxide quasi-binary system. [63] Reducing the oxygen content further eliminates the spinel phase, leaving Ga_2O_3 and metallic nickel with 2-4% gallium content. If needed, it may be possible to eliminate most of the gallium through sublimation as gaseous Ga_2O by exposing the anode to temperatures above 1000 °C in a reducing atmosphere. [94]

It should be noted that some studies have reported no evidence of the formation of other phases after firing La_2NiO_4 with LSGM at 1000 °C for as long as 72 hours. [71, 72] This is contrary to the results of the quasi-ternary phase diagram which would predict the formation of $\text{La}_4\text{Ga}_2\text{O}_9$ and $\text{La}_4\text{Ni}_3\text{O}_{10}$. The absence of these phases may be the result of slower kinetics

at the lower study temperature of 1000 °C compared to 1400 °C for the phase diagram. Other work has detected the formation of thin amorphous phases at the interface between La_2NiO_4 and YSZ and GDC electrolytes. [87] While the interfacial phases could be detected using transmission electron microscopy (TEM), and their effect on cathode performance could be observed using impedance spectroscopy, XRD methods were unable to detect the reaction. In addition, the effect of the Sr and Mg dopants in LSGM on the phase compatibility is unknown, warranting further studies into the long-term stability of $\text{La}_{n+1}\text{Ni}_n\text{O}_{3n+1}$ cathodes on LSGM with attention paid to the possible formation of interfacial phases.

CHAPTER 6

Summary and Recommendations for Future Work

Solid oxide fuel cells (SOFCs) are highly efficient solid state electrochemical devices that directly convert chemical energy into electricity. However, high operating temperatures necessitate expensive materials for various system components and accelerate degradation, preventing SOFCs from competing with traditional technologies on a cost per kilowatt-hour basis. This work focused on characterizing the electrochemical performance of SOFC materials at intermediate temperatures as well as the thermodynamic equilibrium between various layers to improve the long-term performance of SOFCs.

6.1. Hemispherical Electrolyte Probe Method

SOFC electrode performance is significantly affected by electrode morphology. When comparing the performance of SOFC electrodes made from different materials, it is important to ensure the electrodes have similar microstructures, or to characterize the microstructure using 3D tomography, making it difficult to obtain a direct comparison of materials' performance. Normalizing the electrode resistances by geometric factors to calculate metrics such

as the linear-specific TPB resistance ρ_{TPB} and area-specific resistance R_S enables a more direct comparison of SOFC electrode materials. This work developed and demonstrated the novel HEP method as an alternative to lithographically patterned electrode methods. The method uses impedance spectroscopy to measure the polarization resistance associated with the interface between an electrolyte probe and electrode pellet, as well as the resistance in the probe, which is used to determine the contact size used to normalize the polarization resistance. The contact radii determined from the probe resistances showed good agreement with predictions from elastic contact theory.

Comparisons of the normalized resistances with literature values revealed a systematic underestimation by a factor of about 3. This factor is expected to arise from assumptions relating to the geometric terms. The ρ_{TPB} analysis assumes a gas-tight circular contact with TPB around the circumference of the contact, while the R_S analysis assumes the whole contact area contributes to the reaction. A realistic contact between the polished surfaces likely consists of contact between multiple asperities within an overall circular contact area, increasing the total TPB length compared to the contact circumference. The HEP underestimation of R_S supports that there is sufficient gas transport under the probe contact and ionic conductivity in the MIEC electrodes to allow the entire contact area to be active, in addition to a substantial area beyond the probe contact. Despite the discrepancy in magnitude, the HEP measurements produced activation energies similar to those from literature.

6.2. $\text{LaO}_{1.5}\text{-GaO}_{1.5}\text{-NiO}$ Quasi-Ternary System

LSGM is one of the most promising electrolyte materials for SOFCs operating at intermediate temperatures, but reactivity with common electrode materials is a major issue. While reducing processing and operation temperature can limit interfacial reactions in the short-term through kinetic limitations, cation exchange during operation can significantly reduce

performance in the long-term. The thermodynamic equilibrium between LSGM and high-performance electrode materials can thus provide an idea of the long-term stability of devices with LSGM electrolytes.

The current work focused on equilibrium with nickel-containing materials, using LSGM's un-doped parent phase LaGaO_3 to simplify analysis. Previous work began to map out the quasi-ternary system, though much of the work relied on theoretical calculations with limited supporting experimental observations. This work established solubility limits and equilibrium involving LaGaO_3 in the $\text{LaO}_{1.5}\text{-GaO}_{1.5}\text{-NiO}$ quasi-ternary system at 1400 °C using conventional phase analysis and disappearing phase methods. For the first time, $\text{La}_3\text{Ni}_2\text{O}_7$ was observed to be stabilized at high temperature by the substitution of gallium for nickel over a narrow compositional range. Compatibility of LaGaO_3 with NiO and $\text{La}_4\text{Ni}_3\text{O}_{10}$ was confirmed, while any potential equilibrium between LaGaO_3 and the other $\text{La}_{n+1}\text{Ni}_n\text{O}_{3n+1}$ Ruddlesden-Popper phases was disturbed by the formation of $\text{La}_4\text{Ni}_3\text{O}_{10}$ and $\text{La}_4\text{Ga}_2\text{O}_9$. In both compatibilities, limiting the incorporation of nickel into LaGaO_3 is necessary to avoid significant electronic conductivity in LSGM. Saturating NiO with gallium was found to lead to equilibrium with LaGaO_3 with an acceptably low nickel content of only 7% of the gallium replaced by nickel in the latter. Equilibrium between LaGaO_3 and $\text{La}_4\text{Ni}_3\text{O}_{10}$, however, was found to require substantial levels of nickel in LaGaO_3 and gallium in $\text{La}_4\text{Ni}_3\text{O}_{10}$. Four-point conductivity measurements of $\text{La}_4(\text{Ni,Ga})_3\text{O}_{10}$ as a function of gallium content revealed a drastic decrease in conductivity. Increased electronic conductivity in LaGaO_3 (LSGM) and decreased conductivity in $\text{La}_4\text{Ni}_3\text{O}_{10}$ are not promising for the high temperature co-processing or long-term stability of $\text{La}_{n+1}\text{Ni}_n\text{O}_{3n+1}$ cathodes with LSGM electrolytes.

6.3. Future Directions

6.3.1 HEP Screening of Cathode and Anode Materials

The results in this work demonstrate the HEP method's ability to properly rank the performance of various electrode materials. Two methods for screening potential electrode materials are recommended. First, as long as a consistent contact size and similarly-prepared probes are used for each material, the measured temperature-dependent polarization resistances can be directly compared to obtain a ranking of electrode performance. This method requires no knowledge of the properties of electrode materials being compared. If the nature of conductivity in the electrode materials is known (electronic or MIEC), the polarization resistances can be normalized using the contact size as was done in this work. Since the underestimation of the normalized resistances appears to be more or less constant for a given combination of probe and pellet surface treatments, measuring a known electrode material and comparing to literature values from lithographically patterned electrodes could provide a correction factor used to calibrate HEP measurements of other materials in order to obtain more quantitatively accurate values.

In addition to comparing multiple material systems, the HEP method could be used to rapidly identify the effect of other factors on performance, such as composition. Many electrode materials rely on doping to increase ionic conductivity or modify shrinkage during processing. As more and more cations are included to modify performance, it becomes increasingly difficult to identify the ideal composition. HEP methods could be used to rapidly search the composition space, identifying the region of highest performance. Once materials and compositions with promising properties are identified, other characterization techniques can provide more in-depth analysis of the top candidates.

While this work focused on cathodes paired with a YSZ electrolyte, the same technique

could be used for other electrolyte materials as well as anode materials. Measuring anode materials would require no more than the creation of an experimental setup with a controlled atmosphere so that fuel can be supplied to the HEP setup rather than air. If dense probes of other electrolyte materials such as LSGM or GDC can be obtained, the same process can be applied with no further modification. Alternatively, YSZ probes could be coated with a layer of other electrolyte materials. The polarization resistance is sensitive to the interface and would likely be relatively unaffected by the thickness of the electrolyte coating. However, determining the contact size from the probe resistance may be more difficult. If the coating is thin enough, most of the resistance, including the spreading resistance, will arise from the YSZ portion of the probe, but further studies would be required to verify the accuracy of contact radius measurements.

6.3.2 LSGM-Ni Phase Stability

This work determined the details of phase stability of LaGaO_3 in the $\text{LaO}_{1.5}\text{-GaO}_{1.5}\text{-NiO}$ quasi-ternary system, using LaGaO_3 as a proxy for the behavior of LSGM. However, the effect of the strontium and magnesium dopants on phase equilibrium is unknown. In this work, equilibrium between LaGaO_3 and La_2NiO_4 was found to be disrupted by the formation of $\text{La}_4\text{Ga}_2\text{O}_9$ and $\text{La}_4\text{Ni}_3\text{O}_{10}$. However, some studies have fired mixed powders of La_2NiO_4 and LSGM at 1000 °C for as long as 72 hours with no evidence of reaction. [71, 72] The lack of reaction may be a result of kinetic limitations, but the LSGM dopants could also have a significant effect. Additionally, adding in more cations introduces more potential impurity phases that can form, such as SrLaGaO_4 . Mapping out the full $\text{LaO}_{1.5}\text{-SrO-GaO}_{1.5}\text{-MgO-NiO}$ quasi-quinary phase space is unrealistic, so other approaches are needed to identify long-term stability in the LSGM-Ni system. One potential approach would be to constrain the strontium and magnesium content to reduce the system to a quasi-ternary system, ei-

ther fixing both as a constant mole fraction, or replacing a fixed percentage of lanthanum with strontium, and replacing a fixed percentage of gallium and/or nickel with magnesium (e.g. the $\text{La}_{0.9}\text{Sr}_{0.1}\text{O}_{1.45}\text{-Ga}_{0.8}\text{Mg}_{0.2}\text{O}_{1.4}\text{-NiO}$ system). Alternatively, other characterization techniques such as TEM can be employed to detect interfacial reactions that can be difficult to detect with XRD methods, especially if the interfacial phases are amorphous. [87] Understanding the effects of the strontium and magnesium dopants in LSGM would aid in ensuring the long-term stability of SOFCs using LSGM electrolytes and nickel-containing electrodes.

6.3.3 Optimization and Stability of LNO-LSGM Cathodes

Devices using LSGM electrolytes and La_2NiO_4 cathodes have shown promising initial performance and good stability out to 144 hours of operation at 800 °C. [71] Additionally, $\text{La}_3\text{Ni}_2\text{O}_7$ and $\text{La}_4\text{Ni}_3\text{O}_{10}$ have been reported to show improved long-term (14 days) thermal stability and electrode performance compared to La_2NiO_4 , largely owing to increased electronic conductivity. [30,31] However, the results from this work suggest that eventually, detrimental cation exchange will occur at the interface between the lanthanum nickel oxides and LSGM. Additionally, coarsening of the cathode particles can lead to a significant decrease in performance over the lifetime of the devices. Longer term testing is therefore important for understanding how these devices behave over their target lifetimes of 50,000 hours.

Appendix A describes in detail preliminary work on synthesizing and characterizing symmetric devices using LSGM electrolytes and mixed La_2NiO_4 -LSGM cathodes. The powders for use in the cathodes were synthesized using a citric acid – EDTA method in order to obtain small particle sizes. By mixing LSGM in with the La_2NiO_4 in the cathode, it is hoped to physically constrain the coarsening of La_2NiO_4 particles with LSGM, which has a

higher melting temperature, and thus a slower expected coarsening rate. The work described in Appendix A establishes the thermal treatments required to achieve high purity cathode powders as well as mechanically stable cathode layers. Also included are some initial electrochemical tests of the performance of early attempts to make stable devices. Further study is required to achieve some level of optimization in these cathodes by altering such parameters as porosity, the La_2NiO_4 -to-LSGM mixing ratio, and electrode thickness. Once these parameters have been optimized, long-term testing on the order of 1000 hours can provide insight into degradation rate. Cycling symmetric devices with various cathode overpotentials (or various current densities) helps to further define the operating conditions required to avoid significant degradation in these cathodes, particularly for the application of reversible solid oxide cells. While current work has focused on cathodes based on La_2NiO_4 , largely because it is the most studied, the high performance observed in $\text{La}_3\text{Ni}_2\text{O}_7$ and $\text{La}_4\text{Ni}_3\text{O}_{10}$ symmetric cells warrants further investigation in devices that employ these materials. Much of the work optimizing La_2NiO_4 cathodes would likely translate to $\text{La}_3\text{Ni}_2\text{O}_7$ and $\text{La}_4\text{Ni}_3\text{O}_{10}$ cathodes. A comparison of long-term behavior of cathodes based on each $\text{La}_{n+1}\text{Ni}_n\text{O}_{3n+1}$ phase would complement previous studies of their initial performance as oxygen electrodes in various solid oxide cell devices.

References

- [1] U.S Energy Information Administration, “International Energy Outlook 2016,” 2016.
- [2] C. H. Wendel, Z. Gao, S. A. Barnett, and R. J. Braun, “Modeling and experimental performance of an intermediate temperature reversible solid oxide cell for high-efficiency, distributed-scale electrical energy storage,” *Journal of Power Sources*, vol. 283, pp. 329–342, 2015.
- [3] E.-C. Shin, P.-A. Ahn, H.-H. Seo, J.-M. Jo, S.-D. Kim, S.-K. Woo, J. H. Yu, J. Mizusaki, and J.-S. Lee, “Polarization mechanism of high temperature electrolysis in a Ni-YSZ/YSZ/LSM solid oxide cell by parametric impedance analysis,” *Solid State Ionics*, vol. 232, pp. 80–96, feb 2013.
- [4] Y.-S. Yoo, M. Choi, J.-H. Hwang, H.-N. Im, B. Singh, and S.-J. Song, “ $\text{La}_2\text{NiO}_{4+\delta}$ as oxygen electrode in reversible solid oxide cells,” *Ceramics International*, vol. 41, no. 5, pp. 6448–6454, 2015.
- [5] X. Yu and S. Ye, “Recent advances in activity and durability enhancement of Pt/C catalytic cathode in PEMFC. Part II: Degradation mechanism and durability enhancement of carbon supported platinum catalyst,” *Journal of Power Sources*, vol. 172, no. 1, pp. 145–154, 2007.
- [6] J. Wu, X. Z. Yuan, J. J. Martin, H. Wang, J. Zhang, J. Shen, S. Wu, and W. Merida, “A review of PEM fuel cell durability: Degradation mechanisms and mitigation strategies,” *Journal of Power Sources*, vol. 184, no. 1, pp. 104–119, 2008.
- [7] Y. Funahashi, T. Shimamori, T. Suzuki, Y. Fujishiro, and M. Awano, “Fabrication and characterization of components for cube shaped micro tubular SOFC bundle,” *Journal of Power Sources*, vol. 163, no. 2, pp. 731–736, 2007.

- [8] R. A. George, "Status of tubular SOFC field unit demonstrations," *Journal of Power Sources*, vol. 86, no. 1, pp. 134–139, 2000.
- [9] S. Nagata, A. Momma, T. Kato, and Y. Kasuga, "Numerical analysis of output characteristics of tubular SOFC with internal reformer," *Journal of Power Sources*, vol. 101, no. 1, pp. 60–71, 2001.
- [10] J. W. Fergus, "Electrolytes for solid oxide fuel cells," *Journal of Power Sources*, vol. 162, pp. 30–40, nov 2006.
- [11] Y. Ma, "Ceria-based Nanostructured Materials for Low-Temperature Solid Oxide Fuel Cells," 2012.
- [12] V. Kharton, F. Marques, and A. Atkinson, "Transport properties of solid oxide electrolyte ceramics: a brief review," *Solid State Ionics*, vol. 174, pp. 135–149, oct 2004.
- [13] K. Huang, R. S. Tichy, and J. B. Goodenough, "Superior Perovskite Oxide-Ion Conductor; Strontium- and Magnesium-Doped LaGaO₃: I, Phase Relationships and Electrical Properties," *Journal of the American Ceramic Society*, vol. 81, pp. 2565–2575, jan 1998.
- [14] A. Matraszek, "Phase diagram study in the La₂O₃-Ga₂O₃-MgO-SrO system in air," *Solid State Ionics*, vol. 166, pp. 343–350, jan 2004.
- [15] K. Huang and J. B. Goodenough, "A solid oxide fuel cell based on Sr- and Mg-doped LaGaO₃ electrolyte: the role of a rare-earth oxide buffer," *Journal of Alloys and Compounds*, vol. 304, pp. 454–464, 2000.
- [16] T. Ishihara, T. Shibayama, H. Nishiguchi, and Y. Takita, "Oxide Ion Conductivity in La_{0.8}Sr_{0.2}Ga_{0.8}Mg_{0.2-x}Ni_xO₃ Perovskite Oxide and Application for the Electrolyte of Solid Oxide Fuel Cells," *Journal of Materials Science*, vol. 36, no. 5, pp. 1125–1131, 2001.
- [17] P. Huang, A. Horky, and A. Petric, "Interfacial Reaction between Nickel Oxide and Lanthanum Gallate during Sintering and its Effect on Conductivity," *Journal of the American Ceramic Society*, vol. 82, pp. 2402–2406, sep 1999.
- [18] E. C. Miller, Z. Gao, and S. A. Barnett, "Fabrication of Solid Oxide Fuel Cells with a Thin (La_{0.9}Sr_{0.1})_{0.98}(Ga_{0.8}Mg_{0.2})O_{3-δ} Electrolyte on a Sr_{0.8}La_{0.2}TiO₃ Support," *Fuel Cells*, vol. 13, pp. 1060–1067, dec 2013.
- [19] Z. Gao, L. V. Mogni, E. C. Miller, J. G. Railsback, and S. A. Barnett, "A perspective on low-temperature solid oxide fuel cells," *Energy Environ. Sci.*, vol. 9, no. 5, pp. 1602–1644, 2016.

- [20] A. Atkinson, S. Barnett, R. J. Gorte, J. T. S. Irvine, A. J. McEvoy, M. Mogensen, S. C. Singhal, and J. Vohs, “Advanced anodes for high-temperature fuel cells,” *Nature Materials*, vol. 3, pp. 17–27, jan 2004.
- [21] P. I. Cowin, C. T. G. Petit, R. Lan, J. T. S. Irvine, and S. Tao, “Recent Progress in the Development of Anode Materials for Solid Oxide Fuel Cells,” *Advanced Energy Materials*, vol. 1, pp. 314–332, may 2011.
- [22] N. Q. Minh, “Ceramic Fuel Cells,” *Journal of the American Ceramic Society*, vol. 76, pp. 563–588, mar 1993.
- [23] S. Adler, “Factors governing oxygen reduction in solid oxide fuel cell cathodes.,” *Chemical reviews*, vol. 104, pp. 4791–843, oct 2004.
- [24] S. Adler, J. Lane, and B. Steele, “Electrode Kinetics of Porous Mixed-Conducting Oxygen Electrodes,” *Journal of The Electrochemical Society*, vol. 143, no. 11, pp. 3554–3564, 1996.
- [25] R. A. De Souza and M. Martin, “Probing Diffusion Kinetics with Secondary Ion Mass Spectrometry,” *MRS Bulletin*, vol. 34, pp. 907–914, dec 2009.
- [26] T. C. Yeh, J. L. Routbort, and T. O. Mason, “Oxygen transport and surface exchange properties of $\text{Sr}_{0.5}\text{Sm}_{0.5}\text{CoO}_{3-\delta}$,” *Solid State Ionics*, vol. 232, pp. 138–143, 2013.
- [27] J. A. Lane and J. A. Kilner, “Measuring oxygen diffusion and oxygen surface exchange by conductivity relaxation,” *Solid State Ionics*, vol. 136-137, pp. 997–1001, nov 2000.
- [28] F. S. Baumann, J. Fleig, G. Cristiani, B. Stuhlhofer, H.-U. Habermeier, and J. Maier, “Quantitative Comparison of Mixed Conducting SOFC Cathode Materials by Means of Thin Film Model Electrodes,” *Journal of The Electrochemical Society*, vol. 154, no. 9, p. B931, 2007.
- [29] Z. Shao and S. M. Haile, “A high-performance cathode for the next generation of solid-oxide fuel cells,” *Nature*, vol. 431, pp. 170–173, sep 2004.
- [30] S. Takahashi, S. Nishimoto, M. Matsuda, and M. Miyake, “Electrode Properties of the Ruddlesden-Popper Series, $\text{La}_{n+1}\text{Ni}_n\text{O}_{3n+1}$ ($n=1, 2, \text{ and } 3$), as Intermediate-Temperature Solid Oxide Fuel Cells,” *Journal of the American Ceramic Society*, vol. 93, pp. 2329–2333, aug 2010.
- [31] G. Amow, I. Davidson, and S. Skinner, “A comparative study of the Ruddlesden-Popper series, $\text{La}_{n+1}\text{Ni}_n\text{O}_{3n+1}$ ($n=1, 2 \text{ and } 3$), for solid-oxide fuel-cell cathode applications,” *Solid State Ionics*, vol. 177, pp. 1205–1210, may 2006.

- [32] X.-D. Zhou, J. Templeton, Z. Nie, H. Chen, J. Stevenson, and L. Pederson, "Electrochemical performance and stability of the cathode for solid oxide fuel cells: V. high performance and stable Pr_2NiO_4 as the cathode for solid oxide fuel cells," *Electrochimica Acta*, vol. 71, pp. 44–49, 2012.
- [33] J. G. Railsback, Z. Gao, and S. A. Barnett, "Oxygen electrode characteristics of $\text{Pr}_2\text{NiO}_{4+\delta}$ -infiltrated porous $(\text{La}_{0.9}\text{Sr}_{0.1})(\text{Ga}_{0.8}\text{Mg}_{0.2})\text{O}_{3-\delta}$," *Solid State Ionics*, vol. 274, pp. 134–139, 2015.
- [34] J. R. Wilson, J. S. Cronin, A. T. Duong, S. Rukes, H.-Y. Chen, K. Thornton, D. R. Mumm, and S. A. Barnett, "Effect of composition of $(\text{La}_{0.8}\text{Sr}_{0.2}\text{MnO}_3\text{-Y}_2\text{O}_3\text{-stabilized ZrO}_2)$ cathodes: Correlating three-dimensional microstructure and polarization resistance," *Journal of Power Sources*, vol. 195, pp. 1829–1840, apr 2010.
- [35] T. Klemensø, K. Thydén, M. Chen, and H.-J. Wang, "Stability of Ni-yttria stabilized zirconia anodes based on Ni-impregnation," *Journal of Power Sources*, vol. 195, pp. 7295–7301, nov 2010.
- [36] A. Buyukaksoy, V. Petrovsky, and F. Dogan, "Redox Stable Solid Oxide Fuel Cells with Ni-YSZ Cermet Anodes Prepared by Polymeric Precursor Infiltration," *Journal of The Electrochemical Society*, vol. 159, no. 2, p. B232, 2012.
- [37] A. N. Busawon, D. Sarantaridis, and A. Atkinson, "Ni Infiltration as a Possible Solution to the Redox Problem of SOFC Anodes," *Electrochemical and Solid-State Letters*, vol. 11, no. 10, p. B186, 2008.
- [38] X. Lou, S. Wang, Z. Liu, L. Yang, and M. Liu, "Improving $\text{La}_{0.6}\text{Sr}_{0.4}\text{Co}_{0.2}\text{Fe}_{0.8}\text{O}_{3-\delta}$ cathode performance by infiltration of a $\text{Sm}_{0.5}\text{Sr}_{0.5}\text{CoO}_{3-\delta}$ coating," *Solid State Ionics*, vol. 180, no. 23-25, pp. 1285–1289, 2009.
- [39] J. D. Nicholas, L. Wang, A. V. Call, and S. A. Barnett, "Use of the Simple Infiltrated Microstructure Polarization Loss Estimation (SIMPLE) model to describe the performance of nano-composite solid oxide fuel cell cathodes," *Physical Chemistry Chemical Physics*, vol. 14, no. 44, pp. 15379–15392, 2012.
- [40] C. Nicollet, A. Flura, V. Vibhu, S. Fourcade, A. Rougier, J.-M. Bassat, and J.-C. Grenier, "Preparation and characterization of $\text{Pr}_2\text{NiO}_{4+\delta}$ infiltrated into Gd-doped ceria as SOFC cathode," *Journal of Solid State Electrochemistry*, vol. 20, pp. 2071–2078, jul 2016.
- [41] W. G. Bessler, M. Vogler, H. Störmer, D. Gerthsen, A. Utz, A. Weber, and E. Ivers-Tiffée, "Model anodes and anode models for understanding the mechanism of hydrogen oxidation in solid oxide fuel cells.," *Physical chemistry chemical physics : PCCP*, vol. 12, pp. 13888–903, nov 2010.

- [42] D. Kek, M. Mogensen, and S. Pejovnik, "A Study of Metal (Ni, Pt, Au)/Yttria-Stabilized Zirconia Interface in Hydrogen Atmosphere at Elevated Temperature," *Journal of The Electrochemical Society*, vol. 148, no. 8, p. A878, 2001.
- [43] K. Vels Jensen, "Microstructural and chemical changes at the Ni/YSZ interface," *Solid State Ionics*, vol. 144, pp. 197–209, dec 2001.
- [44] G. Ostensen Lauvstad, R. Tunold, and S. Sunde, "Electrochemical Oxidation of CO on Pt and Ni Point Electrodes in Contact with an Yttria-Stabilized Zirconia Electrolyte," *Journal of The Electrochemical Society*, vol. 149, no. 12, p. E506, 2002.
- [45] K. Jensen, "Effect of impurities on structural and electrochemical properties of the Ni-YSZ interface," *Solid State Ionics*, vol. 160, pp. 27–37, may 2003.
- [46] K. V. Hansen, K. Norrman, and M. Mogensen, "H₂-H₂O-Ni-YSZ Electrode Performance," *Journal of The Electrochemical Society*, vol. 151, no. 9, p. A1436, 2004.
- [47] M. S. Schmidt, K. Vels Hansen, K. Norrman, and M. Mogensen, "Three-phase-boundary dynamics at the Ni/ScYSZ interface," *Solid State Ionics*, vol. 180, pp. 431–438, apr 2009.
- [48] J. R. Wilson, A. T. Duong, M. Gameiro, H.-Y. Chen, K. Thornton, D. R. Mumm, and S. A. Barnett, "Quantitative three-dimensional microstructure of a solid oxide fuel cell cathode," *Electrochemistry Communications*, vol. 11, no. 5, pp. 1052–1056, 2009.
- [49] A. K. Opitz and J. Fleig, "Investigation of O₂ reduction on Pt/YSZ by means of thin film microelectrodes: The geometry dependence of the electrode impedance," *Solid State Ionics*, vol. 181, pp. 684–693, jun 2010.
- [50] Y. B. Kim, C.-M. Hsu, S. T. Connor, T. M. Gur, Y. Cui, and F. B. Prinz, "Nanopore Patterned Pt Array Electrodes for Triple Phase Boundary Study in Low Temperature SOFC," *Journal of The Electrochemical Society*, vol. 157, no. 9, p. B1269, 2010.
- [51] A. Bieberle, L. P. Meier, and L. Gauckler, "The Electrochemistry of Ni Pattern Anodes Used as Solid Oxide Fuel Cell Model Electrodes," *Journal of The Electrochemical Society*, vol. 148, no. 6, p. A646, 2001.
- [52] M. V. Rao, J. Fleig, M. Zinkevich, and F. Aldinger, "The influence of the solid electrolyte on the impedance of hydrogen oxidation at patterned Ni electrodes," *Solid State Ionics*, vol. 181, pp. 1170–1177, aug 2010.
- [53] R. Radhakrishnan, A. V. Virkar, and S. C. Singhal, "Estimation of Charge-Transfer Resistivity of La_{0.8}Sr_{0.2}MnO₃ Cathode on Y_{0.16}Zr_{0.84}O₂ Electrolyte Using Patterned Electrodes," *Journal of The Electrochemical Society*, vol. 152, no. 1, p. A210, 2005.

- [54] L. J. Miara, J. N. Davis, S. N. Basu, U. B. Pal, and S. Gopalan, "Application of a State-Space Model to Patterned Cathodes of $(\text{La}_{0.87}\text{Ca}_{0.13})_{0.95}\text{MnO}_3$," *Journal of The Electrochemical Society*, vol. 158, no. 12, p. B1523, 2011.
- [55] V. Brichzin, "The geometry dependence of the polarization resistance of Sr-doped LaMnO_3 microelectrodes on yttria-stabilized zirconia," *Solid State Ionics*, vol. 152-153, pp. 499–507, dec 2002.
- [56] J. Fleig, F. S. Baumann, V. Brichzin, H.-R. Kim, J. Jamnik, G. Cristiani, H.-U. Habermeier, and J. Maier, "Thin Film Microelectrodes in SOFC Electrode Research," *Fuel Cells*, vol. 6, pp. 284–292, aug 2006.
- [57] C. Dogan, K. Stöwe, and W. F. Maier, "Optical high-throughput screening for activity and electrochemical stability of oxygen reducing electrode catalysts for fuel cell applications," *ACS Combinatorial Science*, vol. 17, no. 3, pp. 164–175, 2015.
- [58] T. H. Muster, A. Trinchi, T. A. Markley, D. Lau, P. Martin, A. Bradbury, A. Bendavid, and S. Dligatch, "A review of high throughput and combinatorial electrochemistry," *Electrochimica Acta*, vol. 56, no. 27, pp. 9679–9699, 2011.
- [59] P. Datta, P. Majewski, and F. Aldinger, "Synthesis and microstructural characterization of Sr- and Mg-substituted LaGaO_3 solid electrolyte," *Materials Chemistry and Physics*, vol. 102, pp. 240–244, apr 2007.
- [60] N. Solak, *Interface Stability in Solid Oxide Fuel Cells for Intermediate Temperature Applications*. PhD thesis, 2007.
- [61] J.-N. Audinot, J.-M. Bassat, A. Wattiaux, J.-C. Grenier, and M. Pouchard, "Investigations of the $\text{LaGa}_{1-x}\text{Ni}_x\text{O}_{3-\delta}$ ($x < 0.50$) system in the scope of SOFC's: synthesis and physical characterizations," *Comptes Rendus de l'Académie des Sciences - Series IIC - Chemistry*, vol. 2, pp. 69–73, feb 1999.
- [62] M. Zinkevich, S. Geupel, H. Nitsche, M. Ahrens, and F. Aldinger, "Study of the La_2O_3 - Ga_2O_3 System by Experiment and Thermodynamic Calculations," *Journal of Phase Equilibria & Diffusion*, vol. 25, pp. 437–447, oct 2004.
- [63] M. Zinkevich, S. Geupel, and F. Aldinger, "Thermodynamic assessment of the ternary systems Ga-Mg-O, Ga-Ni-O, Mg-Ni-O and extrapolation to the Ga-Mg-Ni-O phase diagram," *Journal of Alloys and Compounds*, vol. 393, pp. 154–166, may 2005.
- [64] R. D. Shannon, "Revised effective ionic radii and systematic studies of interatomic distances in halides and chalcogenides," *Acta Crystallographica Section A*, vol. 32, pp. 751–767, sep 1976.
- [65] M. Zinkevich and F. Aldinger, "Thermodynamic analysis of the ternary La-Ni-O system," *Journal of Alloys and Compounds*, vol. 375, pp. 147–161, jul 2004.

- [66] M. Hrovat, S. Bernik, J. Holc, and Z. Samardzija, "Subsolidus phase equilibria in the La_2O_3 - Ga_2O_3 - NiO system," *Journal of Materials Research*, vol. 14, no. 6, pp. 2351–2354, 1999.
- [67] N. Solak, M. Zinkevich, and F. Aldinger, "Reactivity in LaGaO_3/Ni and CeO_2/Ni Systems," *Fuel Cells*, vol. 6, pp. 87–92, apr 2006.
- [68] T. Moriga, D. D. Edwards, T. O. Mason, G. B. Palmer, K. R. Poeppelmeier, J. L. Schindler, C. R. Kannewurf, and I. Nakabayashi, "Phase Relationships and Physical Properties of Homologous Compounds in the Zinc Oxide-Indium Oxide System," *Journal of the American Ceramic Society*, vol. 81, pp. 1310–1316, jan 2005.
- [69] T. Moriga, D. R. Kammler, T. O. Mason, G. B. Palmer, and K. R. Poeppelmeier, "Homologous Compounds in the Indium-Gallium-Zinc Oxide System," *Journal of American Ceramic Society*, vol. 82, no. 10, pp. 2705–2710, 1999.
- [70] N. Solak, M. Zinkevich, and F. Aldinger, "Compatibility of La_2NiO_4 cathodes with LaGaO_3 electrolytes: A computational approach," *Solid State Ionics*, vol. 177, pp. 2139–2142, oct 2006.
- [71] M. J. Escudero, A. Fuerte, and L. Daza, " $\text{La}_2\text{NiO}_{4+\delta}$ potential cathode material on $\text{La}_{0.9}\text{Sr}_{0.1}\text{Ga}_{0.8}\text{Mg}_{0.2}\text{O}_{2.85}$ electrolyte for intermediate temperature solid oxide fuel cell," *Journal of Power Sources*, vol. 196, pp. 7245–7250, sep 2010.
- [72] R. Sayers, J. Liu, B. Rustumji, and S. J. Skinner, "Novel K_2NiF_4 -Type Materials for Solid Oxide Fuel Cells: Compatibility with Electrolytes in the Intermediate Temperature Range," *Fuel Cells*, vol. 8, pp. 338–343, oct 2008.
- [73] S. Bernal, F. Botana, R. García, and J. Rodríguez-Izquierdo, "Behaviour of rare earth sesquioxides exposed to atmospheric carbon dioxide and water," *Reactivity of Solids*, vol. 4, pp. 23–40, oct 1987.
- [74] F. M. Smits, "Measurement of Sheet Resistivities with the Four-Point Probe," *Bell System Technical Journal*, vol. 37, pp. 711–718, may 1958.
- [75] D. S. McLachlan, M. Blaszkiewicz, and R. E. Newnham, "Electrical Resistivity of Composites," *Journal of the American Ceramic Society*, vol. 73, pp. 2187–2203, aug 1990.
- [76] J. Newman, "Resistance for Flow of Current to a Disk," *Journal of The Electrochemical Society*, vol. 113, no. 5, pp. 501–502, 1966.
- [77] R. Holm, *Electric Contacts*. New York: Springer-Verlag, 4 ed., 1967.
- [78] B. A. Boukamp, "Equivalent Circuit for Windows," 2005.

- [79] F. Baumann, J. Fleig, H. Habermeier, and J. Maier, "Impedance spectroscopic study on well-defined (La,Sr)(Co,Fe)O_{3-δ} model electrodes," *Solid State Ionics*, vol. 177, pp. 1071–1081, apr 2006.
- [80] J. Fleig, "Microelectrodes in solid state ionics," *Solid State Ionics*, vol. 161, pp. 279–289, aug 2003.
- [81] S. Adler, "Chemical Expansivity of Electrochemical Ceramics," *Journal of the American Ceramic Society*, vol. 841, no. 9, pp. 2117–2119, 2001.
- [82] A. S. Ziarani and R. Aguilera, "Knudsen's Permeability Correction for Tight Porous Media," *Transport in Porous Media*, vol. 91, no. 1, pp. 239–260, 2012.
- [83] S. P. Jiang, "Thermally and Electrochemically Induced Electrode/Electrolyte Interfaces in Solid Oxide Fuel Cells: An AFM and EIS Study," *Journal of The Electrochemical Society*, vol. 162, no. 10, pp. F1119–F1128, 2015.
- [84] S. Giraud and J. Canel, "Young's modulus of some SOFCs materials as a function of temperature," *Journal of the European Ceramic Society*, vol. 28, pp. 77–83, jan 2008.
- [85] N. Orlovskaya, K. Kleveland, T. Grande, and M.-A. Einarsrud, "Mechanical properties of LaCoO₃ based ceramics," *Journal of the European Ceramic Society*, vol. 20, no. December 1998, pp. 51–56, 2000.
- [86] I. C. Fullarton, J. P. Jacobs, H. E. van Benthem, J. A. Kilner, H. H. Brongersma, P. J. Scanlon, and B. C. H. Steele, "Study of oxygen ion transport in acceptor doped samarium cobalt oxide," *Ionics*, vol. 1, pp. 51–58, jan 1995.
- [87] A. Montenegro-Hernández, A. Soldati, L. Moggi, H. Troiani, A. Schreiber, F. Soldera, and A. Caneiro, "Reactivity at the Ln₂NiO_{4+δ}/electrolyte interface (Ln = La, Nd) studied by Electrochemical Impedance Spectroscopy and Transmission Electron Microscopy," *Journal of Power Sources*, vol. 265, pp. 6–13, nov 2014.
- [88] Y. Lin and S. A. Barnett, "Co-Firing of Anode-Supported SOFCs with Thin La_{0.9}Sr_{0.1}Ga_{0.8}Mg_{0.2}O_{3-δ} Electrolytes," *Electrochemical and Solid-State Letters*, vol. 9, no. 6, p. A285, 2006.
- [89] S. An, "Characterization of Cu-CeO₂ direct hydrocarbon anodes in a solid oxide fuel cell with lanthanum gallate electrolyte," *Solid State Ionics*, vol. 175, pp. 135–138, nov 2004.
- [90] K. Huang, J. Wan, and J. B. Goodenough, "Oxide-Ion Conducting Ceramics for Solid Oxide Fuel Cells," *Journal of Materials Science*, vol. 36, no. 5, pp. 1093–1098, 2001.
- [91] M. Asadian, "The Influence of Atmosphere on Oxides Crystal Growth," *Modern Aspects of Bulk Crystal and Thin Film Preparation*, 2012.

- [92] D. F. Wilson, E. C. Beahm, T. M. Besmann, J. H. Devan, J. R. Distefano, S. R. Greene, P. L. Rittenhouse, and B. a. Worley, "Potential Effects of Gallium on Cladding Materials," *Ornl*, vol. TM-13504, 1997.
- [93] Z.-M. Cao, X. Shi, W. Xie, I. Ohnuma, K. Ishida, and Z.-Y. Qiao, "Thermodynamic reassessment of NiGa binary system," *Rare Metals*, vol. 34, pp. 864–872, dec 2015.
- [94] D. Kolman, M. Griego, C. James, and D. Butt, "Thermally induced gallium removal from plutonium dioxide for MOX fuel production," *Journal of Nuclear Materials*, vol. 282, pp. 245–254, dec 2000.
- [95] N. A. Abdullah, S. Hasan, and N. Osman, "Role of CA-EDTA on the Synthesizing Process of Cerate-Zirconate Ceramics Electrolyte," *Journal of Chemistry*, vol. 2013, pp. 1–7, 2013.
- [96] N. Hildenbrand, P. Nammensma, D. H. A. Blank, H. J. M. Bouwmeester, and B. A. Boukamp, "Influence of configuration and microstructure on performance of $\text{La}_2\text{NiO}_{4+\delta}$ intermediate-temperature solid oxide fuel cells cathodes," *Journal of Power Sources*, vol. 238, pp. 442–453, 2013.

APPENDIX A

Fabrication and Performance of Mixed La_2NiO_4 -LSGM Cathodes

Symmetric cells with identical cathodes on either side of the electrolyte are useful for studying cathode performance without the need to subtract contributions from the anode. Measuring the electrochemical performance around open circuit conditions provides a close approximation of cathode performance during operation in full fuel cells.

A.1. Synthesis and Purity of Cathode Powders

Citric acid – EDTA synthesis, a modified Pechini process, was used to synthesize powders of La_2NiO_4 (LNO) and $\text{La}_{0.9}\text{Sr}_{0.1}\text{Ga}_{0.8}\text{Mg}_{0.2}\text{O}_{3-\delta}$ (LSGM) with smaller particle sizes compared to what is typically obtained through solid state synthesis. Metal nitrates were weighed in the desired molar ratio of metal cations and dissolved in water in a glass beaker on a stir plate. One mole of ethylenediaminetetraacetic acid (EDTA) and two moles of citric acid for each mole of metal cations were weighted out. The EDTA was dissolved in ammonium hydroxide in another glass beaker on a stir plate, then added to the aqueous nitrate solution, before adding the citric acid. White precipitates generally formed after adding the EDTA in

ammonium hydroxide, but disappeared after adding citric acid and stirring. The EDTA and citric acid act as chelating agents, forming organic complexes around the dissolved metal ions to keep them evenly dispersed in solution. [95] The solution was then heated and stirred in a glass beaker on a stirring hot plate around 80-120 °C to evaporate the solvents until a thick gel formed. The gel was then moved to a vented furnace and held at 250 °C until the gel was converted to a highly porous ash. Ventilation is important, as the nitrous oxides are released when the nitrates are burned. The ash was then collected, ground in an agate mortar and pestle, and fired at high temperature to form the desired metal oxide.

Keeping the final firing temperature as low as possible maintained as small of a particle size as possible, but too low of a temperature provided insufficient energy for a full reaction and phase purity. The phase content of the LNO and LSGM powders was characterized using XRD and WPF (section 3.2) as a function of the temperature used to fire the ash powder into oxide powder. The compositions of LSGM powders as a function of firing temperature are shown in Fig. A.1, with the XRD spectra for powders fired between 1000 and 1400 °C shown in Fig. A.2. At the lowest temperatures, little to no LSGM was detected, and the powders were primarily comprised of $\text{La}_4\text{Ga}_2\text{O}_9$, with impurities of SrLaGaO_4 , $\text{SrLaGa}_3\text{O}_7$, and traces of MgO . As the firing temperature increased, the $\text{La}_4\text{Ga}_2\text{O}_9$ content decreased, and the LSGM content significantly increased, up to 98.7 ± 2.6 wt% for powder fired at 1400 °C for 4 hours. This can also be observed in the disappearance of impurity peaks in Fig. A.2. The compositions of the LNO powders are shown in Fig. A.3. Even at low temperatures, the powders show fairly high purity. La_2O_3 is the only impurity detected with the exception of some $\text{La}(\text{OH})_3$ in one of the powders that likely formed from the hydration the La_2O_3 over time when exposed to air. The presence of excess La_2O_3 with no evidence of excess NiO suggests that the synthesized LNO powder may be slightly A-site deficient. Powder fired for one hour at 900 °C was over 95 wt% LNO. Firing at higher temperatures may slightly

improve the purity, but likely at the cost of a significantly increased particle size. From the results of these studies, powders of LNO fired for one hour at 900 °C and LSGM fired for four hours at 1400 °C are recommended for creating inks for LNO-LSGM mixed cathodes.

A.2. Synthesis of LSGM Electrolytes

Dense electrolyte pellets of LSGM were synthesized from commercial powders of La_2O_3 (Aldrich, 99.99%), SrCO_3 (Alfa Aesar, 99%), Ga_2O_3 (Aldrich, 99.99%), and MgO (Alfa Aesar, 96%) using a modified version of the solid state synthesis methods described in section 3.1. The weighed powders placed in a high-density polyethylene bottle with YSZ milling media and covered with ethanol. The lid of the bottle was taped shut before placing the bottle on a ball mill to mix the powders overnight. The ball milled powder was then dried in an oven around 70 °C before firing in a large alumina crucible for twelve hours at 1250 °C. The fired powder was mixed with 2 wt% polyvinyl butyral (PVB) as a binding agent, then ball milled and dried again. The LSGM + PVB mixture was passed through a size 120 sieve (wire spacing of 125 μm) in order to eliminate large particles and flakes before pressing 0.5 g of the sieved powder into each pellet using a steel die set with a diameter of 19 mm, and firing the pellets on alumina plates for four hours at 1400 °C. XRD performed on a fired pellet confirmed the phase purity of the LSGM electrolyte pellets. Pellets used for device fabrication were visually inspected to ensure flat surfaces free of cracks and bubbles.

A.3. Device Fabrication

Symmetric devices were fabricated by screen printing circular cathodes on each side of LSGM electrolyte pellets. Cathode powders synthesized using the citric acid – EDTA method and fired for four hours at 1000 °C were mixed and ball milled overnight with 30 wt% graphite

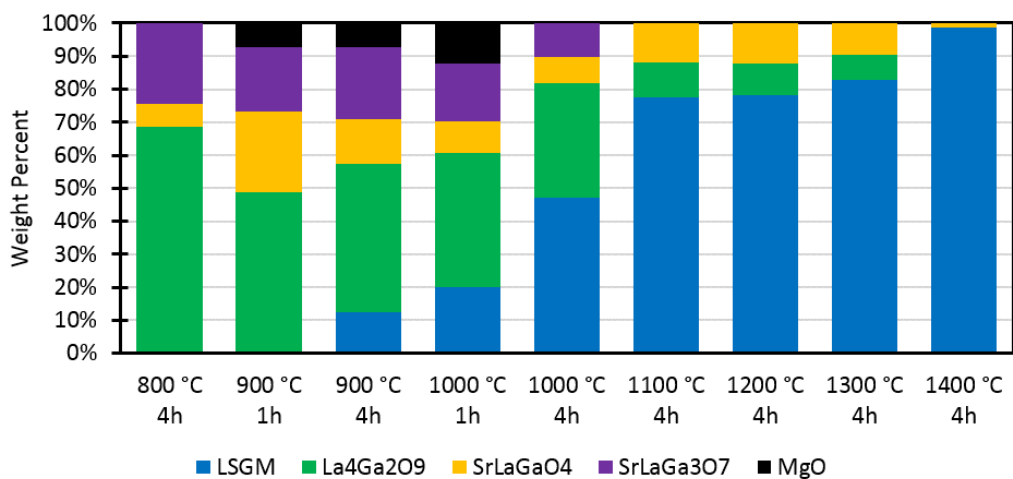


Figure A.1: Composition of LSGM powders prepared using the citric acid – EDTA method using various firing conditions.

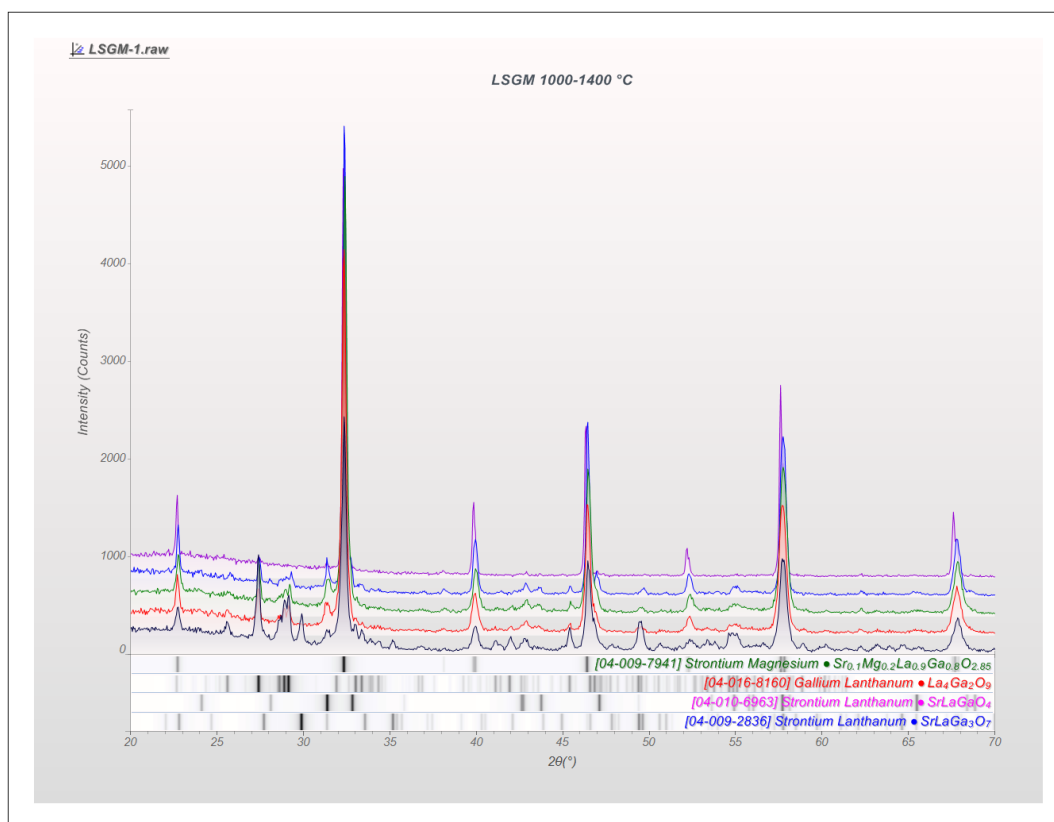


Figure A.2: XRD spectra of LSGM powders fired between 1000 °C (black) and 1400 °C (purple). By 1400 °C, nearly all of the peaks corresponding to impurity phases have disappeared.

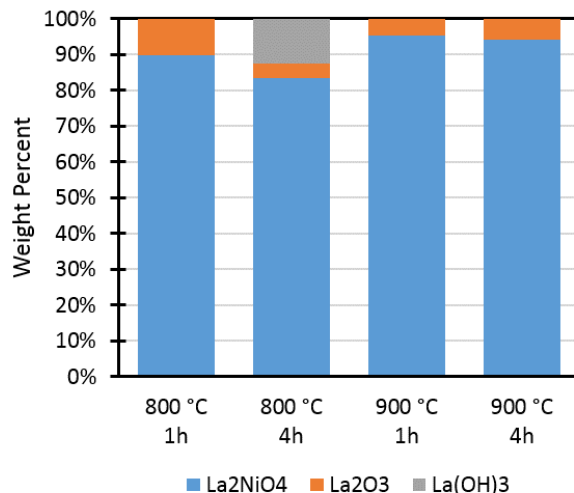


Figure A.3: Composition of La_2NiO_4 powders prepared using the citric acid – EDTA method using various firing conditions.

as a pore former. It should be noted that the LSGM powder used in these cathodes likely contained only about 50 wt% LSGM, with the rest made up from impurities including $\text{La}_4\text{Ga}_2\text{O}_9$ and $\text{SrLaGa}_3\text{O}_7$, as illustrated in Fig. A.1. While this purity is too low to create efficient cathodes, the ink can be used to gain an idea of the processing conditions required to turn these types of powders into stable cathodes. After drying the ball milled cathode powder, it was mixed with Heraeus vehicle V-737 (1.17 times the total mass of powder) and run three times through a three-roll mill to create a cathode ink. The ink was then screen printed onto electrolyte pellets using a mask to create circular electrodes with areas of 0.5 cm^2 . The electrodes were dried in an oven around $150 \text{ }^\circ\text{C}$ before repeating screen printing a total of three times on each side to achieve the desired electrode thickness. The symmetric devices were then heated to $600 \text{ }^\circ\text{C}$ for one hour to burn out the V-737 vehicle and graphite pore former before firing at higher temperatures between 1000 and $1400 \text{ }^\circ\text{C}$ for four hours.

Silver grids were screen printed onto the fired cathodes to ensure good electrical contact. However, the cathodes proved too fragile, sticking to the silver paste and peeling off. To remedy this, single layers of $(\text{La}_{0.8}\text{Sr}_{0.2})_{0.98}\text{MnO}_4$ (LSM) were screen printed on top of the

cathodes as current collectors and fired at 1050 °C for 4 hours. The lower viscosity of the LSM ink allowed for it to be screen printed onto the fragile LNO-LSGM cathode layers more easily than the silver ink. LSM current collectors were successfully applied to cathodes fired at or above 1200 °C, with cathodes fired at 1000 and 1100 °C peeling off when screen printing the current collector. After firing for four hours at 1050 °C, the current collector provided enough mechanical stability for the cathode layer to allow for the silver grid to be screen printed on top of the LSM current collector. Finally, silver wires were attached to the silver grids using silver paste cured in an oven around 150 °C for about 15 minutes.

A.4. Initial Electrochemical Performance

Impedance spectroscopy was used to measure and separate the various resistances in the fabricated device over the temperature range of 600-800 °C. A representative impedance spectrum for the device made using impure LSGM powder is shown in Fig. A.4. The high frequency offset is attributed to the ohmic resistance of the LSGM pellet, while the two arcs observed at lower frequency are attributed to the polarization resistance associated with the cathode reaction. The ohmic and polarization resistances were divided in half and multiplied by the cathode area (0.5 cm²) to calculate the area-specific resistances for one half of the symmetric cell. The area-specific resistances are plotted as a function of temperature in Fig. A.5. The polarization resistance can also be split into the resistances of the two component arcs, as shown in Fig. A.6. The two responses could not reliably be separated at 800 °C. The two responses have peak frequencies around 1 Hz and 1000 Hz. The lower frequency response exhibits a significantly higher activation energy (Table A.1), leading to a larger low frequency resistance below 750 °C. The polarization resistances are approximately 3-5 times larger than those reported for more optimized La₂NiO₄ cathodes. [96] However, the polarization resistance is expected to decrease significantly with the use of a higher purity

LSGM powder and further optimization of processing conditions.

As of now, the processes associated with the two observed responses in the polarization arcs remain unidentified. Work is ongoing to fabricate and characterize a symmetric device with cathodes made using LSGM powder fired at 1400 °C in order to eliminate impurities. Further experiments investigating the effects of microstructure, composition, and oxygen partial pressure may provide information useful in identifying the causes of the two major cathode resistances. Other suggestions for future work are discussed in Chapter 6.

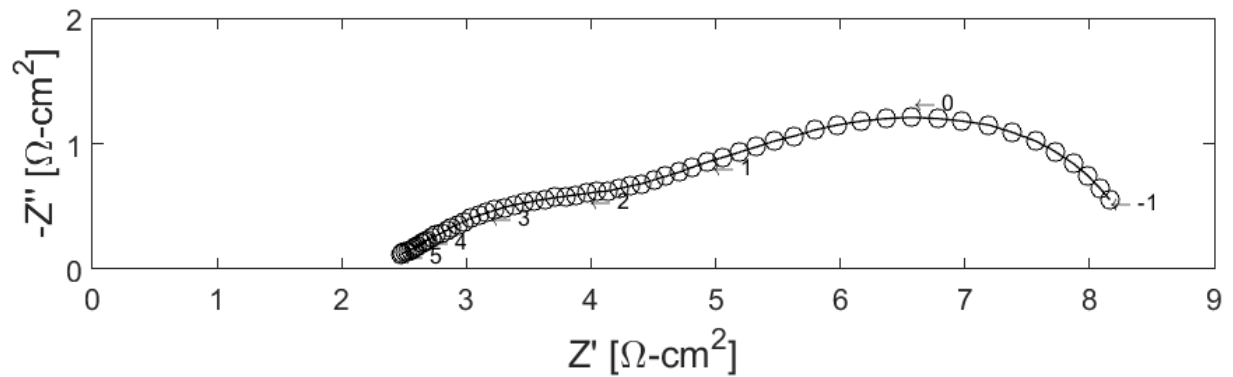


Figure A.4: Nyquist plot for the symmetric LNO-LSGM cathode device, measured at 700 °C. Made using LSGM and LNO powder fired 4 hours at 1000 °C. The numbers denote decades of frequency.

Table A.1: Measured activation energies of the ohmic and polarization resistances as well the two components of the total polarization resistance.

| Resistance | R_{Ohmic} | R_{Pol} | R_{MF} | R_{LF} |
|------------------------|-------------|-----------|----------|----------|
| Activation Energy [eV] | 0.585 | 0.653 | 0.467 | 0.810 |

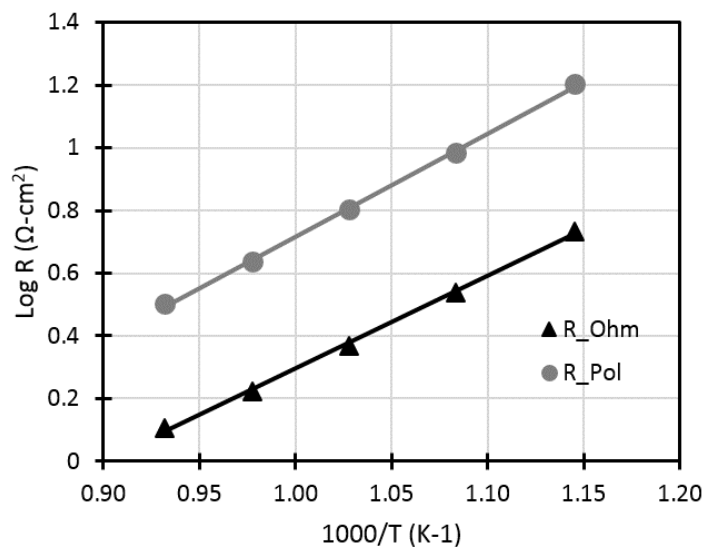


Figure A.5: Temperature dependence of the ohmic and polarization resistances of the symmetric device.

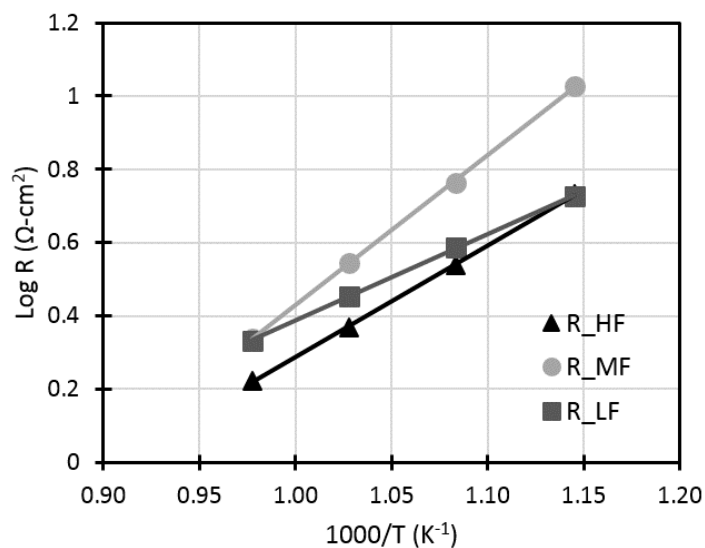


Figure A.6: Temperature dependence of the high frequency (HF), middle frequency (MF), and low frequency (LF) resistances. The high frequency resistance is attributed to the ohmic resistance of the LSGM pellet, while the middle and low frequency resistances were attributed to the polarization resistance.

APPENDIX B

LaO_{1.5}-GaO_{1.5}-NiO Phase Diagram Samples

| Sample | n | x | n=1 | n=2 | n=3 | LGO | LGR | NiO | Spinel | La4Ga2O9 |
|--------|------|-------|-----|-----|-----|-----|-----|-----|--------|----------|
| CL12 | 1 | 0.4 | x | | | | | | | x |
| CL4 | 1 | 0.05 | x | | | | | | | |
| CL8 | 1 | 0.25 | x | | | | | | | x |
| REB10 | 1 | 0.23 | x | | | | | | | x |
| REB13 | 1 | 0.25 | x | | | | | | | x |
| REB16 | 1 | 0.22 | x | | | | | | | x |
| S13 | 1 | 0.1 | x | | | | | | | |
| S14 | 1 | 0.3 | x | | | | | | | x |
| S25 | 1 | 0.4 | x | | | | | | | x |
| S26 | 1 | 0.5 | x | | | | | | | x |
| S29 | 1 | 0.15 | x | | | | | | | x |
| S30 | 1 | 0.2 | x | | | | | | | x |
| S43 | 1 | 0.95 | x | | | | | | | x |
| REB2 | 2 | 0.2 | x | x | | | | x | | |
| REB3 | 2 | 0.3 | x | x | x | | | | | |
| REB4 | 2 | 0.4 | x | x | x | | | | | |
| REB5 | 2 | 0.25 | | x | | | | | | |
| REB6 | 2 | 0.5 | x | | x | | | | | x |
| REB7 | 2 | 0.275 | | x | | | | | | |
| REB8 | 2 | 0.25 | | x | | | | | | |
| REBa? | 2 | 0.1 | x | x | | | | x | | |
| REBb? | 2 | 0.2 | x | x | | | | x | | |
| S23 | 2 | 0.28 | x | x | x | | | | | |
| S24 | 2 | 0.29 | x | x | x | | | | | |
| CL1 | 3 | 0.7 | | | x | x | | | | x |
| CL10 | 3 | 0.55 | | | x | | | | | |
| CL11 | 3 | 0.575 | | | x | | | | | x |
| CL2 | 3 | 0.8 | | | x | | x | | | x |
| CL3 | 3 | 0.6 | | | x | x | | | | x |
| CL5 | 3 | 0.15 | x | x | | | | x | | |
| CL6 | 3 | 0.25 | | x | x | | | | | |
| CL9 | 3 | 0.525 | | | x | | | | | |
| S15 | 3 | 0.1 | x | | x | | | x | | |
| S16 | 3 | 0.3 | | | x | | | | | |
| S47 | 3 | 0.75 | | | x | x | | | | x |
| S31 | La40 | 0.9 | | x | | | | x | | |
| S32 | La40 | 0.65 | | | | | x | x | | |
| S33 | La40 | 0.85 | | x | x | | | x | | |
| S34 | La40 | 0.7 | | | x | | x | x | | |
| S35 | La40 | 0.1 | | | | x | | | x | |
| S36 | La40 | 0.35 | | | | x | | x | x | |
| S37 | La40 | 0.15 | | | | x | | x | x | |
| S38 | La40 | 0.3 | | | | x | | x | x | |
| S39 | La40 | 0.2 | | | | x | | x | x | |
| S40 | La40 | 0.25 | | | | x | | x | x | |
| S10 | LGO | 0.02 | | | | x | | | | |
| S4 | LGO | 0.4 | | | | | x | | | |
| S41 | LGO | 0.55 | | | x | | x | x | | |
| S42 | LGO | 0.6 | | | x | | x | x | | |
| S45 | LGO | 0.5 | | | | | x | | | |
| S46 | LGO | 0.65 | | | x | | x | x | | |
| S9 | LGO | 0.05 | | | | x | | | | |